

**Towards new Front-End Electronics  
for the  
HADES Drift Chamber System**

Dissertation  
zur Erlangung des Doktorgrades  
der Naturwissenschaften

vorgelegt beim Fachbereich Physik  
der Johann Wolfgang Goethe-Universität  
in Frankfurt am Main

von  
**Michael Wiebusch**  
aus Fritzlar

Mai 2019  
(D30)

vom Fachbereich Physik der  
Johann Wolfgang Goethe-Universität als Dissertation angenommen.

Dekan:	Prof. Dr. Michael Lang
Gutachter:	Prof. Dr. Joachim Stroth
	Prof. Dr. Christoph Blume
Datum der Disputation:	17.07.2019

## Abstract

HADES (High Acceptance DiElectron Spectrometer), located at GSI, is a versatile detector for precise spectroscopy of  $e^+ e^-$  pairs and charged hadrons produced on a fixed target in a 1 AGeV to 3.5 AGeV kinetic beam energy region. The main experimental goal is to investigate properties of dense nuclear matter created in heavy ion collisions and learn about in-medium hadron properties.

In the HADES set-up 24 Mini Drift Chambers (MDC) allow for track reconstruction and determining the particle momentum by exploiting charged particle deflection in a magnetic field. In addition, the drift chambers contribute to particle identification by measuring the energy loss. The read-out concept foresees each sensing wire to be equipped with a preamplifier, analog pulse shaper and discriminator. In the current front-end electronics, the ASD-8 [New93] ASIC comprises the above modules. Due to limitations of the current on-board time to digital converters (TDC), especially regarding higher reaction rates expected at the future FAIR facility (HADES at SIS-100), the electronics need to be replaced by new boards featuring multi-hit TDCs. Whereas ASD-8 chips cannot be procured anymore, a promising replacement candidate is the PASTTREC [Str17][Prz15] ASIC, developed by JU Krakow, which was tested w.r.t. suitability for MDC read-out in a variety of set-ups and, where possible, in direct comparison to ASD-8.

The timing precision, being the most crucial performance parameter of the joint system of detector and read-out electronics, was assessed in two different set-ups, i.e. a cosmic muon tracking set-up and a beam test at the COSY accelerator at Juelich using a minimum ionizing proton beam.

The beam test results were reproduced and can thus be quantitatively explained in a three dimensional GARFIELD simulation of a HADES MDC drift cell. In particular, the simulation is able to describe the characteristic dependence of the time precision on the track position within the cell.

A circuit simulation (SPICE) was used to closely model the time development of a raw drift chamber pulse, measured as a response to X-rays from a  $^{55}\text{Fe}$  source. The insights gained from this model were used for attributing realistic charge values to the time over threshold values measured with the read-out ASICs in a charge calibration set-up. Furthermore, a high-level circuit simulation of the PASTTREC shaper is implemented to serve as a demonstration of the effect of the individual shaping and tail cancellation stages which are present in both ASICs.



# Contents

<b>1</b>	<b>Introduction</b>	<b>1</b>
1.1	Aspects of heavy ion collisions - HADES physics . . . . .	1
1.2	The HADES experiment . . . . .	1
1.3	HADES at SIS100 . . . . .	4
1.4	Objective of this thesis . . . . .	4
<b>2</b>	<b>Operational aspects of the HADES drift chambers</b>	<b>7</b>
2.1	The HADES drift chamber system . . . . .	7
2.2	Interaction of charged particles with gasses . . . . .	9
2.3	Operation of an ideal proportional counter . . . . .	11
2.3.1	Electrode configuration and electric field . . . . .	11
2.3.2	Impedance and signal propagation . . . . .	12
2.3.3	Charge transport in the detector gas . . . . .	13
2.3.4	Electron diffusion . . . . .	13
2.3.5	Gas amplification . . . . .	14
2.3.6	Time development of the signal . . . . .	15
2.3.7	Shockley-Ramo theorem . . . . .	16
2.3.8	Ion induced signal current . . . . .	17
2.4	A model for the MDC I raw signal . . . . .	18
2.4.1	Impulse response functions . . . . .	18
2.4.2	Sampling the real-life detector response . . . . .	20
2.4.3	$^{55}\text{Fe}$ X-ray source ionization . . . . .	20
2.4.4	Simple drift cell model . . . . .	22
2.4.5	Transmission line drift cell model . . . . .	24
2.5	Drift chamber read-out electronics . . . . .	25
2.5.1	Currently used and future MDC electronics . . . . .	27
2.5.2	Unipolar shaper . . . . .	28
2.5.3	Pole-Zero filter and tail cancellation . . . . .	30
2.5.4	The PASTTREC shaper . . . . .	32
<b>3</b>	<b>Extraction of drift time</b>	<b>37</b>
3.1	General considerations . . . . .	37
3.2	Time precision tests with cosmic muons . . . . .	40
3.2.1	Motivation . . . . .	40
3.2.2	Cosmic muons . . . . .	40
3.2.3	Self-tracking . . . . .	40
3.2.4	Set-up . . . . .	41
3.2.5	Front-end electronics and signal coupling . . . . .	43
3.2.6	ASIC settings . . . . .	45
3.2.7	Analysis . . . . .	45
3.2.8	Error analysis . . . . .	50
3.2.9	Results . . . . .	55
3.3	Time precision tests with proton beam . . . . .	56
3.3.1	Motivation . . . . .	56
3.3.2	Set-up . . . . .	56
3.3.3	Analysis . . . . .	58
3.3.4	ASIC settings . . . . .	67
3.3.5	Error analysis . . . . .	69

## Contents

3.3.6	Self-Tracking . . . . .	73
3.3.7	Self-Tracking error . . . . .	76
3.3.8	Results . . . . .	76
3.4	Summary and discussion of drift time precision measurements . . . . .	79
<b>4</b>	<b>Measuring energy loss</b>	<b>81</b>
4.1	ASIC settings . . . . .	81
4.2	Recording the charge calibration function . . . . .	81
4.2.1	Intrinsic charge measurement precision of electronics . . . . .	83
4.2.2	Intrinsic time measurement precision of electronics . . . . .	84
4.3	Charge measurement precision with $^{55}\text{Fe}$ source . . . . .	85
4.3.1	Ionization by $^{55}\text{Fe}$ radiation in Argon, escape peak . . . . .	85
4.3.2	Analysis . . . . .	85
4.3.3	Results . . . . .	86
4.4	Charge measurement of minimum ionizing particles with PASTTREC . . . . .	88
<b>5</b>	<b>Simulation</b>	<b>91</b>
5.1	Cell geometry . . . . .	91
5.2	Field geometry . . . . .	91
5.3	Electron drift velocity . . . . .	95
5.4	Simulation of the beam test . . . . .	96
5.5	Comparison to experimental beam test data . . . . .	100
<b>6</b>	<b>Summary and outlook</b>	<b>103</b>
<b>7</b>	<b>Zusammenfassung</b>	<b>106</b>
<b>A</b>	<b>Appendix</b>	<b>113</b>
A.1	Flex print cable capacitance . . . . .	113
A.2	Skew normal distribution . . . . .	114
A.3	$^{55}\text{Fe}$ charge spectra recorded with PASTTREC . . . . .	116
A.4	Beam test MIPS charge spectra, PASTTREC . . . . .	118
A.5	Table of ASD-8 thresholds . . . . .	120
	<b>References</b>	<b>123</b>
	<b>Danksagung</b>	<b>127</b>

# 1 Introduction

## 1.1 Aspects of heavy ion collisions - HADES physics

An important topic in modern particle physics is the study of hadronic matter. Under normal conditions, stable hadrons, i.e. protons and neutrons, form atomic nuclei. By colliding heavy nuclei, particle accelerators grant an experimental access to hot and compressed hadronic matter. Systematic studies of such exotic matter states in the laboratory provide insights into the matter states present in the early universe and into astrophysical processes and phenomena, such as supernovas and colliding neutron stars [Ste18].

In a heavy ion collision one distinguishes three distinct phases. In the first phase, the compression phase, the overlapping parts of the two colliding nuclei are being compressed to several times the normal nuclear density. In a number of individual elastic and inelastic scattering events, initial linear momentum of the colliding nucleons is randomized and thus converted to heat. This phase lasts for circa  $10^{-22}$  s only.

After the initial compression phase the system expands and the local energy density decreases. Inelastic interactions between the reaction products cease beneath a characteristic energy density threshold. This is called the chemical freeze-out, since thereafter the amounts of the different sorts of created particles stays constant (apart from resonance decays). At a further state of expansion, elastic interactions cease, and one speaks of the kinematic freeze-out, since the individual particle momenta remain constant.

Hadrons are made of quarks which are confined into color neutral groups of two or three by the strong force, which is transmitted via gluons. The coupling constant of the strong force is dependent on the momentum transfer. For high momentum transfer, the coupling constant is small and thus the interaction can be described via perturbation theory. For low momentum transfer, this approach is invalid. An alternative attempt for describing low energy hadronic matter is pursued by so-called effective approaches, which consider the mesonic and baryonic degrees of freedom. An important prediction of these models is a change in hadron properties when embedded in nuclear matter relative to the hadron's properties in the vacuum.

Of special interest is the in-medium modification of the spectral functions of the light vector mesons  $\rho$ ,  $\omega$  and  $\phi$ . These have very short lifetimes and decay already during the course of a heavy ion collision. Vector mesons mainly decay via hadronic channels. However, with a probability of circa  $10^{-4}$ , a vector meson decays into an  $e^+e^-$  pair which does not participate in strong interaction and consequently escapes the expanding nuclear fireball undisturbed. By reconstructing the invariant mass of the dilepton pair one has access to the mass and decay width of the vector meson at the time of its decay.

Because the  $\rho$  meson is particularly short lived (1.3 fm/c) it decays predominantly in the compression phase of the collision, making it a preeminent probe of compressed hadronic matter. Effective models predict a significant in-medium broadening of the  $\rho$  decay width and a decrease of the invariant mass already at normal nuclear matter density [RW99]. Further, measuring the medium modifications of the vector mesons is expected to yield information about the restoration of chiral symmetry in hot and dense nuclear matter.

## 1.2 The HADES experiment

The High-Acceptance DiElectron Spectrometer (HADES), located at GSI Helmholtzzentrum für Schwerionenforschung is a fixed target experiment designed for the study of

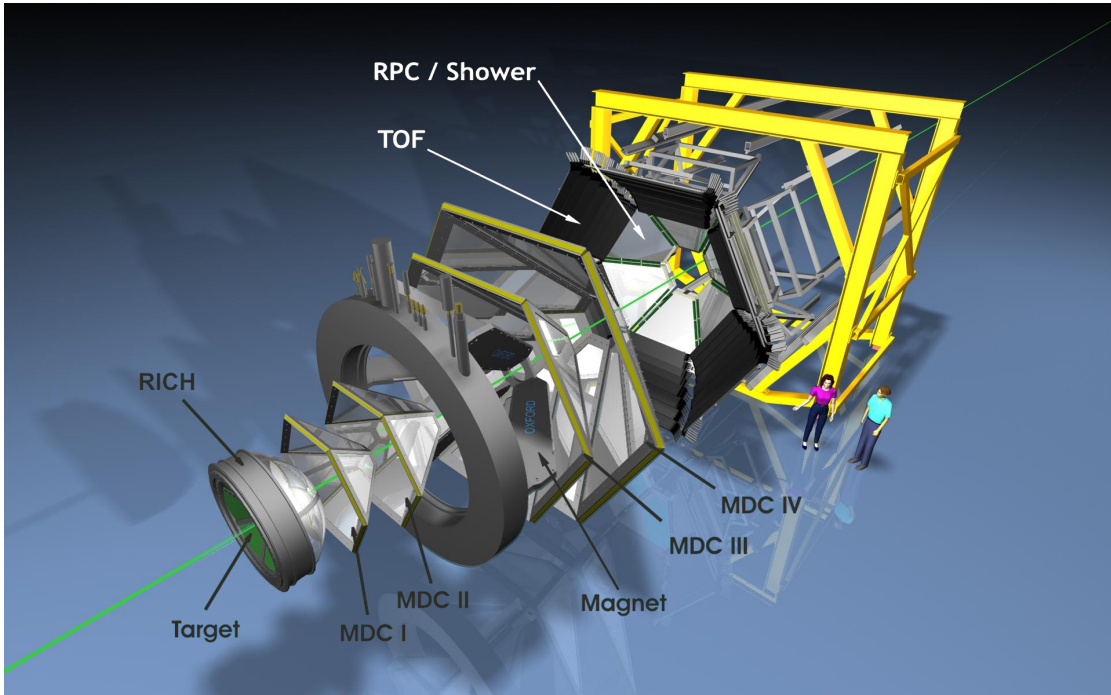


Figure 1.1: A CGI explosion view of the HADES detector

in-medium modifications of light vector mesons. HADES is supplied heavy ion and elementary particle beams in an energy regime of 1 AGeV to 2 AGeV by the SIS18 accelerator. This kinetic beam energy range covers the  $\rho$  meson production threshold. In the compression phase of the accessible heavy ion collisions, nuclear matter temperatures of  $T = 40$  MeV to 80 MeV and baryon densities of up to three times normal nuclear matter density are reached [Had09]. Complementary to the collisions of heavy nuclei, experiments with proton and pion beams on heavy nuclei, as well as proton and pion beams on hydrogen were conducted. In contrast to heavy ion collisions, elementary reactions, i.e. pion or proton induced reactions, embed vector mesons in normal nuclear matter [Aga09].

The processes in the collisions cannot be observed directly. The detectors can only measure the end states of the reaction products after the kinetic freeze out. While hadronic reaction products are abundant in a heavy ion collision, dileptons, which are the observables of interest, are rare. In order to trigger on di-electron candidates, a hadron blind ring imaging cherenkov counter is used, selecting interesting events in real time. Nevertheless, the data acquisition system has to be able to handle measuring up to 200 individual charged particle trajectories in a central heavy ion collision (Au + Au).

Figure 1.1 shows an explosion view of the HADES detector assembly. Closest to the target is located the above-mentioned ring imaging cherenkov detector (RICH) for identifying electrons. Going further downbeam, there are two layers of drift chambers (MDC I,II), a superconducting toroidal magnet and two additional layers of drift chambers (MDC III,IV), followed by the META (Multiplicity Electron Trigger Array) detector (TOF, RPC). Not included in the figure is the diamond detector, located directly in front of the target, and the forward wall which is placed behind all other systems.

The diamond detector, or start detector, serves to measure the start time of a potential collision event, i.e. the advent of a beam particle. The drift chambers represent the main tracking detector system of HADES. Together with the magnet, the four tracking



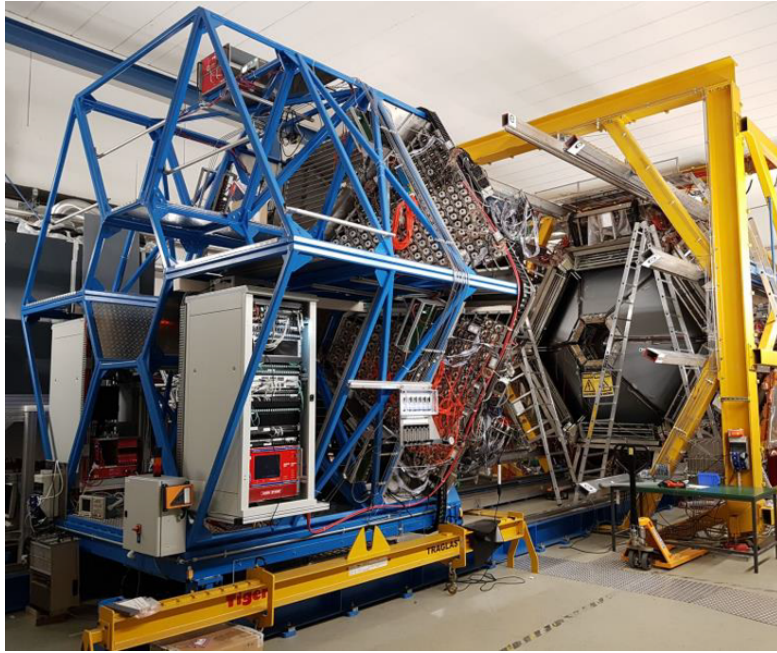


Figure 1.2: A photograph of the HADES detector from the rear, with the electromagnetic calorimeter prominently visible on the left

stations form a magnet spectrometer for determining the momentum of the particle via its deflection in the magnetic field. The META detector is a fast segmented detector for measuring the time of flight of particles (versus the diamond start detector) as well as providing a means to trigger on events above a certain track multiplicity. The forward wall is a scintillator array covering small polar angles. It serves to determine the reaction plane of the collision, by measuring the spectators, i.e. projectile nucleons not taking part in the collision.

Particle identification is achieved by comparing the momentum and the time of flight (velocity) of a particle, and thus obtaining information about its mass. Alternatively the momentum is compared with the energy loss in the drift chamber gas, which is also a function of velocity. In practice, both methods are combined.

In the most recent configuration of HADES, an electromagnetic calorimeter (ECAL) is added in between the META detector and the forward wall, prominently visible in the photograph in figure 1.2. The ECAL contributes to particle identification, especially electron/pion separation.

For the systematic study of vector meson decays, HADES features a high geometric acceptance for the leptonic decay products and a high precision in the determination of the invariant mass of the dilepton pairs. Neglecting the rest mass of the electron and the positron, the invariant mass of a dilepton pair is given by [Mar05]

$$M_{inv} \approx 2\sqrt{p_{e^+}p_{e^-}} \sin \frac{\alpha}{2}. \quad (1)$$

It depends on the measurement of the momenta and the opening angle  $\alpha$  between the electron and the positron trajectory. Both, the momentum and the opening angle measurement precision depend critically on the spatial precision of the drift chambers. The design goal of HADES is to achieve a relative precision of 1% in the invariant mass range of the  $\rho$  meson, which requires a spatial precision of the drift chambers of  $100 \mu\text{m}$

in the direction of magnetic deflection in the spectrometer. For a single drift cell, this requirement translates to a precision of  $150\ \mu\text{m}$  [Mar05].

### 1.3 HADES at SIS100

To achieve a full understanding of the properties of hadrons in nuclear matter, it is necessary to combine complementary results from different regions of the nuclear matter phase diagram. FAIR (Facility for Antiproton and Ion Research), which is currently under construction in Darmstadt, will physically and functionally extend GSI. Its synchrotron, SIS100 will provide beams with higher energy and intensity than the currently operating SIS18. It is foreseen to relocate the entire HADES detector to be operated at the same beam line as CBM (Compressed Baryonic Matter) [CBM09], the future dedicated FAIR heavy ion experiment. SIS100 will grant access to heavy ion collisions at beam energies ranging from 2 AGeV to 10 AGeV, an energy regime for which no experimental dilepton data exists so far. At the SIS100 energies, much higher matter densities can be achieved than with SIS18, while the temperature is expected to stay below the transition threshold to quark-gluon-plasma. A significant enhancement in the production of vector mesons is expected [Had09], as well as an overall increase in the number of hadronic reaction end products.

While HADES and CBM are both fixed target experiments with overlapping physics questions, in particular dielectron spectroscopy of vector mesons, the experiments differ in geometric acceptance and detector technology. HADES was designed for beam energies of 1 AGeV to 2 AGeV and thus its high geometric acceptance ranging from  $18^\circ$  to  $85^\circ$  polar angle accommodates collision products with a certain Lorentz boost. Since CBM was directly designed for the higher SIS100 energies, its geometric acceptance,  $3^\circ$  to  $25^\circ$  is tailored to a respectively higher Lorentz boost. For a beam energy around 4 AGeV, the mid-rapidity (for the light hadrons) of the collision system is boosted to polar angles within the overlap of the HADES and the CBM acceptance. Consequently, to attain a complete picture of the energy regime, the complementary results from HADES ( $\leq 4$  AGeV) and CBM (above  $\geq 4$  AGeV) need to be combined, while the common overlap region allows for testing the consistency of both experiments.

Benefiting of the high acceptance of HADES, it is possible to carry out multi-differential analyses, which in turn demand high statistics to ensure high data quality. Neither the storage bandwidth nor the reaction rates at SIS100 will be the limiting factor on experiment statistics, whereas the current drift chamber read-out electronics introduce limitations due to slow data read-out. Furthermore, the missing multi-hit capability of the signal digitization circuits (Time to Digital Converters) will lead to challenges regarding the higher track densities expected at SIS100. In order to cope with the stricter requirements on the drift chamber performance, the HADES MDC system needs to be upgraded with new front-end electronics, employing an improved digital read-out concept. Because also the current analog part of the MDC read-out is identified as a source of instability and inefficiency, due to its sensitivity to electromagnetic interference and its inclination to self-oscillation, an analog replacement technology is investigated.

### 1.4 Objective of this thesis

In this thesis an alternative integrated analog read-out circuit, the PASTTREC ASIC is investigated as a potential replacement for its counterpart in the existing HADES MDC front-end electronics, the ASD-8 ASIC. PASTTREC is tested, wherever possible, in direct comparison to ASD-8. The ultimate goal is to achieve optimal detector

performance in terms of spatial measurement precision, energy measurement precision and efficiency/reliability. This endeavor requires a detailed understanding the HADES drift chambers, which can be seen as an array comprising a large number of individual proportional counters.

In chapter 2, the fundamental working principles of proportional counters are discussed with an emphasis on a quantitative understanding of the resulting electrical output signal. The theoretical insights are integrated into an electrical circuit simulation to model and recreate the concrete MDC cell raw signal response to a delta-like stimulus. Further, the different analog signal shaping stages, present in both read-out ASICs are discussed on the basis of an idealized high level circuit simulation of the PASTTREC ASIC.

In chapter 3, an MDC cell is considered as a detector yielding spatial information via the arrival time (drift time) of the drifting ionization charges deposited in the detector gas by charged particle tracks. The previous chapter provides an understanding of the complete signal generation and analog signal processing chain. On the basis of these insights, the limiting factors for the precise determination of the drift time are discussed, which ultimately limit the spatial measurement precision of the detector. The drift time measurement precision is assessed in two different test set-ups enabling a comparison between both ASICs. The first set-up is used to track cosmic muons, while the second set-up is operated at an accelerator providing minimum ionizing protons. The latter provides a means to measure the space-time relation of the drift cell, as well as the time precision as a function of the distance from the sense wire.

Chapter 4 investigates charge measurement. Both ASICs measure charge indirectly via the time over threshold method. A procedure is introduced for determining the calibration function which converts between between logical pulse length and charge. In this context, too, the quantitative understanding of the MDC pulse shape is of importance. The consistency of the PASTTREC calibration is examined systematically by irradiating MDC cells with a radioactive  $^{55}\text{Fe}$  source.

Lastly, in chapter 5 an MDC cell (MDC I) is simulated in GARFIELD [GAR] a dedicated gas detector simulation framework. Apart from studying the electric field strength and the drift velocity as a function of position within the cell, the simulation is used to recreate and interpret the beam test results.

## 1 Introduction

## 2 Operational aspects of the HADES drift chambers

### 2.1 The HADES drift chamber system

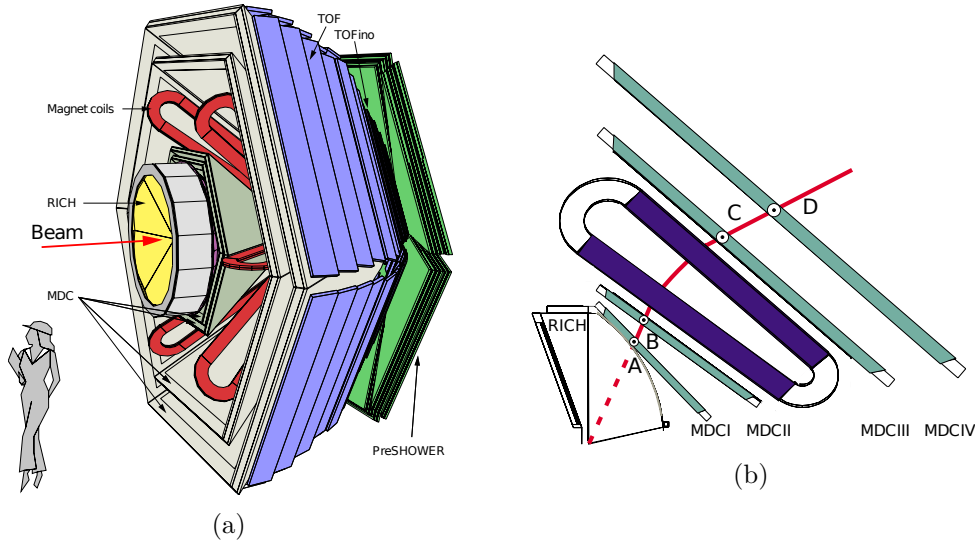


Figure 2.1: A sketch of the HADES detector in measurement position (a) and a cross section through one of six sectors of the magnet spectrometer comprising MDC and the superconducting magnet (blue coil) (b). Images taken from [Mar05].

The **Mini Drift Chamber** (MDC) system of the HADES experiment comprises four planes of drift chambers (MDC I to MDC IV). Each plane is composed of six identical trapezoidal chambers, arranged in a shape similar to an umbrella. In the experiment these structures are stacked into each other, so they form a concentric tracking detector system in the forward direction around the target on the beam axis (see Figure 2.1a). An ironless superconducting magnet, consisting of six coils, creates a toroidal magnetic field which is mostly confined to the space between MDC planes II and III. Charged particle trajectories are bent in this region due to the Lorentz force (Figure 2.1b). By reconstructing the amount of deflection, it is possible to determine the momentum of the particle if its charge is known.

Each chamber comprises thirteen internal layers of wires: six read-out layers, interleaved with seven cathode layers. The wires of the read-out layers are oriented at different stereo angles relative to the two center read-out layers (see Figure 2.2), so  $x$  and  $y$  position of a traversing particle can be determined within the plane of the drift chamber. While cathode layers consist of identical wires at a common electrical potential, the read-out layers feature an alternating sequence of so-called field wires and sense wires. Consequently each sense wire is in the center of a spatial volume that is confined by either a cathode wire or a field wire. In the normal operation, the chamber is filled with a special gas mixture and the cathode and field wires are kept at a negative electric potential via a high voltage power supply. The sense wire however, remains at ground potential and thus becomes the anode of an individual gas detector cell (Figure 2.3). In the following, such a cell is called a drift cell. The described structure is the same for all MDC planes/chambers, while the wire and layer pitch as well as the overall size of the chambers increases from the inner towards the outer planes. The smallest MDC drift cells possess a cross section of  $5 \times 5 \text{ mm}^2$  (MDC I) while the largest measure  $14 \times 10 \text{ mm}^2$  (MDC IV). See all MDC wire geometries listed in table 2.1.

## 2 Operational aspects of the HADES drift chambers

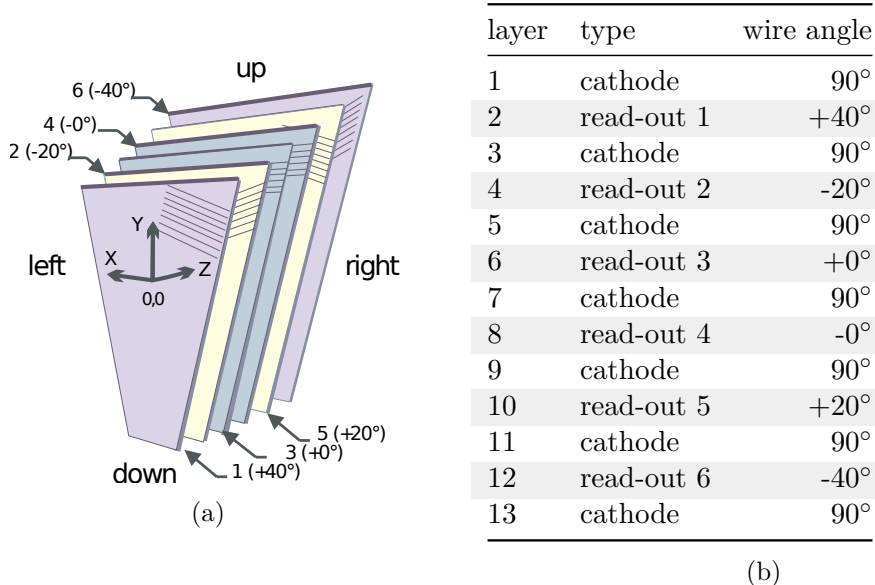


Figure 2.2: Layer order and wire orientation in all HADES drift chambers. The sketch (a) on the left omits the cathode layers.

MDC plane	cathode pitch	layer pitch	sense/field wire pitch
I	2.0 mm	2.5 mm	2.5 mm
II	2.0 mm	2.5 mm	3.0 mm
III	3.0 mm	4.0 mm	6.0 mm
IV	4.0 mm	5.0 mm	7.0 mm

	sense wire radius	cath. wire radius	field wire radius
I - III	10 $\mu\text{m}$	40 $\mu\text{m}$	40 $\mu\text{m}$
IV	15 $\mu\text{m}$	50 $\mu\text{m}$	50 $\mu\text{m}$

Table 2.1: Wire geometries of all MDC planes

When a charged particle traverses the active volume of a drift cell, it ionizes the detector gas along its trajectory. The free electrons created in the process will drift towards the anode of electrode configuration, i.e. the sense wire, while the remaining gas ions drift towards the negatively charged field and cathode wires. Above a certain operating voltage the cell acts as a proportional counter: The electric field in the direct vicinity (few tens of  $\mu\text{m}$ ) of the sense wire accelerates the drifting electrons to kinetic energies sufficient to ionize the detector gas themselves. Consequently an avalanche process multiplies the charge collected at the anode by a large but ideally constant factor (up to several  $10^4$  [Sau77]). Exploiting the gas amplification process, the electric charge signal arriving at the sense wire is large enough to be tapped and registered with an electronic measurement amplifier.

In the MDC system, the signal read-out electronics, comprising amplifier, analog signal processing and digitization circuitry, are mounted on the frames of the drift chambers and are connected to the sense wires via flex-print cables (FPC) with varying lengths from 11 cm to 28 cm.

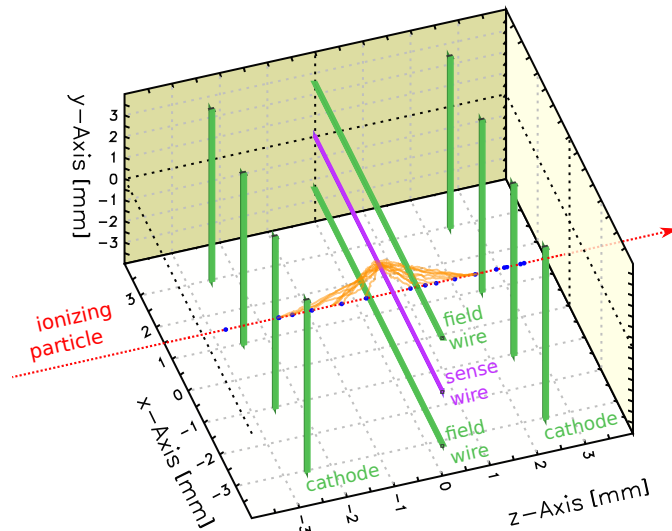


Figure 2.3: Zoom inside the wire geometry of an MDC I chamber. Shown is a  $0^\circ$  read-out layer sandwiched between two ( $90^\circ$ ) cathode layers. The wire geometry is shown in correct scale while the wire diameters are exaggerated.

In principle the signal from a drift chamber can provide the following information:

**The advent of a charged particle:** A charged particle or other form of ionizing radiation must have hit the drift cell. The spatial position of the charged particle's trajectory is known in one dimension with a resolution corresponding to the width of the drift cell.

**The radial distance of the particle trajectory from sense wire:** Given another (fast) detector measured the point in time when the charged particle passed through the drift cell. Relative to this detector the drift cell signal is delayed due to the finite time needed by the ionization electrons to drift to the sense wire. This delay is a function of the distance between track and sense wire. This information greatly increases the spatial measurement precision of the detector.

**The energy loss of the particle in the drift cell gas:** When all ionization electrons originating from the particle track have been collected and their charge has been multiplied by the gas amplification process, the integrated charge signal at the sense wire is proportional to the total ionization caused by the impinging particle. In HADES, the specific energy loss, among other observables, contributes to identifying the particle species.

Like any other detector system, the HADES drift chambers have limitations regarding the precision to which the corresponding observables can be measured. In order to understand these limitations and to optimize the measurement quality one has to understand the nature and the shape of the electrical drift chamber signal.

## 2.2 Interaction of charged particles with gasses

The fundamental principle of particle detection is the interaction of particles with an arbitrary detector medium. In the case of drift chambers the detector medium is a gas and the relevant mechanism is the electromagnetic interaction between fast, charged

## 2 Operational aspects of the HADES drift chambers

particles and gas atoms or molecules. The measured quantity is the amount (and the location) of ionization in the detector gas.

When an impinging charged particle knocks out an electron from neutral gas atom in an inelastic scattering event, one speaks of *primary ionization*. In many cases, the kinetic energy of the primary ionization electron is high enough to ionize further gas atoms, which is termed *secondary ionization*. In case of low energy transfer, inelastic scattering can lead to atomic excitation of gas atoms instead of ionization. Especially in gas mixtures, it is possible that the excitation energy is transferred to a different atom with lower ionization energy which is consequently ionized. This process also contributes to secondary ionization. The sum of primary and secondary ionization is referred to as the *total ionization*. Because ionizing a gas requires energy, there is a relation between the energy loss  $\Delta E$  of a charged particle and the total number  $n_T$  of electron/ion pairs (primary + secondary) created in the detector medium [Sau77]:

$$n_T = \frac{\Delta E}{W_i} \quad (2)$$

with  $W_i$  being the ionization energy of the gas ( $\approx 30$  eV). Due to the statistical nature of inelastic scattering, the ionization is unevenly distributed along the particle trajectory, and, because of the abovementioned secondary ionization processes, the deposited charge is concentrated in localized ionization clusters with variable number of charges (typically one to three [Mar05]). The mean energy loss per unit length  $\langle dE/dx \rangle$  (or “stopping power”) of a charged particle in a given material can be described by the Bethe-Bloch formula [PDG10]:

$$-\left\langle \frac{dE}{dx} \right\rangle = 4\pi N_A r_e^2 m_e c^2 \frac{Z}{A} \frac{z^2}{\beta^2} \left[ \frac{1}{2} \ln \left( \frac{2c^2 m_e \gamma^2 \beta^2 T_{max}}{I^2} \right) - \beta^2 - \frac{\delta(\beta\gamma)}{2} \right] \quad (3)$$

- with  $N_A$  – Avogadro’s number
- $r_e$  – classical electron radius
- $m_e$  – electron mass
- $Z, A$  – atomic number and atomic mass of material
- $z$  – charge of impinging particle
- $I$  – material ionization constant
- $\gamma$  – Lorentz factor
- $\delta$  – density effect correction to ionization energy loss

$T_{max}$  is the maximum possible kinetic energy transferred to a free electron by the impinging particle with mass  $M$ :

$$T_{max} = \frac{2m_e c^2 \beta^2 \gamma^2}{1 + 2\gamma m_e/M + (m_e/M)^2} \quad (4)$$

A peculiar feature of the energy loss is its relative independence from the impinging particle mass (species). The energy loss is mainly determined by a particle’s charge and  $\beta\gamma = \frac{p}{Mc}$ , which is a mere function of its velocity. This fact can be exploited for particle identification: When the particle’s momentum is known, measuring the specific energy



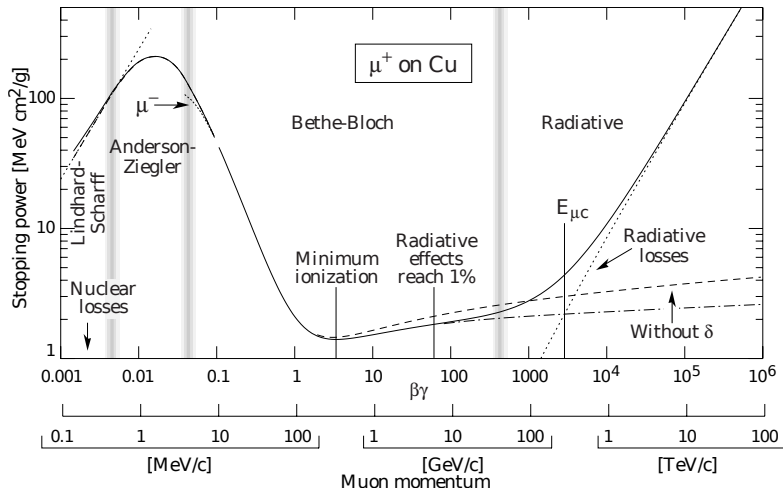


Figure 2.4: Mean stopping power ( $-dE/dx$ ) for positive muons passing through copper. The Bethe-Bloch formula describes the velocity region  $0.1 < \beta\gamma < 1000$ . The dependence of the energy loss function on  $\beta\gamma$  ( $\sim$ velocity) is nearly identical for all particles and similar for all materials. Source: [PDG10].

loss, in principle, yields the particle's mass  $M$ . Furthermore, when normalized to the material mass-density, the energy loss depends only weakly on the material properties, so the stopping powers of all materials are in the same order of magnitude and follow the same dependence on  $\beta\gamma$ . As a representative example, the energy loss of muons in copper is depicted in figure 2.4. Obviously the energy loss has a minimum. In fact, all charged particles become *minimum ionizing particles* (MIPs) at a certain velocity, i.e. when  $\beta\gamma \approx 3$ . MIPs play a special role in the design considerations of particle detectors: They produce the least amount of detectable signal charge, so they represent the most challenging special case that the detector must handle.

When a charged particle loses only a small fraction of its kinetic energy in a relatively small number of individual inelastic scattering events, e.g. by passing through a drift chamber, the total deposited energy is subject to large fluctuations following a non-Gaussian probability distribution. The energy loss distribution is described by the asymmetric Landau distribution [Sau77], which possesses a prominent tail towards large energy losses. The theoretical Landau distribution does not have a defined statistical mean and is thus characterized in terms of its most probable energy loss  $(\Delta E)_{mp}$ :

$$P(\Delta E) = P(\lambda) = \frac{1}{\sqrt{2\pi}} \exp\left(-\frac{1}{2}(\lambda + e^{-\lambda})\right) \quad (5)$$

$$\lambda = \frac{\Delta E - (\Delta E)_{mp}}{\langle \Delta E \rangle} \quad (6)$$

Here  $\lambda$  is the deviation from the most probable energy loss, normalized to the mean energy loss  $\langle \Delta E \rangle$  described by the Bethe-Bloch formula.

## 2.3 Operation of an ideal proportional counter

### 2.3.1 Electrode configuration and electric field

The most simple and ideal realization of a proportional counter is a gas-filled conductive cylinder of length  $l$  with a thin metal wire spanning along its central axis (see Figure 2.5).

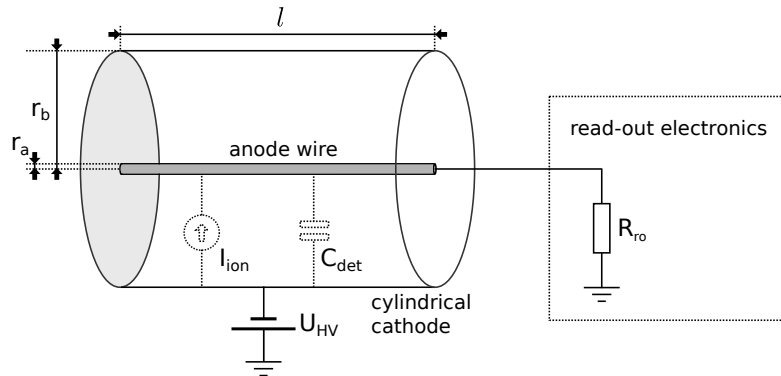


Figure 2.5: Schematic of a basic proportional counter in form of a cylindrical drift tube

A voltage is applied, so that the wire (anode) is positively charged relative to the cylinder (cathode). Such a configuration is called a drift tube. In analogy to the HADES drift chambers a negative high voltage  $-U_{HV}$  is applied to the cathode, while the anode is connected to ground potential<sup>1</sup> via the read-out electronics, here idealized as an ohmic resistor  $R_{ro}$ . Since the cylindrical anode wire (radius  $r_a$ ) and the cathode cylinder (radius  $r_b$ ) form an ideal cylindrical capacitor, the electric field inside the cylinder is well known and can be expressed as a function of radial position  $r$  relative to the central axis.

$$E(r) = \frac{U_{HV}}{\ln(r_b/r_a)} \cdot \frac{1}{r} \quad (7)$$

It will be shown in chapter 5, that the inner part of an MDC drift cell has a very similar electric field geometry and may very well be approximated by a drift tube, especially w.r.t. the electric signal properties.

### 2.3.2 Impedance and signal propagation

In principle an elongated drift tube is a coaxial cable. The capacitance and inductance per unit length can be calculated from the geometric parameters [RF18]:

$$C_{det} = C' \cdot l, \quad L_{det} = L' \cdot l \quad (8)$$

$$C' = \frac{2\pi\epsilon_0\epsilon_r}{\ln(r_b/r_a)} \quad (9)$$

$$L' = \frac{\mu_0\mu_r}{2\pi} \cdot \ln(r_b/r_a) \quad (10)$$

If the resistance of the conductors can be neglected, the impedance of the cable is [Dem09]:

$$Z = \sqrt{\frac{L'}{C'}} = \sqrt{\frac{\mu_0\mu_r}{4\pi^2\epsilon_0\epsilon_r}} \ln(r_b/r_a) \quad (11)$$

The dielectric constant and the magnetic permeability of the tube filling is negligible, so  $\epsilon_r = 1$ ,  $\mu_r = 1$ . For a drift tube with  $r_b = 2.5$  mm and  $r_a = 10$   $\mu$ m this results in  $C' = 10.1$  pF/m,  $L' = 1.1$   $\mu$ H/m and an impedance of  $Z = 330$   $\Omega$ . This provides a suitable approximation for an MDC I cell, since the absolute size of the cell/tube ( $r_b$ )

<sup>1</sup>Note that in many other realizations of proportional counters, especially straw tubes, the cathode and not the anode is at ground potential for technical reasons. The working principle is the same, since the electric field is indifferent to offsets in the absolute electrical potential.

affects the results only weakly due to the logarithm. With negligible material constants, signals propagate along the tube at the speed of light:

$$v = \frac{1}{\sqrt{\varepsilon\mu}} = \frac{c_0}{\sqrt{\varepsilon_r\mu_r}} = c_0 \quad (12)$$

### 2.3.3 Charge transport in the detector gas

Ionizing radiation creates gas ions and free electrons in the detector gas in equal numbers. In the electric field these particles immediately start to drift in radial direction towards the respective oppositely charged electrode. That means, of course, that the free electrons drift to the anode wire. The drift of a charged particle in an external field is a continuous microscopic sequence of acceleration, i.e. gain of kinetic energy, followed by collision with gas atoms/molecules, where the kinetic energy is lost again. A characteristic parameter of the scattering process is the mean free path, which is of the order of several  $\mu\text{m}$ . In the macroscopic picture an equilibrium is reached between acceleration and scattering and the effective electron or ion velocity is proportional to the local electric field via the particle's mobility coefficient:  $\mu^+$  (ions),  $\mu^-$  (electrons).

$$\frac{dr}{dt} = \mu^\pm \cdot \frac{E(r)}{P} \quad (13)$$

The drift velocity is further inversely proportional to the gas pressure  $P$ , since a higher gas density directly reduces the mean free path length. The ratio  $E/P$  is often referred to as the reduced electric field. Electrons and ions possess greatly different mobilities, i.e. electrons usually drift about a factor of thousand faster than ions. Typical electron drift velocities in proportional counters are of the order of  $50 \mu\text{m ns}^{-1}$ [Sau77]. While ions lose large fractions of their momentum when colliding with equally heavy gas atoms, the much lighter electrons merely have their momentum vector randomized to some degree. They lose however momentum on average over several collisions[BR08]. Further, kinetic energy is lost in inelastic scattering leading to electronic excitation, vibrational and rotational excitation in molecular gasses, and at higher energies even ionization (above 10 eV).

Due to quantum mechanical effects the scattering cross section (both elastic and inelastic) of electrons on gas atoms and molecules depends on the electron energy. Hence the mobility  $\mu^-$  is not a constant but a non-trivial function of the electric field strength itself. However, by carefully tuning the gas mixture and the operating voltage, this effect can be exploited to provide a relatively uniform electron drift velocity over a large part of the otherwise non-uniform electric field within the drift tube. To be accurate, it has to be noted that neither the ion mobility  $\mu^+$  is a constant. Its approximation as a constant, however, is far more applicable and sufficient for the following considerations.

### 2.3.4 Electron diffusion

While drifting through the detector gas, an electron has its momentum randomized each mean free path, when colliding with a gas particle. On average it moves in the direction of the electric field lines with the equilibrium drift velocity  $v_D$ , because the stochastic momentum transfer is isotropic. In other words, the microscopic trajectory of the electron can be pictured as a random walk superimposed on an idealized macroscopic drift trajectory. However, over time, the fluctuations add up in a random direction and the deviation between the microscopic and the ideal drift trajectory grows.

## 2 Operational aspects of the HADES drift chambers

When a large number of electrons is starting a uniform drift motion in  $z$  direction from the same origin, the electron density can be described by a Gaussian distribution [BR08]:

$$n(\vec{r}) = \left( \frac{1}{\sqrt{4\pi Dt}} \right)^3 \exp\left( \frac{-r^2}{4Dt} \right) \quad (14)$$

$$\text{with } \vec{r} = \begin{pmatrix} x \\ y \\ z - v_D \cdot t \end{pmatrix} \quad (15)$$

and the diffusion constant  $D$ . Consequently the width of the electron cloud increases with the square root of the elapsed time  $t$ , or expressed differently, with the traveled distance  $L$ :

$$\sigma_r = \sqrt{2D \cdot t} = \sqrt{\frac{2DL}{\mu^- E}} \quad (16)$$

Intuitively one assumes that the diffusive broadening of the charge distribution is isotropic in space, but in reality one observes that diffusion behaves different in longitudinal and transversal direction relative to the drift motion. This can be explained with the energy dependent, and thus velocity dependent, scattering cross section of electrons and gas particles. Since the leading and the trailing regions of the Gaussian charge distribution travel with different effective velocities, the respective electrons have different mobilities  $\mu^-$ . Quantitatively the effect can be described by using separate diffusion coefficients  $D_L$  and  $D_T$  in longitudinal and in transverse direction [BR08]:

$$n(\vec{r}) = \frac{1}{\sqrt{4\pi D_L t}} \cdot \left( \frac{1}{\sqrt{4\pi D_T t}} \right)^2 \exp\left( -\frac{x^2 + y^2}{4D_T t} - \frac{(z - v_D)^2}{4D_L t} \right) \quad (17)$$

$$\sigma_x = \sigma_y = \sqrt{2D_T \cdot t} \quad (18)$$

$$\sigma_z = \sqrt{2D_L \cdot t} \quad (19)$$

### 2.3.5 Gas amplification

For normal operation conditions of the counter, the kinetic energy attained by the electrons between two collisions leads to mere elastic scattering or thermal excitation of the gas in the biggest part of the drift cell. Since the strength of the electric field greatly increases towards the anode wire ( $E \propto \frac{1}{r}$ ), the region where drifting electrons cause gas ionization can be tuned to few wire radii around the anode by setting the operating voltage accordingly. When entering this region, each incoming primary or secondary electron creates an avalanche, and the number of new free electrons and ions created doubles each mean free path. A frequently encountered quantity related to the gas amplification is the first Townsend coefficient. It is the inverse of the mean free path for ionization and it describes the number of ion pairs produced per unit length of drift [Sau77]. The largest fraction (one half) of the total ionization is produced in the last mean free path before the electrons are collected by the anode wire [Sau77]. This process is over in less than one nanosecond. Subsequently the remaining ions drift to the cathode. This drift process happens on a different time scale and can take up to milliseconds, until the ions arrive and are neutralized at their destination.

Typically, a drift chamber is operated with a noble gas. As discussed in section 2.2, charged particles lose energy in the detector gas through ionization and excitation. Obviously ionization is a desired process, since it creates signal charge. Excited electronic

states of noble gas atoms, however, can decay via emission of UV photons energetic enough to ionize other gas atoms. This is problematic when UV photons created in the amplification avalanche themselves trigger an avalanche outside the initial one, which results in a breakdown of the counter [Mar05]. The phenomenon drastically limits a stable operation of the proportional counter, especially for useful gas amplification factors. This limitation can be overcome by mixing the noble gas with hydrocarbons or CO<sub>2</sub>. The so-called quenching gas is polyatomic and thus possesses a number of low-energy vibrational and rotational excitation modes [Sau77], which effectively absorb and dissipate the energy of the UV photons.

Gas amplification factors between  $10^3$  and  $10^5$  can be achieved while preserving a proportionality between the initially deposited charge and the final charge signal. For amplification factors between  $10^5$  and  $10^8$  the proportionality is gradually lost [KW16]. With increasing high voltage, due to the low mobility of ions, more and more positive space charges are built up around the anode, which leads to a local reduction of the field, and thus to a saturation of the gas gain. This situation is reached even sooner for a high amount of initial ionization [KW16].

### 2.3.6 Time development of the signal

In the simplest picture the avalanche electrons simply enter the anode wire and generate a delta-function like current pulse. However, this picture is wrong, at least at the time scales of interest, i.e. 1 ns to 1  $\mu$ s. The following deduction of the signal shape is analogous to [KW16].

The drift tube is a capacitor holding a charge  $Q_{det} = C_{det} \cdot U_{HV}$ . In the avalanche, electron/ion pairs are created and separated by the capacitor's electric field. After the electrons are collected at the anode and the ions are neutralized at the cathode, the capacitor's charge is diminished by the exact same amount of charge that was separated in the avalanche. If it were not so, the law of charge conservation was violated. Since the detector capacitor is connected to an external voltage source (via the front-end electronics), it is recharged to its original charge state, and it is this recharging current that is registered by the outside world as the detector signal. Usually the change in charge and the corresponding voltage drop is very small compared to the initial voltage. Typical operation voltages are between 1 and 2 kV, while a typical signal causes a voltage drop by only few mV. This means that the dynamics of drifting charges in the gas are dominated by the initial electric field sustained by the high voltage supply, while the output signal corresponds to the small temporary modifications of this field.

A very important role for understanding the dynamics of the signal plays electrostatic induction. Even before the electrons/ions reach the anode/cathode their electric charge induces mirror charges of opposing sign in the surface of the surrounding electrodes. As an example, let us picture a single electron that is moved from infinite distance to the surface of a grounded electrode: In order to form the positive mirror charge, a net amount of one electron has to be pushed away from the electrode. It happens gradually, as the amount of displaced charge is a function of the distance. In fact, the moment when an electron enters the anode it merely recombines with its positive mirror charge and there is no momentary change in the output signal. The same holds true for the ions at the cathode.

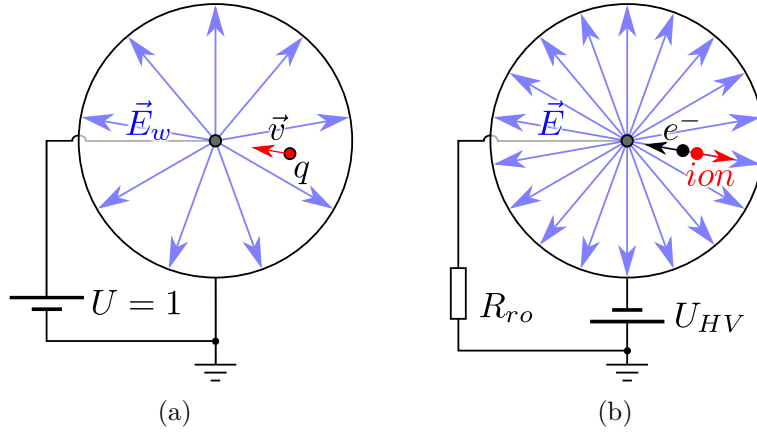


Figure 2.6: (a) Illustration of the theoretical weighting field inside the drift tube to calculate the current induced in the anode wire (b) Schematic depicting the real-world operation

### 2.3.7 Shockley-Ramo theorem

To quantify induced charges and currents we use the Shockley-Ramo theorem [KW16]. It states, that the current induced into a grounded electrode by a moving charge  $q$  is

$$I_{ind} = q\vec{E}_w \cdot \vec{v}, \quad (20)$$

with  $\vec{v}$  the velocity of the charge and  $\vec{E}_w$  the weighting field of the electrode configuration. The hypothetical weighting field is obtained by raising the electrode of interest to a unitless potential of 1 and grounding all other electrodes. In the special case of our drift tube, this means grounding the cathode cylinder and applying  $U = 1$  to the anode wire (as shown in Figure 2.6). The weighting field has the unit:  $[\vec{E}_w] = 1 \text{ m}^{-1}$ . Because of the cylinder symmetry and charges either radially drifting inwards or outwards, i.e. parallel to the electric field, the equation can be used in scalar form:

$$I_{ind} = -\frac{dQ_{ind}}{dt} = qE_w \cdot \frac{dr}{dt} \quad (21)$$

$$dQ_{ind} = -qE_w \cdot dr, \quad (22)$$

with  $Q_{ind}$  being the induced (displaced) charge. Analog to the real electrical field (7) we get:

$$E_w = \frac{1}{\ln r_b/r_a} \frac{1}{r}. \quad (23)$$

The output signal is not sensitive to the initial charge deposited by the ionizing radiation. It is dominated by orders of magnitude by the charge separated in the avalanche amplification process. In such an avalanche we can assume that  $N$  (approx.  $10^4$  to  $10^6$ ) electron/ion pairs are created at  $r_0 = r_a + \lambda$ , one mean free path length  $\lambda$  ( $\approx 1 \mu\text{m}$ ) away from the anode wire. Both, the drift of the electrons and the ions, contribute to the total induced charge:

$$Q_{ind}^{total} = Q_{ind}^{el} + Q_{ind}^{ion} = -Ne \quad (24)$$

The sign is negative because we are “collecting” negative charges at the anode. For our cylinder geometry we can arrive at [KW16]:

$$Q_{ind}^{el} = -(-Ne) \cdot \int_{r_0}^{r_a} \frac{1}{\ln r_b/r_a} \frac{1}{r} dr = -Ne \frac{\ln r_0/r_a}{\ln r_b/r_a} \quad (25)$$

$$Q_{ind}^{ion} = -(Ne) \cdot \int_{r_0}^{r_b} \frac{1}{\ln r_b/r_a} \frac{1}{r} dr = -Ne \frac{\ln r_b/r_0}{\ln r_b/r_a} \quad (26)$$

When we compare the signal fractions for real life parameters, we find, that the charge induced by the electrons is very small in relation. For  $r_a = 10 \mu\text{m}$ ,  $r_b = 2.5 \text{mm}$ ,  $r_0 = r_a + 1 \mu\text{m}$  we get:

$$\frac{Q_{ind}^{el}}{Q_{ind}^{ion}} = \frac{\ln r_0/r_a}{\ln r_b/r_0} = 1.76\%. \quad (27)$$

Therefore we will neglect the electron fraction in the following and deal only with the ion signal. Figuratively spoken, the avalanche electrons are created almost directly at the wire and then *become* the negative mirror charges for the positive ions which slowly drift away. Gradually these mirror charges (or rather an equivalent amount of negative charges) are released and leave the anode wire through the front-end electronics and thus *become* the output signal of the drift tube.

### 2.3.8 Ion induced signal current

After considering the absolute induced charge we are now interested in the time development of the current induced by the drifting avalanche ions. First we solve the equation of motion for drifting ions (13) for the case of a cylindrical electric field (7) and the boundary conditions  $r = r(t)$ ,  $r(0) = r_0$ :

$$\frac{dr}{dt} = \mu^+ \cdot \frac{E(r)}{P} = \frac{\mu^+}{P} \frac{U_{HV}}{\ln r_b/r_a} \cdot \frac{1}{r} \quad (28)$$

$$\int_{r_0}^{r(t)} r' dr' = \int_0^t \frac{\mu^+}{P} \frac{U_{HV}}{\ln r_b/r_a} dt' \quad (29)$$

$$\Rightarrow r(t) = \sqrt{r_0^2 + \frac{2\mu^+ U_{HV}}{P \cdot \ln r_b/r_a} t} \quad (30)$$

$$= r_0 \cdot \sqrt{1 + \frac{t}{t_0}}, \quad t_0 = \frac{r_0^2 P \cdot \ln r_b/r_a}{2\mu^+ U_{HV}}. \quad (31)$$

Now we plug this solution into the Shockley-Ramo equation to attain the ion current:

$$I_{ind}^{ion}(t) = qE_w(r(t)) \cdot \frac{dr}{dt} = -\frac{Ne}{\ln r_b/r_a} \frac{1}{r(t)} \cdot \frac{dr}{dt} \quad (32)$$

$$I_{ind}^{ion}(t) = -\frac{Ne}{2 \cdot \ln r_b/r_a} \frac{1}{t_0 + t}. \quad (33)$$

And by time integration we can calculate the absolute induced charge:

$$Q_{ind}^{total}(t) \approx Q_{ind}^{ion}(t) = \int_0^t -\frac{Ne}{2 \cdot \ln r_b/r_a} \frac{1}{t_0 + t'} dt' \quad (34)$$

$$= -\frac{Ne}{2 \cdot \ln r_b/r_a} \ln \left( 1 + \frac{t}{t_0} \right). \quad (35)$$

## 2 Operational aspects of the HADES drift chambers

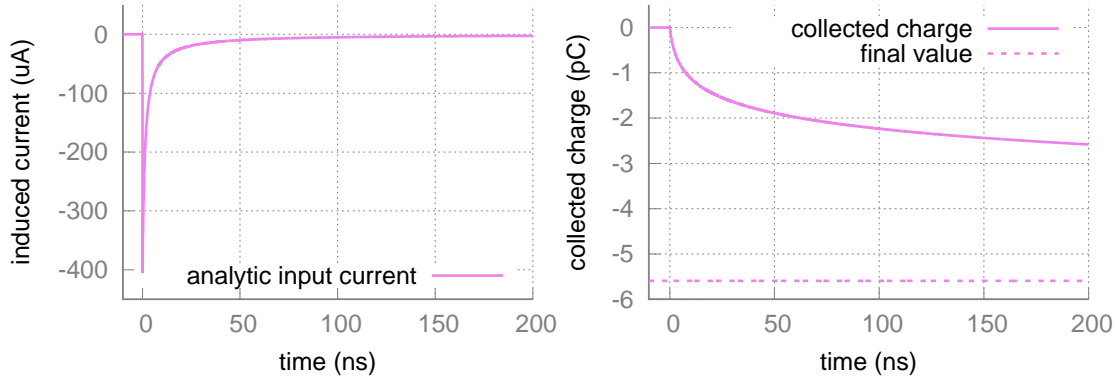


Figure 2.7: The theoretical current signal (left) and the charge signal (right) of an ideal cylindrical proportional counter with parameters  $r_a = 10 \mu\text{m}$ ,  $r_b = 2.5 \text{ mm}$ ,  $r_0 = r_a + 1 \mu\text{m}$ ,  $\mu_{Ar}^+ = 1.7 \text{ cm}^2\text{s}^{-1}\text{V}^{-1}\text{atm}^{-1}$ ,  $P = 1 \text{ atm}$ ,  $U_{HV} = 1600 \text{ V}$ . The total charge  $Q_{ind}$  after the gas amplification is  $35 \cdot 10^6 e = 5.6 \text{ pC}$ .

Further we can use (31) to calculate the time it takes for the ions to arrive at the cathode:

$$T^+ = t(r = r_b) = t_0 \frac{r_b^2 - r_0^2}{r_0^2}. \quad (36)$$

For an MDC I chamber ( $r_a = 10 \mu\text{m}$ ,  $r_b = 2.5 \text{ mm}$ ,  $r_0 = r_a + 1 \mu\text{m}$ ,  $\mu_{Ar}^+ = 1.7 \text{ cm}^2\text{s}^{-1}\text{V}^{-1}\text{atm}^{-1}$ ,  $P = 1 \text{ atm}$ ,  $U_{HV} = 1600 \text{ V}$ ) we calculate a maximum ion drift time of

$$T^+ = 63 \mu\text{s}. \quad (37)$$

Figure 2.7 shows a plot of both, the induced current and the induced charge. While after 100 ns the current pulse seems to have returned to the base line, only 40% of the total pulse charge has been collected. This is a feature of the characteristic time dependence ( $\propto \frac{1}{t}$ ) of the signal current, which is referred to as the “ion tail” of a proportional counter signal pulse.

### 2.4 A model for the MDC I raw signal

In the following we want to apply the theoretical considerations of the previous section to understand the raw analog signal at the output of a HADES MDC drift cell. At the moment we are not interested in the complex signals caused by particle tracks crossing a drift cell but in the detector response to a single ionization electron arriving at the anode wire. In the field of signal processing this is called the impulse response function.

#### 2.4.1 Impulse response functions

When a device has a scalar input and a scalar output variable and the output depends linearly on the input, and further the system does not change its properties over time, it is called a linear time-invariant (LTI) system. Such a system can be completely characterized by its impulse response function, which can be determined when the system is stimulated with a delta input pulse. Arbitrary output signals  $y(t)$  of the system can then be predicted by convoluting the respective input signal  $x(t)$  with the system’s



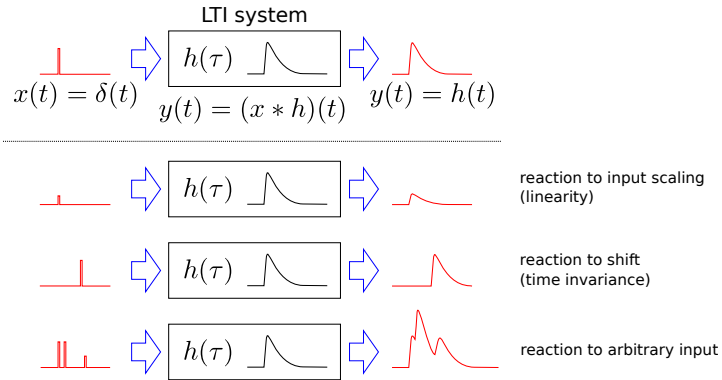


Figure 2.8: Illustration of the reaction of a linear time invariant (LTI) system to a delta stimulus and arbitrary stimuli.

impulse response function  $h(\tau)$  [Rug05]:

$$y(t) = (x * h)(t) \quad (38)$$

$$= \int_{-\infty}^{\infty} x(t - \tau) \cdot h(\tau) d\tau \quad (39)$$

$$= \int_{-\infty}^{\infty} x(\tau) \cdot h(t - \tau) d\tau \quad (40)$$

This concept is largely applied to electrical systems, e.g. networks of passive components and circuits including linear amplifiers. The input and output variables are then usually analog voltages. LTI systems have the elegant property, that when two such systems are connected in series, the resulting system is again an LTI system and the joint impulse response function is the convolution of the individual response functions. In the following, our drift chamber cell is also treated as an LTI system. Its input variable is the arrival time density of primary and secondary ionization electrons arriving at the anode and the output is the voltage drop on ( $\propto$  current into) the input impedance of the front-end electronics. Actually a full description of the drift cell includes a concatenation of two LTI subsystems, governed by different independent processes:

- The first system describes the ion induction current with its characteristic  $\propto \frac{1}{t}$  shape. This has been analytically solved in the previous section, by approximating an MDC drift cell as an idealized drift tube.
- The pre-charged drift cell capacity is discharged by the ion induction current. The second system describes the recharging of the cell capacitance via the front-end electronics and the signal pulse propagation in the cell.

The systems can be regarded as independent because the momentary changes in the voltage between anode and cathode are very small compared to the absolute operation voltage and thus the electric field, which governs the dynamics of the drifting avalanche electrons and ions, can be regarded as constant. This section tries to model the second process. Because of the mathematical complexity introduced with convolutions, a model for the second process is computed numerically using LTSPICE [SPI14], a software framework for the simulation of electronic circuits in the time domain.

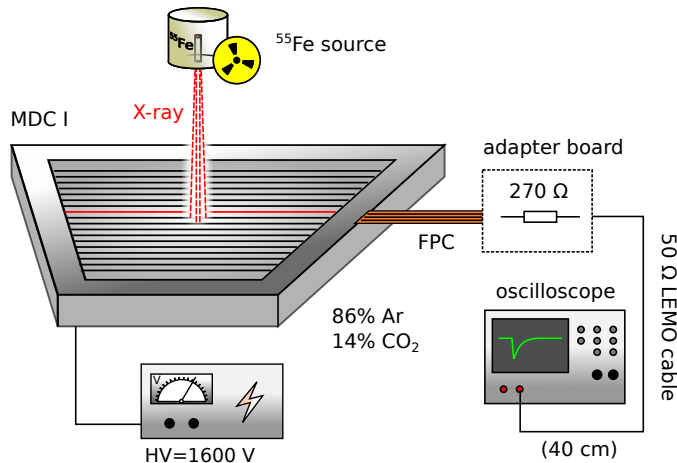


Figure 2.9: Sketch of the measurement set-up for studying the drift chamber signal shape.

### 2.4.2 Sampling the real-life detector response

To attain an sample of a typical drift chamber response signal, an MDC I chamber was brought into operation and irradiated with a radioactive  $^{55}\text{Fe}$  source while the analog signal of a single drift cell was sampled by means of an oscilloscope <sup>2</sup> (see figure 2.9). The chamber was operated at  $U_{HV} = 1600\text{ V}$  and with a gas mixture of 86 %Ar and 14 %CO<sub>2</sub>. The signal output of the MDC is a thin flex print cable (FPC). To couple the chamber to the oscilloscope, a small adapter board was used which features a matching flex print connector on one side and a LEMO (50  $\Omega$  laboratory cable) connector on the other side. On the adapter board a 270  $\Omega$  resistor is wired in series between chamber and oscilloscope to roughly match the impedance of the measurement device to the impedance of the detector cell. The waveform acquisition is started when a pulse with negative polarity falls below a threshold of  $-0.3\text{ mV}$ . To reduce noise and fluctuations, 1000 waveforms are recorded and averaged. The resulting waveform is depicted in figure 2.10.

### 2.4.3 $^{55}\text{Fe}$ X-ray source ionization

$^{55}\text{Fe}$  undergoes a  $\beta^+$  decay to form  $^{55}\text{Mn}$ . This process occurs via electron capture and leaves the  $^{55}\text{Mn}$  atom with a hole in the K shell. Subsequent filling of the hole emits or K- $\alpha$ -1 and K- $\alpha$ -2 X-rays with energies of 5.898 75 keV and 5.887 65 keV [LNHB18]. Because the energies are so similar, the X-ray radiation can be considered monochromatic for most applications.

In the following we consider a 5.9 keV photon interacting with the detector gas at a random position within the drift cell. Under the assumption that the entire energy  $\Delta E$  is converted to ionization, we can calculate the total number of electron/ion pairs created with the following formula [Sau77]:

$$n_T = \frac{\Delta E}{W_i} = \frac{5.9\text{ keV}}{27.0\text{ eV}} = 218.5 \quad (41)$$

For a 86 % argon ( $W_i = 26\text{ eV}$ ) and 14 % CO<sub>2</sub> ( $W_i = 33\text{ eV}$ ) mixture, we obtain a mean ionization energy of  $W_i = 0.86 \cdot 26\text{ eV} + 0.14 \cdot 33\text{ eV} = 27.0\text{ eV}$  <sup>3</sup>.

<sup>2</sup>Oscilloscope used is model “LeCroy Wavesurfer 64Xs” [LeC08] featuring an input bandwidth of 600 MHz.

<sup>3</sup>The weighted average of the gas mixture ionization energies is a simplified estimate, neglecting the microscopic interaction cross sections.

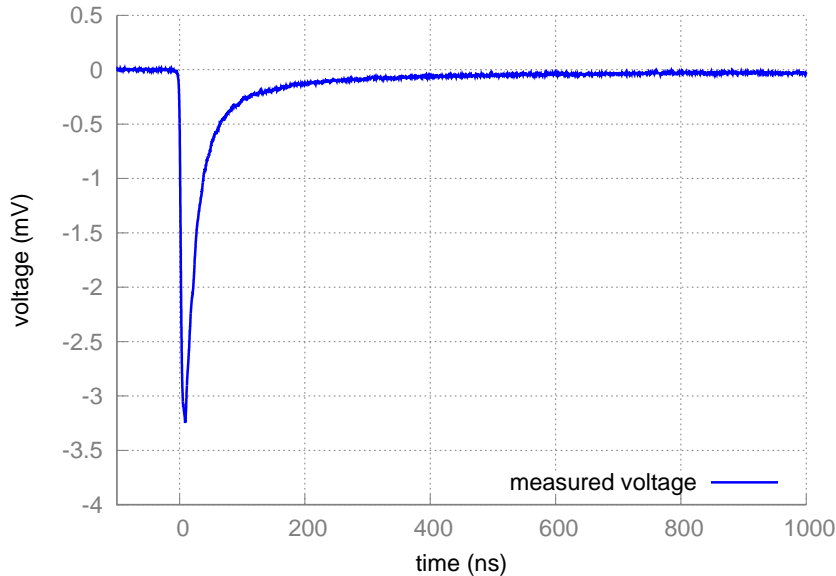


Figure 2.10: The drift chamber voltage signal recorded at the  $50\ \Omega$  oscilloscope input. A distinctive, slow decaying signal tail is visible. The depicted signal is an average over 1000 individual detector pulses.

Ideally we want all ionization electrons to arrive in absolute coincidence to probe the detector's impulse response with a delta-like stimulus. However, there is a certain time spread due to the finite size of the charge cloud and due to diffusion of the drifting electrons in the gas. A model of the non-ideal  $^{55}\text{Fe}$  stimulus is calculated in GARFIELD, a simulation software for gaseous detectors (see chapter 5). Figure 2.11a shows the simulated spatial distribution of the ionization. For better statistics, 100 individual events are superimposed at the same position. We observe a standard deviation of the charge density of circa  $65 - 70\ \mu\text{m}$  in every spatial direction. Consequently the averaged electron arrival time distribution is simulated for a such X-ray conversion occurring at a fixed distance of  $1.25\ \text{mm}$  from the sense wire (half distance between the sense wire and the field wire). The resulting distribution is shown in figure 2.11b. Its shape is Gaussian-like and its standard deviation is  $2.7\ \text{ns}$ . This limits the temporal precision to which the detector response can be measured. It is, however, sufficient for studying the characteristic ion tail and the time development of the charge signal. Of course, other than in this simulation, the photons from the X-ray source produce ionization everywhere in the cell and the broadening due to diffusion varies, depending on the distance to the wire. This example can still be seen as a representative estimation of the diffusion because of the following relations:

- The amount of diffusion increases with the square root of the drift time, and thereby also roughly with the square root of the distance to the sense wire.
- The cross section area of the sensitive detector volume increases with the square of the distance to the sense wire.
- The above effects cancel out, so half way between sense and field wire one should measure the mean diffusion broadening of an uniformly irradiated drift cell (neglecting the corners of the non-cylindrical cell for simplicity).

## 2 Operational aspects of the HADES drift chambers

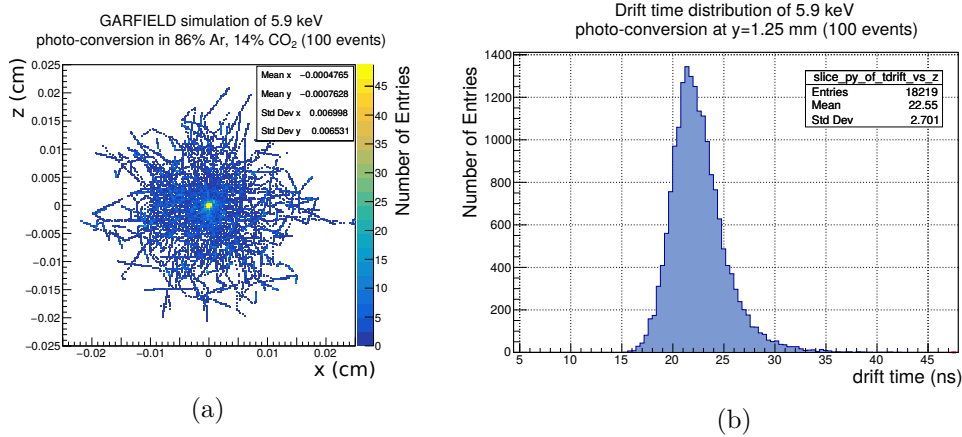


Figure 2.11: (a) 2D projection of the spatial distribution of a  $^{55}\text{Fe}$  ionization (GARFIELD simulation, 100 events), (b) Arrival time distribution of a  $^{55}\text{Fe}$  ionization at a distance of 1.25 mm from the sense wire, simulated with GARFIELD, 100 events. The broadening accounts for both the finite size of the ionization cloud and the diffusion of the drifting electrons.

### 2.4.4 Simple drift cell model

The electronic simulation software LTSPICE [SPI14] was used to model the electrical properties of the drift chamber including the attached cables and their impact on the signal shape. In the following, it is attempted to recreate the measured signal with the fewest possible assumptions about the set-up.

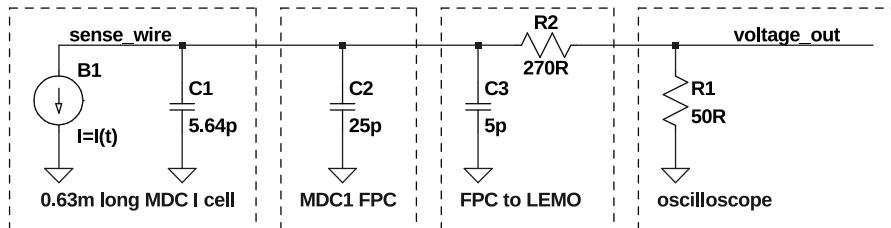


Figure 2.12: Schematic of the simple MDC I drift cell SPICE model. The current source B1 generates a current signal according to the analytical ion current shown in figure 2.7 convoluted with the arrival time distribution of the  $^{55}\text{Fe}$  signal.

The schematic of the simulated circuit is depicted in figure 2.12. The drift cell is modeled as a current source wired in parallel with the calculated capacitance of the cell, according to equation (8). The programmable current source B1 generates a current proportional to the analytically derived ion signal current  $I_{ind}^{ion}(t)$  (equation 33), convoluted with the simulated arrival time distribution of a  $^{55}\text{Fe}$  ionization (figure 2.11b). In addition to the drift cell capacity, also the capacity of the flex print cable and the adapter board which was used in the measurement are taken into account by connecting them in parallel with the detector cell. The oscilloscope is represented as a  $50\ \Omega$  resistor on which we measure the voltage drop and it is connected to the detector via a  $270\ \Omega$  series resistor to match the impedance of the cell, analog to the measurement. The only free parameter of this model is the amplitude of the current source signal, which depends linearly on the yet unknown gas amplification factor.

It is remarkable that by design the capacitance of the detector is dominated by the

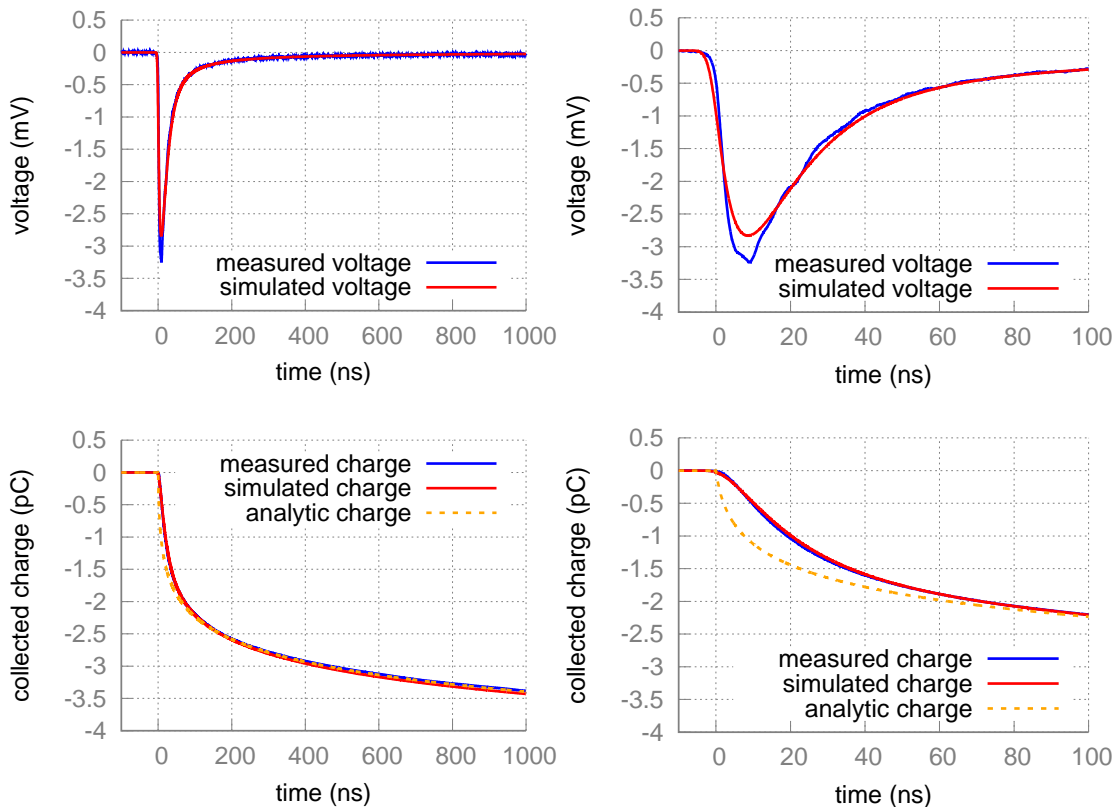


Figure 2.13: Voltage signal and charge signal of the simple drift cell SPICE model in direct comparison to the measured signal, plotted at different time scales. Also shown is the analytic charge signal in accordance with equation (35), which follows a simple logarithm.

attached cables and not by the properties of the drift cell itself. For more details about the capacitances of the different types of flex print cables used in the drift chamber system, see the appendix, section A.1.

Figure 2.13 shows the simulated output signal in direct comparison to the measured chamber signal. From the output voltage we can calculate the collected signal charge by integrating the current that flows through the  $50\ \Omega$  resistor representing the oscilloscope. Both, voltage and charge signals are plotted for two different time scales. The free parameter of the input current amplitude was fixed, so the measured and the simulated charge signal match after  $1\ \mu\text{s}$ . The model predicts a total collected charge of  $5.6\ \text{pC}$  (after  $T^+ = 63\ \mu\text{s}$ ). Assuming the  $^{55}\text{Fe}$  ionization causes an initial charge signal of 218.5 ionizations, this corresponds to a gas amplification gain of

$$G = 1.6 \cdot 10^5.$$

After this charge normalization, the model produces results comparable to the measurement. On the coarse time scale ( $0\ \mu\text{s}$  to  $1\ \mu\text{s}$ ) no significant difference is visible between the measured signal and the simulation. For the charge signal, even the analytic formula for the collected charge (equation (35)) provides a good approximation. For the long term time development of the signal, both the measurement and the output of the SPICE model converge against the analytic solution derived in section 2.3.8. On a finer time scale ( $0\ \text{ns}$  to  $100\ \text{ns}$ ), which is more relevant for the read-out electronics, the difference

between the SPICE model and the measurement are visible more clearly. While the overall pulse shape is reproduced relatively well, it has to be noted that the modeled output voltage slightly underestimates the steepness of measured leading signal edge, and the signal peak is less pronounced. A commonly used measure for the steepness of a signal edge is the rise time  $t_r$ . In most applications it is defined as the time needed for a signal to swing from 10 % to 90 % of its maximum value. Using this definition, the measured signal features a rise time of 4.95 ns and the simulation results in a rise time of 6.68 ns.

Regarding the collected charge on this time scale, it is obvious that the SPICE model is much closer to the measured charge than the analytic solution. Also, because the charge signal is the integral of the voltage ( $\propto$  current) signal, the difference between measurement and simulation is less prominent. The discrepancies between simulation and measurement arise, because in this model the spatial extension of the simulated system and the pulse propagation through the same is neglected. In the case of a propagating pulse, only the local cell capacitance plays a role while in this model the entire cell capacitance is concentrated in a single node. In reality, also signal reflections occur at the junctions between the detector cell, the FPC and the LEMO adapter, i.e. at impedance mismatches, which cannot be described by this model.

#### 2.4.5 Transmission line drift cell model

While the SPICE model in the previous section describes the rough shape of the measured voltage signal quite well, it underestimates the steepness of the rising edge. We now discuss a refined version of the SPICE model, which describes at least the detector cell as an extended one-dimensional object and takes signal propagation delays and reflections into account. As shown in figure 2.14, the detector cell is no longer modeled as a simple capacitor, but instead as a generalized transmission line (e.g. a coaxial cable) with characteristic resistivity, inductance and capacity per unit length and the length of the actual detector cell. It was assumed that the resistivity of the transmission line was dominated by the very thin sense wire. The datasheet [CFW18] of the sense wire material (99.95 % tungsten) specifies a specific resistivity of  $5.49 \mu\Omega\text{cm}$ , which corresponds to a unit length resistivity of

$$R' = 175 \Omega/\text{m} \quad (42)$$

for the given wire radius of  $10 \mu\text{m}$ . For the capacity and inductivity the values were used which were derived earlier in section 2.3.2:

$$C' = 10.1 \text{ pF}/\text{m}, \quad L' = 1.1 \mu\text{H}/\text{m} \quad (43)$$

The simulated transmission line is divided in two smaller lines with half the length. The current source is connected in the middle. This simulates a drift cell which is irradiated exactly in the middle, i.e. with the radioactive source placed at half its length. Apart from that, the SPICE simulation is identical with the simple drift cell model in section 2.4.4.

The simulated voltage and charge signals are shown in figure 2.15. In comparison to the simple model, the transmission line model is better at explaining the rising edge of the signal. The simulated rise time is 4.84 ns, which is closer to the measured rise time of 4.95 ns. The refined model appears to describe the collected charge just as well as the simple model. A remarkable feature of the simulated pulse is the small double peak structure due to the reflection at the open end of the transmission line. This feature is

not observed in the real-life signal. However, unlike the simulation, the physical chamber is not irradiated at a single spot but in a broader region near the center of the respective sense wire, so the reflections are expected to be washed out.

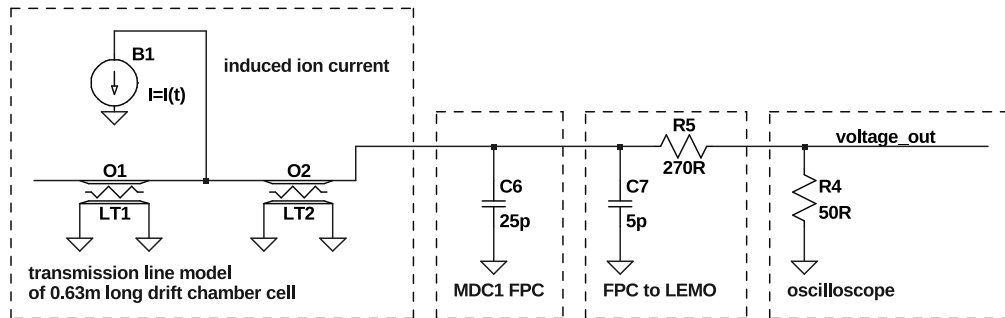


Figure 2.14: Schematic of a SPICE simulation employing lossy transmission lines to model an MDC I drift cell.

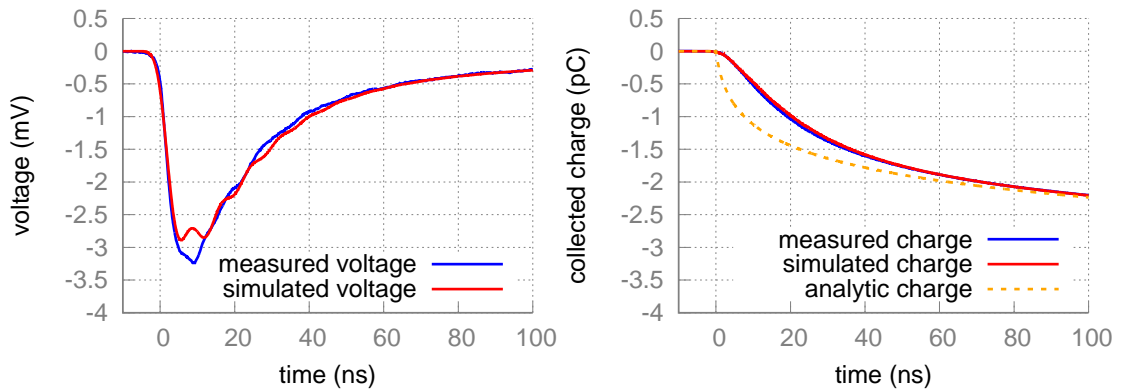


Figure 2.15: Voltage and charge signal at the output of the transmission line drift cell SPICE model compared with the measured drift chamber signal. The analytically derived charge signal is shown for reference as well.

## 2.5 Drift chamber read-out electronics

We discussed the working principle and electrical properties of a HADES MDC drift cell down to the level of modeling the time development of the analog detector output signal. Now we want to deal with the front-end electronics, the part of the signal chain which receives and processes this analog signal, with the purpose to extract meaningful information. As discussed before, there are two observables of interest: On the one hand there is the arrival time of the signal pulse. Given the point in time is known when a charged particle track traverses the drift cell, the time it takes for the signal pulse to arrive is correlated with the radial distance of the particle track to the sense wire. On the other hand there is the total pulse charge which corresponds to the energy loss of the charged particle in the gas volume of the cell. This information helps identifying the particle.

There are different concepts on how to read out such a detector and to extract the above data. Common and absolutely necessary for all concepts is to have a current/charge sensitive pre-amplifier in order to convert the very weak detector current signals into

voltage signals which are decoupled from the detector output node and have a proper voltage swing to be processed by the subsequent electronic components. The input bandwidth needs to be sufficiently high to capture the relevant time frequency domain of the detector signal. One way to extract the desired features is to sample the complete waveform after the amplifier by means of an ADC and to either store the dataset for offline analysis or to process it in real time with a digital signal processing platform. Another way is to employ an analog shaper and a discriminator after the input amplifier. The shaper is an analog circuit which serves multiple purposes:

- Limit the frequency response sharply to the relevant frequency domain to reject unwanted HF noise power (higher order low-pass filtering).
- Establish an approximate linear relation between the peak height of the shaped pulse and the charge content of the input pulse (analog integration).
- Cancel out the ion tail of the drift chamber signal, so the shaper output returns to the baseline quickly and the circuit can process another detector pulse, even though the tail of the first signal is still present.

In fact, the first two functions are achieved with the exact same circuitry.

Subsequently a discriminator compares the shaped signal with a fixed threshold voltage. If the analog signal passes over the threshold, the discriminator generates a logical output signal, which is cleared again, when the analog signal returns below the threshold. The logical signal is then recorded by a time-to-digital converter (TDC) which records the time of the signal's rising and falling edges. The recorded timestamps are then transmitted as digital datasets to the data acquisition (DAQ) system. In the following, the timestamp corresponding to the leading edge of the discriminator output signal will be called  $t1$  and the timestamp of the trailing edge will be called  $t2$ . With the proper threshold setting and calibration, the original pulse charge can, to some extent, be reconstructed from the time-over-threshold (ToT) information, because it is correlated with the shaped pulse height. Obviously the time-over-threshold is calculated as

$$ToT = t2 - t1. \quad (44)$$

A sampling ADC read-out provides full access to the pulse waveform, so arbitrary features (like arrival time and pulse charge) can be extracted independently. Pile-up of multiple pulses can be easily detected and identified as a linear combination of different signals, so there is no need for tail cancellation in hardware. This concept however requires very fast ADCs with a sampling rate of at least 1 GHz, which results in a constant high output data rate and a relatively high power consumption per channel. For a high number of channels, online data processing and feature extraction becomes mandatory.

In comparison with the sampling ADC solution, the shaper/discriminator read-out concept has the advantage, that it is very power-efficient and uses little space especially when integrated circuits can be used. Because feature extraction happens already before the signal enters the digital domain, it drastically reduces the amount of recorded data, which is beneficial when a large number of channels need to be read out in parallel. Despite the resource-efficiency, the shaper/discriminator read-out has the disadvantage, that signal pile-up is undetectable, i.e. only one detector pulse can be processed within the tail-cancellation time frame of the shaper. Furthermore the use of a shaper requires a compromise between arrival time and pulse charge measurement precision. A characteristic parameter of the shaper is the so-called peaking time, which



is defined as the time after which the impulse response function of the shaper reaches its maximum before returning to the baseline again. It can be seen as the characteristic time scale over which the shaper performs an analog integration. The higher the peaking time, the larger the fraction of the detector pulse that contributes to the charge measurement, and the lower the sensitivity of the charge measurement to statistical fluctuations affecting the substructure of the detector pulse. A higher peaking time, however, also decreases the steepness of the leading edge of the shaped signal and results in a lower  $t_1$  measurement precision.

### 2.5.1 Currently used and future MDC electronics

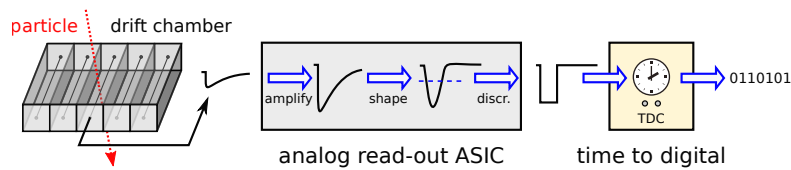


Figure 2.16: Conceptual sketch of the drift chamber read-out chain

In HADES, the shaper/discriminator concept is used, which is depicted in figure 2.16. The front-end electronics are split into two domains, analog and digital, which are handled by two individual ASICs. ASD-8, the currently used analog ASIC, contains a current sensitive amplifier, an analog signal shaping circuit and a discriminator. Each ASD-8 chip has eight individual signal inputs and outputs and can read out eight drift chamber sense wires in parallel. The logical output of the discriminator is fed into a dedicated time to digital converter (TDC) ASIC which has a digital interface connected to the HADES data acquisition (DAQ) system. Because of its resource efficiency, making use of the shaper/discriminator concept is key for the HADES drift chamber system, since a total number of 27000 individual sense wires need to be read out and the placement of the front-end electronics is constrained to the narrow frames of the drift chambers. Furthermore, the power consumption must be low enough, so passive cooling is sufficient for removing the excess heat.

The current front-end electronics consist of two parts: The motherboards and the daughterboards. Each daughterboard hosts two ASD-8 ASICs and is thus able to read out 16 MDC wires. The daughterboard connects to the chamber via four flex print connectors, each connecting four channels. The motherboard hosts the TDC ASICs and a data link to the HADES data acquisition system. Furthermore the motherboard provides mezzanine connectors to be equipped with four or six daughterboards, depending on the board type. Although the current ASD-8 based MDC read-out electronics enabled several successful measurement campaigns with HADES, they repeatedly behaved unstable due to pickup noise and self-oscillation, which makes the MDC system hard to operate. Moreover the TDC ASICs and the subsequent read-out system have the limitation that they can only process one hit per channel per trigger (event). If this one hit is lost by recording a random noise pulse, the respective channel is subsequently blind to particle tracks of the current collision event.

To overcome the limitations it is planned to design a new version of front-end electronics using a multi-hit TDC, i.e. a TDC which can digitize multiple pulses in one trigger cycle. If possible, the analog part of the new front-end should also be able to operate more stable. Furthermore, to operate HADES at the SIS100 accelerator of FAIR, it is contemplated to rebuild the inner MDC layers with additional read-out wire layers at

	ASD-8	PASTTREC
channels	8	8
gain	fixed	programmable: 0.67, 1, 2, 4 mV/fC
peaking time	fixed, 7 ns	programmable: 10, 15, 20, 35 ns
tail cancellation	fixed	programmable: 4 parameters
discriminator threshold	analog input	programmable: 128 steps
discriminator baseline adjustment	-	programmable: 32 steps (per channel)
technology	BJT	CMOS
signal input	differential	single ended
input impedance	120 $\Omega$ [New93]	35 $\Omega$ to 65 $\Omega$ [Prz15]
control interface	-	SPI
power consumption	18 mW/channel	35 mW/channel

Table 2.2: Comparison of ASD-8 and PASTTREC properties and specifications.

additional stereo angles. This update will reduce the number of hits with ambiguous wire combinations and improve tracking at the expected higher track multiplicities. These additional layers then need to be read out with new read-out hardware. Because the original ASD-8 chip is neither available anymore nor can it be produced, an analog read-out chip with similar functionality and properties needed to be found as a replacement. A promising candidate is PASTTREC, an ASIC developed for the read-out of the PANDA straw tube tracking system. In this work PASTTREC was tested for compatibility with MDC, and, wherever possible, in direct comparison with ASD-8. A comparison of the specifications of the two ASICs can be seen in table 2.2. A major difference between the two ASICs is the digital interface (SPI). PASTTREC has a number of programmable settings, such as gain, peaking time, four individual shaper parameters and a common threshold for all channels. Furthermore, each channel has a baseline correction setting, which can be regarded as an individual threshold fine tuning setting. ASD-8, however, has no digital interface. The only free parameter is the threshold setting, which is set via an external analog reference voltage input.

### 2.5.2 Unipolar shaper

As discussed before, the shaper in a drift chamber read-out has the function to limit the frequency response to the relevant frequency domain and to establish an approximate linear relation between the peak height of the shaped pulse and the charge content of the input pulse. Both can be achieved with low-pass filtering, which is also referred to as analog integration. The simplest form of a low-pass filter is an RC circuit. A cascade of multiple identical RC filters is called an unipolar shaper. An example schematic of a

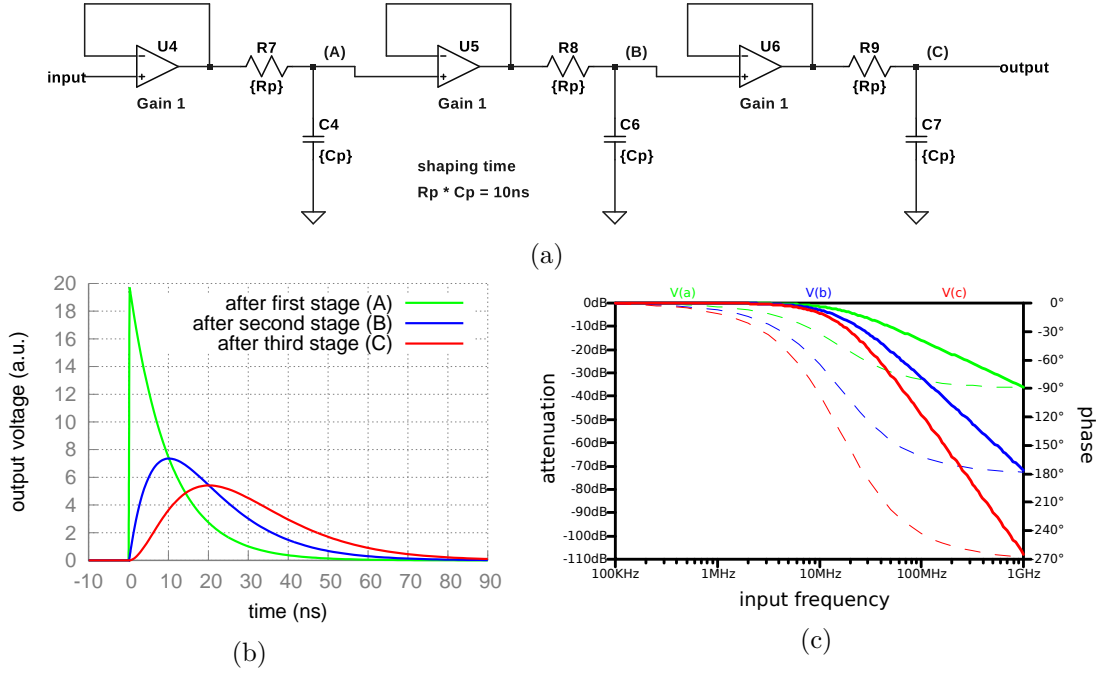


Figure 2.17: Schematic of a three staged unipolar shaper (a) and its simulated impulse response (b) and AC frequency response (c) after each stage. Each shaper stage is an RC filter with time constant  $\tau = 10$  ns.

three staged unipolar shaper is shown in figure 2.17, together with its simulated impulse response and AC frequency response. The RC filters are not directly wired in series but coupled by means of unity gain amplifiers. This way a filter stage is not seen as a load by the previous stage and does not distort its properties. From the impulse response of a single RC stage we can see that it simply adds an exponential tail to each incoming pulse which decays with the characteristic time constant

$$\tau_{sh} = R \cdot C, \quad (45)$$

which we will call the shaping time. In the example, the shaping time is  $\tau_{sh} = 10$  ns. When two or more stages are used, the impulse response function does not peak immediately, but after a certain delay, the so-called peaking time  $t_p$ . It can be shown that for an  $n$ -staged unipolar shaper the peaking time is [BR08]

$$t_p = (n - 1) \cdot \tau_{sh}, \quad (46)$$

which is in excellent agreement with the simulation (figure 2.17b). The peaking time is an important shaper parameter because it determines its effective integration time  $T_I$ . For arbitrary pulses with a duration much shorter than the peaking time, in particular for a delta pulse, the peak amplitude of the shaped pulse is proportional to the total input pulse charge. For pulses with a long tail, especially drift chamber signals, only the charge within a time interval of

$$T_I \approx \frac{t_p}{2} \quad (47)$$

will contribute to the peak amplitude of the shaped pulse [BR08]. This loss of signal charge is called the ballistic deficit. It is quantified as the difference between the measured

## 2 Operational aspects of the HADES drift chambers

charge and the charge that were measured, if the input charge was concentrated in a single delta pulse. As shown in figure 2.17c, the frequency response after every stage is similar, but has a different roll-off slope. From the theory of  $n^{\text{th}}$ -order low-pass filters we know that the roll-off slope is  $-n \cdot 20 \text{ dB/decade}$ . A single RC stage has a cut-off ( $-3 \text{ dB}$ ) frequency of

$$f_c = \frac{1}{2\pi RC} = \frac{1}{2\pi\tau_{sh}}, \quad (48)$$

which is  $15.9 \text{ MHz}$  in the current example. Additional stages slightly lower the cut-off point, however, the order of magnitude of the cut-off frequency is retained. It is obvious that a cascade of multiple RC stages is more effective at suppressing high frequency pickup and white noise from unwanted high frequency bands beyond the relevant frequency domain of the detector signal.

### 2.5.3 Pole-Zero filter and tail cancellation

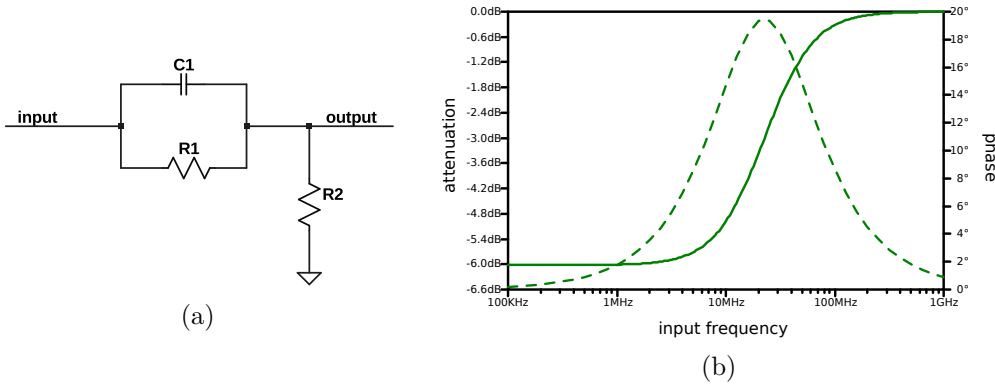


Figure 2.18: Schematic (a) and simulated AC frequency response (b) of a pole-zero filter. Simulation parameters:  $R_1 = R_2$ ,  $R_1 C_1 = \tau_1 = 10 \text{ ns}$ ,  $\tau_2 = 5 \text{ ns}$ .

As mentioned earlier, apart from limiting the bandwidth and integrating the pulse charge, a third function of the shaper is to cancel the long ion tail of the drift chamber signal. Therefore pole-zero filters can be used. The simple circuit, as shown in figure 2.18a, consists of three components: two resistors,  $R_1$  and  $R_2$ , and one capacitor,  $C_1$ . In contrast to an RC circuit, which is characterized by its decay time  $\tau$ , in this circuit, there are two characteristic time constants:

$$\tau_1 = R_1 \cdot C_1 \quad (49)$$

$$\tau_2 = (R_1 || R_2) \cdot C_1 = \frac{1}{1/R_1 + 1/R_2} \cdot C_1 \quad (50)$$

$$\tau_2 < \tau_1. \quad (51)$$

The term pole-zero filter arises from the fact, that such a filter has a pole and a zero at different positions in the complex Laplace  $s$ -plane. The position of the pole and the zero is directly related to  $\tau_1$  and  $\tau_2$ . The circuit has the special property, that it can change, i.e. shorten, the decay slope of an exponential signal tail. Therefore the  $\tau_1$  parameter of the filter must match the decay constant of the input signal. At the output of the filter one can consequently obtain a perfect exponential signal with a decay constant of  $\tau_2$ . This functionality is demonstrated in a SPICE simulation, shown in figure 2.19.

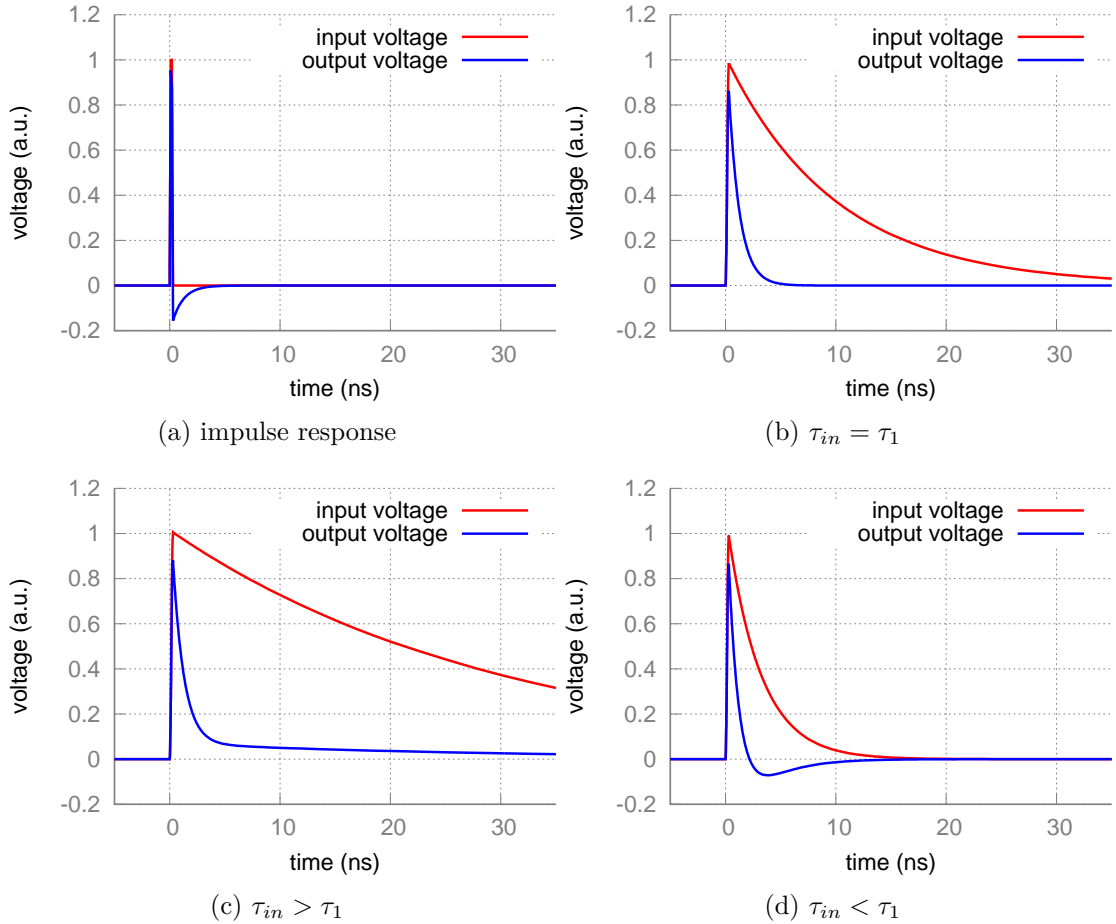


Figure 2.19: Simulated response of a pole-zero filter. The filter has the properties  $\tau_1 = 10$  ns and  $\tau_2 = 1$  ns. The plots show the response to a delta pulse (a) and the response to an exponential with  $\tau = 10$  ns (b),  $\tau = 30$  ns (c),  $\tau = 3$  ns (d).

When the input signal much slower or faster than  $\tau_1$ , the filtered pulse will feature an additional tail or undershoot with the signal's original slope. A pole-zero filter can only cancel exponential tails by substantially shortening them. The tail of the drift chamber signal, however, is of the form

$$I(t) = I_0 \cdot \frac{1}{t + t_0}. \quad (52)$$

Nevertheless, the non-exponential tail can be approximated by a sum of exponentials with different, ever increasing time constants [BR08]:

$$I(t) \approx I_0 \sum_{n=1}^N A_n \cdot e^{-t/\tau_n}, \quad \tau_n < \tau_{n+1} \quad (53)$$

Boie, Hrisoho and Rehak showed, that a drift chamber signal tail can be approximated to a precision of better than 2% by using only three exponential terms [Boi82], and that by using three pole-zero filters, it is possible to cancel out, i.e. shorten, these exponential components. To demonstrate the functionality of such a filter a SPICE simulation was carried out. Figure 2.20 shows the schematic of a cascade of three pole-zero filters, which are coupled by unity gain voltage amplifiers. As an input signal, the simple drift chamber

## 2 Operational aspects of the HADES drift chambers

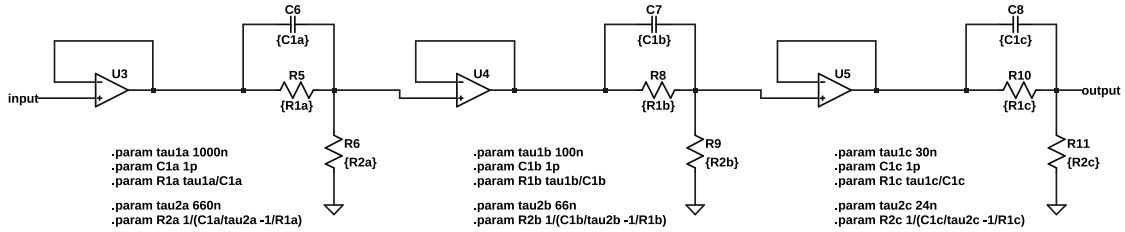


Figure 2.20: Schematic of cascaded pole-zero filters to cancel the ion tail of the drift chamber signal. The chosen filter parameters are:  $\tau_1 = 1 \mu\text{s}$ ,  $\tau_2 = 0.66 \mu\text{s}$  (stage one),  $\tau_1 = 100 \text{ ns}$ ,  $\tau_2 = 66 \text{ ns}$  (stage two),  $\tau_1 = 30 \text{ ns}$ ,  $\tau_2 = 24 \text{ ns}$  (stage three).

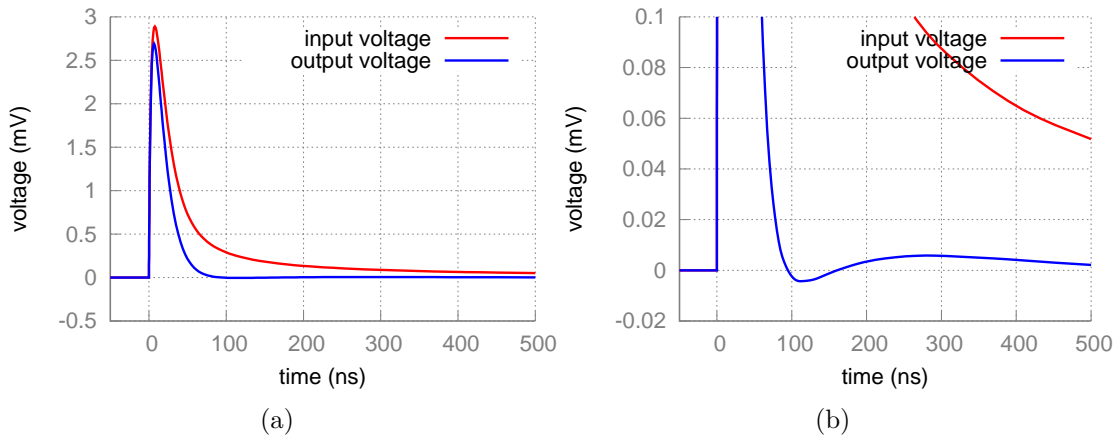


Figure 2.21: Simulated response of a three stage pole-zero filter to a drift chamber pulse. Plot (b) is a magnification of (a) to show the residual of the tail cancellation.

pulse model was used, which was covered in section 2.4.4. For this demonstration, the time constants of the filter were manually adjusted for a good, but not necessarily optimal tail cancellation. The response of the filter is depicted in figure 2.21. When looking at the entire pulse (figure 2.21a), the filter appears to perfectly cancel the tail and the signal returns to the baseline after less than 100 ns. Zooming in (figure 2.21b) reveals the imperfections of the cancellation in form of an undershoot and a residual tail, which do not exceed 0.3 % of the maximum amplitude of the shaped pulse for all times greater than 100 ns.

### 2.5.4 The PASTTREC shaper

In the following we want to discuss the analog signal processing circuitry inside the PASTTREC ASIC. Therefore, based on the technical details described in the Ph.D. thesis of Dominik Przyborowski [Prz15], a simplified equivalent circuit diagram was created, which is depicted in figure 2.22. The schematic does not reflect the actual implementation of the circuitry on a transistor level, but rather the intended ideal functionality of the design, realized with ideal simulated components. In the engineering practice, more complex circuitry is needed to compensate for non-ideal component properties. On this abstract level, the PASTTREC shaper is very similar to the ASD-8 shaper, which uses the exact same sequence of filter stages [New93], even though it is implemented in a completely different semiconductor technology. The equivalent circuit is also used as the basis for a SPICE simulation, so it is possible to study the effects of the individual shaping stages on a simulated drift chamber pulse, which is delivered by the simple

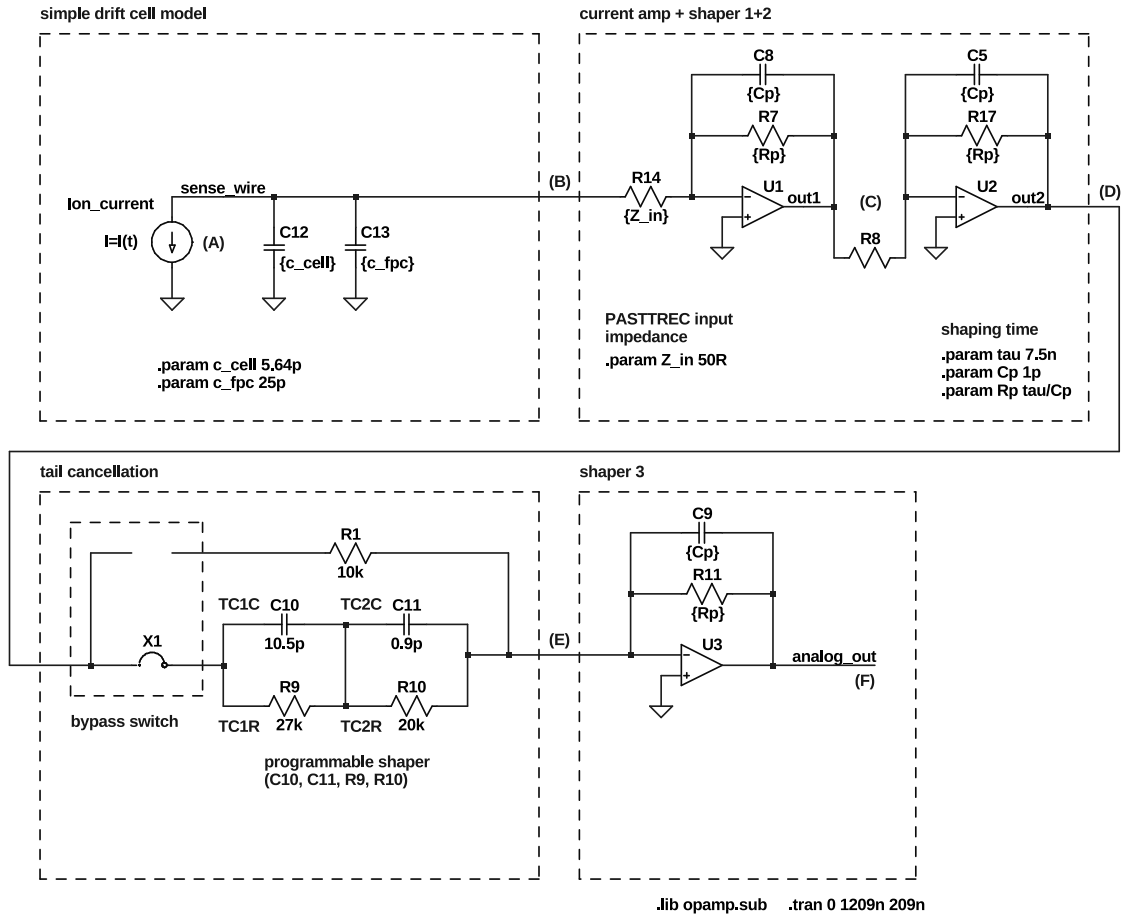


Figure 2.22: Schematic of the simple MDC cell model feeding into a simplified conceptual SPICE model of the PASTTREC shaper.

drift cell pulse SPICE model (section 2.4.4), and which is also included in the depicted schematic.

The first building block of PASTTREC comprises two RC filter stages with equal shaping time  $\tau_{sh}$ , which is equivalent to a two-stage unipolar shaper. In section 2.5.2, the RC filter circuits had to be wired between unity gain operational amplifiers, so one stage is not felt as a load by the previous. In this implementation, however, both, the relevant resistor and capacitor are placed in the return path of an inverting operational amplifier circuit. Apart from inverting the output signal, this circuit has the advantage that the resulting filter stage has a low-impedance current input and a low impedance voltage output, which means that such a filter can directly drive a load. In fact, when an ideal operational amplifier is used, the input as well as the output impedance is exactly zero. Nevertheless, the filter characteristics are exactly identical to the standard RC circuit. The first shaper stage also functions as the input amplifier, which is a current sensitive amplifier. Its finite (non-zero) input impedance is, for simplicity, modeled with an ohmic resistor  $R14 = Z_{in} = 50 \Omega$ <sup>4</sup>. The next building block is the tail cancellation stage. It consists of two programmable resistors TC1R ( $R9$ ) and TC2R ( $R10$ ) and two programmable capacitors TC1C ( $C10$ ) and TC2C ( $C11$ ), which are wired together in a network that can be understood as two non-independent pole-zero filters.

<sup>4</sup>The input impedance of PASTTREC v1 (the first revision after the original prototype) is  $35 \Omega$  to  $65 \Omega$  and depends on the shaping time setting [Prz15].

The functionality is comparable to the tail cancellation filter discussed in section 2.5.3. PASTTREC possesses a programmable switch,  $X1$ , that can be used to bypass the tail cancellation network. The last building block is again an RC filter stage with shaping time  $\tau_{sh}$ . Together with the first two stages it forms a three-stage unipolar shaper with peaking time  $t_p = 2 \cdot \tau_{sh}$ . Just like the the tail-cancellation parameters, the shaping time and the amplification factor are programmable features of the ASIC. In this simulation a shaping time of  $\tau_{sh} = 7.5$  ns was chosen, which corresponds to a peaking time of  $t_p = 15$  ns.

In the ASIC design, a special baseline restoring circuit (BLH - baseline holder) is wired in the feedback path of the last shaping stage to cancel out slow variations in the operating point of the analog circuitry, which are, for example, caused by temperature variations. Because the threshold of the discriminator is defined relative to the baseline, i.e. the idle level of the shaped analog signal, a stable baseline guarantees a reproducible operation of the discriminator and thus, low systematic errors in  $t1$  and  $ToT$  measurement. Furthermore this circuit limits the output amplitude for high input signals. The baseline holder circuit is not included in the depicted diagram and SPICE simulation. Due to its amplitude dependent properties it is a nonlinear circuit, and its influence makes the entire PASTTREC shaper a nonlinear circuit. Therefore the depicted linear equivalent circuit is only an approximation of the PASTTREC shaper response for small signal amplitudes.

The response of the equivalent circuit is simulated with two different input signals. In the first case, we study the response to a single ionization in the detector, i.e. the most pure signal we can imagine for this system. The resulting signals at the individual stages of the signal chain are shown in figure 2.23. Each RC shaper stage decreases the steepness of the pulse's leading edge. Apart from shortening the signal tail, the tail cancellation circuit is affecting the leading edge as well, but increasing the steepness again. The chosen tail-cancellation setting produces an undershoot of 1.2% of the total amplitude after the last stage. In the second case we attempt to simulate a more realistic detector signal, namely the ionization of a minimum ionizing particle traversing a 5 mm long drift cell at a distance of 1.25 mm from the sense wire. Superimposed on the detector current is the theoretical thermal noise (Johnson-Nyquist noise [Joh28]) of the effective RC circuit comprising the capacitance of the detector and the assumed ohmic input impedance of the charge sensitive amplifier. This is achieved by wiring a white noise current source in parallel to  $R14$  with an RMS current amplitude of

$$i_n = \sqrt{\frac{4k_B T \Delta f}{R}}. \quad (54)$$

The noise bandwidth  $\Delta f$  was set to 1 GHz, which is largely exceeding the cut-off frequency of the RC circuit ( $\approx 100$  MHz). The simulated response is depicted in figure 2.24. Here we can see, that the RC shapers not only affect the signal steepness, but also smoothen out noise and blend together the individual ionization spikes.



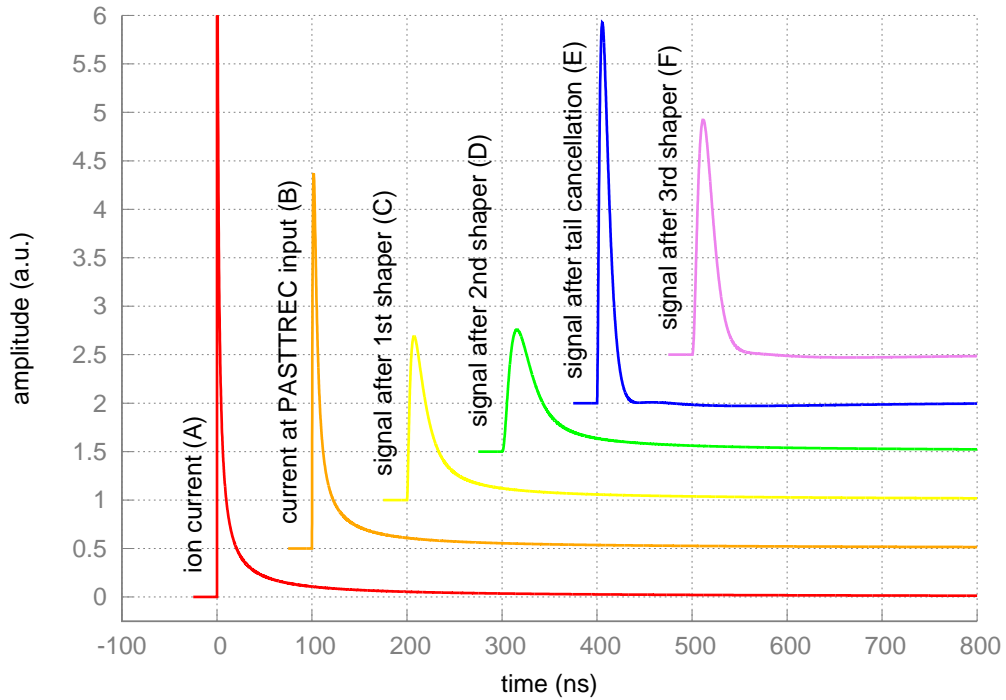


Figure 2.23: Simulated response of the PASTTREC shaper to a single ionization in the detector. Voltage/current signals at the individual stages (A)-(F) in the signal chain are normalized to their integrated signal charge after 100 ns. The curves are shifted relative to each other in time by increments of 100 ns and their baselines by increments of 0.2 a.u. for illustrative reasons.

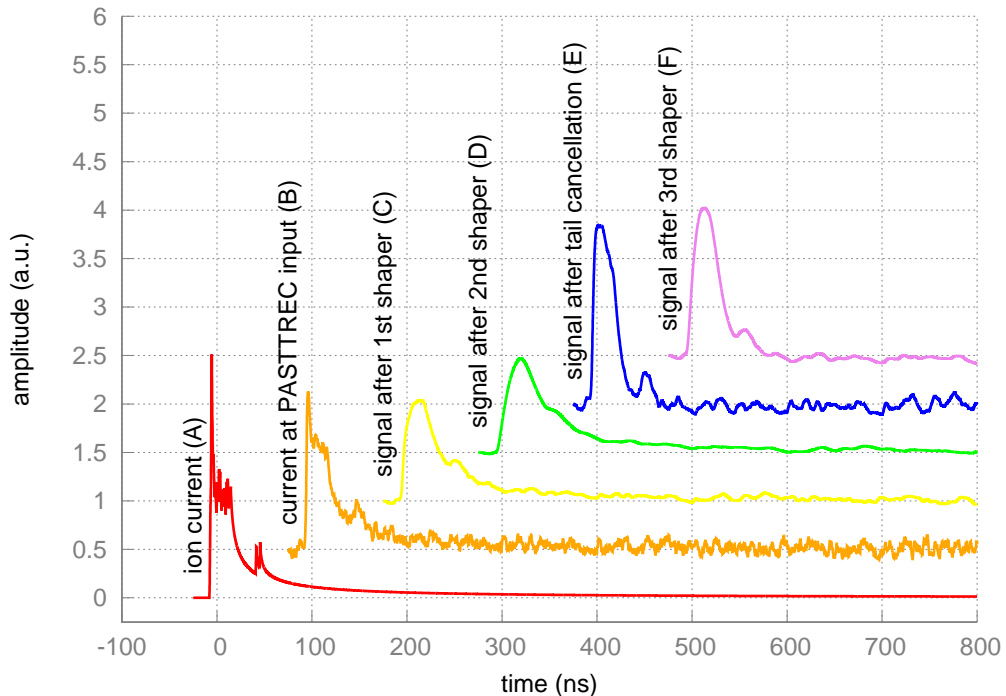


Figure 2.24: Simulated response of the PASTTREC shaper to the signal of a minimum ionizing particle in a 5 mm long drift cell, overlaid with the Johnson-Nyquist (thermal) noise of the effective RC circuit of detector capacitance and ohmic amplifier input impedance.

## 2 Operational aspects of the HADES drift chambers

### 3 Extraction of drift time

#### 3.1 General considerations

In all relevant cases for the operation of a drift chamber as a tracking detector, we want to register the ionization from a charged particle track (although a drift chamber can also detect X-ray photons). By measuring the arrival time of the drifting ionization electrons (relative to a fast reference detector) we attain a quantity that is related to the radial distance of the track from the sense wire. Ideally we want to detect the first arriving electron which originates from ionization along the particle track with the shortest distance to the wire. Because the drift velocity is not uniform over all possible distances, a non-linear calibration function, the so-called space-time relation or  $x(t)$ -relation, is used to convert between drift time and radial distance.

A very important parameter of the joint system comprising drift chamber and read-out electronics is the precision to which the arrival time  $t_1$  of a drift chamber pulse can be measured. The time precision  $\sigma_{t_1}$  is directly proportional to the spatial measurement precision of the drift cell, however, it depends on the steepness of the  $x(t)$ -relation at that respective distance:

$$\sigma_x(t_1) = \frac{dx}{dt}(t_1) \cdot \sigma_{t_1}(t_1) \quad (55)$$

$$\sigma_x(x_1) = \frac{dx}{dt}(t_1) \cdot \sigma_{t_1}(x_1) \quad (56)$$

$$\text{with } x_1 = x(t_1) \quad (57)$$

In the case of a HADES MDC cell, matters are even more complicated. The drift cell cross section has no radial symmetry and further, the cell is not homogeneous in the direction along the sense wire, since the cathode wire plane is oriented at an angle relative to the sense wires. Consequently the drift field geometry reflects these inhomogeneities (see chapter 5). While the field in the inner part of the cell converges against the field of a cylinder capacitor and a simple one dimensional space-time relation is sufficient, the drift time of ionization in the outer parts of the cell is a function of its x, y and z position. In the following, when speaking about the space-time relation of an MDC drift cell, we limit ourselves to tracks perpendicular to the sense/field wire plane. Therefore the first arriving charges will be those deposited within or close to the sense/field wire plane and thus be relatively insensitive to the inhomogeneities due to the crossed cathode wires.

The time measurement uncertainty  $\sigma_{t_1}$  has several individual constituents:

**Stochastic distribution of primary ionization:** The primary ionization is not uniformly distributed along the particle track because the energy deposition in the detector gas is a series of relatively few inelastic scattering events. This leads to a statistical uncertainty and a systematic bias in the drift time, because on average the distance between the closest electrons and the wire is larger than the shortest distance to the track (“impact parameter”). An exemplary situation is shown in figure 3.1a. For obvious geometric reasons, this effect is strongest for tracks passing close to the sense wire. Furthermore the total amount of charge in a signal varies drastically due to the Landau distributed energy loss.

**Electron drift diffusion:** On average, the electron drift trajectories follow the electric field lines in the drift cell. However, transversal diffusion leads to small stochastic detours (see figure 3.1a) and longitudinal diffusion leads to a variation in drift velocity. In sum, diffusion adds a statistical uncertainty in the drift time of each

### 3 Extraction of drift time

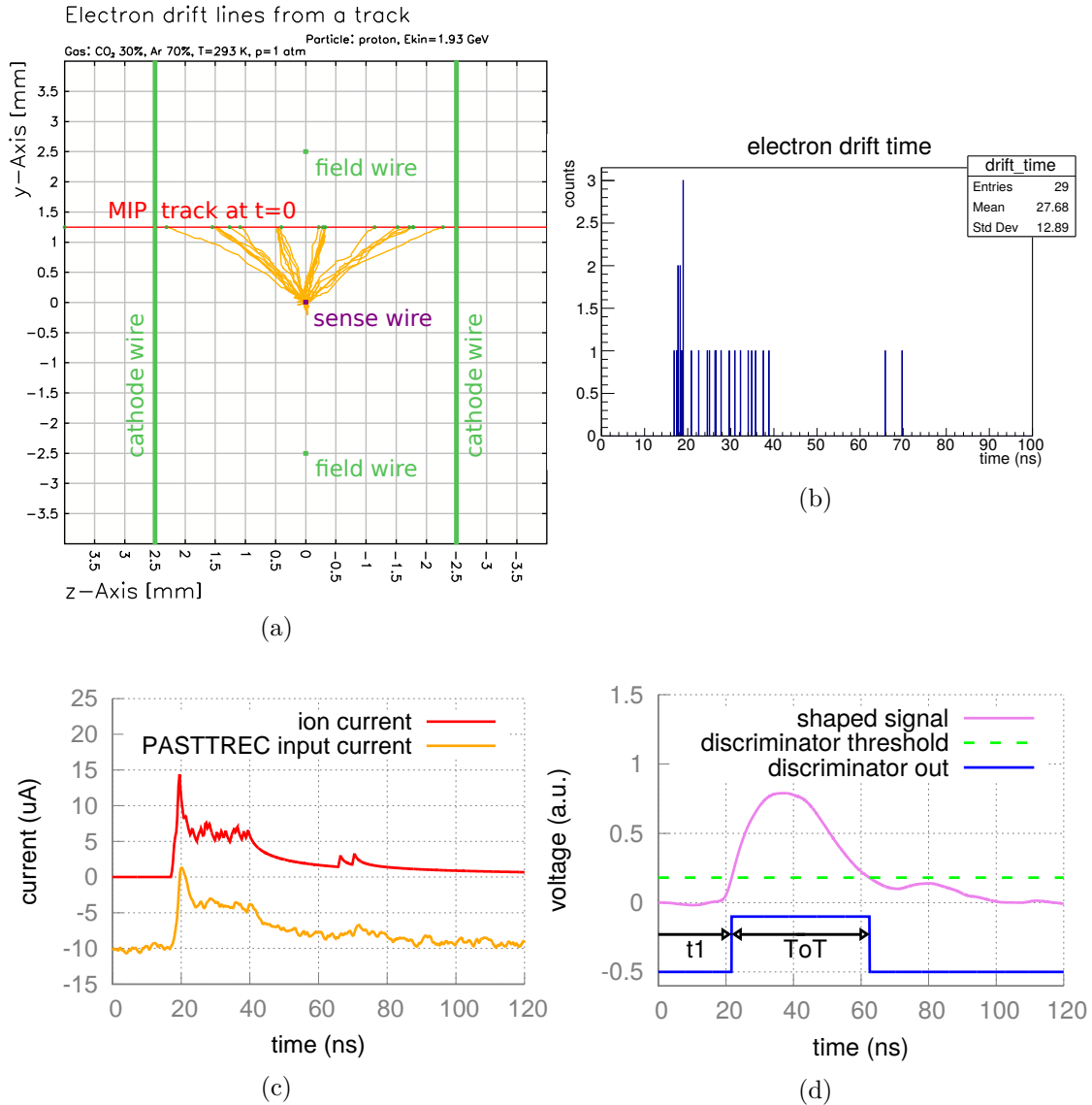


Figure 3.1: (a): Cross section of an MDC I drift cell with ionization from a minimum ionizing particle and electron drift trajectories (GARFIELD simulation). (b): Electron drift/arrival time distribution of the simulated track (c): Ion induced signal current and PASTTREC input current caused by the simulated track using the simple drift cell SPICE model including thermal noise. (d): Signal after PASTTREC shaper (using simplified PASTTREC SPICE simulation) and discriminator output with arbitrary threshold setting.

individual electron, which increases with the square root of the distance of the primary ionization from the sense wire.

**Electronic noise:** Dissipative (resistive) elements in an analog circuit are a source of electronic noise. The so-called thermal noise, which was described by Johnson and Nyquist [Joh28], is a fundamental phenomenon found in all resistors and is a consequence of the Brownian motion of charge carriers in electrical components. In addition to the thermal noise caused by the read-out electronics, also electromagnetic interference picked up from other devices close to the detector contributes to the

electronic noise. Figure 3.1c graphs an estimation of the thermal noise caused by the ohmic input impedance of the signal amplifier (PASTTREC). The residual noise after the shaper leads to a jitter in the  $t_1$  measurement after the discriminator (see figure 3.2a).

**Finite threshold / charge integration:** Ideally, the discriminator threshold is set very closely above the baseline of the shaped signal to be sensitive to the first arriving electron. On short time scales ( $< \text{peaking time}/2$ ), the shaper acts as a pure integrator. Due to the presence of electronic noise, the threshold has to be raised to a certain level so the discriminator is not constantly triggered in absence of a detector pulse. In this case it might require the integrated signal contributions of two or more electron signals to trigger the discriminator. Consequently the system measures the arrival time uncertainties (primary statistics + diffusion) of the  $n^{\text{th}}$  arriving electron, which are generally worse than in the case of the first electron.

**Walk effect:** Because of the finite rise time of the shaped pulses and a finite discriminator threshold, the amplitude of a pulse has a systematic influence on the measurement of  $t_1$ . The higher the amplitude, the faster the threshold is reached, thus high amplitude pulses appear to arrive earlier than otherwise identical pulses with lower amplitude (see figure 3.2b). The walk effect can lead to a spread in  $t_1$  within the same class of tracks because of the Landau fluctuations of the particle's energy loss.

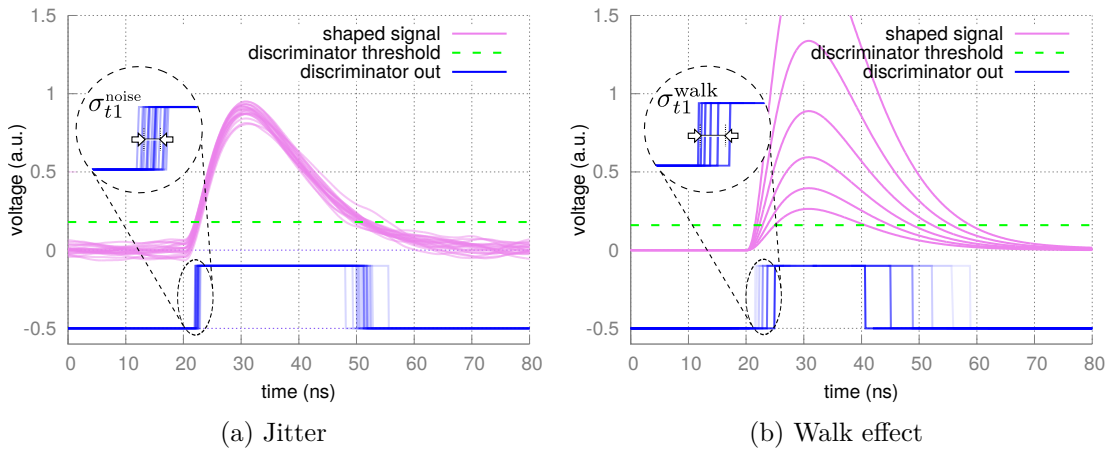


Figure 3.2: (a): Effect of electronic noise on the  $t_1$  measurement precision. The graph shows 20 identical pulses superimposed with noise and processed by an ideal discriminator. (b): Illustration of the walk effect. Varying the amplitude of a pulse systematically affects the measured  $t_1$ .

## 3.2 Time precision tests with cosmic muons

### 3.2.1 Motivation

An important objective of this thesis is to assess the time precision of PASTTREC in combination with MDC, ideally in direct comparison with the old ASD-8 based read-out electronics. It is desirable to characterize the detector system with minimum ionizing particle tracks which represent the most challenging case because they deposit on average the smallest amount of signal charge in the detector. Without a particle accelerator, cosmic muons are a source of close to minimum ionizing particle tracks.

### 3.2.2 Cosmic muons

Cosmic muons are created in the upper atmosphere by cosmic particle radiation. At ground level the average muon energy is  $\approx 4$  GeV and the zenith angle dependent flux can be approximated by [PDG10]

$$j(\vartheta_{xz}) = I_v \cdot \cos^2(\vartheta_{xz}) \quad (58)$$

$$\text{with } I_v = j(0^\circ) \approx 70 \text{ m}^{-2}\text{s}^{-1}\text{sr}^{-1}. \quad (59)$$

For a horizontal plane (detector) this corresponds to an average muon flux of  $\approx 1 \text{ cm}^{-2}\text{min}^{-1}$ . Because a kinetic muon energy of 4 GeV results in a  $\beta\gamma \approx 39$ , the resulting energy loss, as calculated by the Bethe-Bloch formula, is 27% higher than for true minimum ionizing tracks.

### 3.2.3 Self-tracking

In the cosmic muon set-up the “self-tracking” method is used due to the absence of an external tracking device. The applicability of this method is a special feature of the MDC wire arrangement because the two center read-out wire layers are aligned in parallel but shifted by half a cell width. As illustrated in figure 3.3a, in such a geometry a straight perpendicular track creates an ionization signal in two adjacent shifted cells with drift times  $T_a$  and  $T_b$ . Recording a large number of perpendicular tracks and correlating the two drift times provides a means to determine the time precision of the detector. A 2D histogram displaying the sum and the difference of both drift times for 10000 perpendicular tracks is shown in figure 3.3b. Under the hypothetical assumption of an ideal linear space-time relation for the electron drift and neglecting all  $t_1$  measurement errors the sum of both drift times is constant, independent of the exact position of the track. Likewise, the difference of drift times is related to the position of the track:

$$T_a + T_b \approx \text{const} \quad (60)$$

$$T_a - T_b \sim x_{\text{track}} \quad (61)$$

This explains the vertical bar shape in the center of the histogram comprising most of the entries. The diagonal protrusions extending the theoretically expected shape are caused by delayed signals from tracks traversing near the edge of a cell.

Even with a non-linear space-time relation and fluctuations it is possible to select tracks traversing near the center of the overlap region, i.e. with equal distance to both sense wires, by selecting events with  $T_a - T_b$  close to zero. For the selected events the width of the  $T_a + T_b$  distribution reflects the time precision  $\sigma_{t1}$  under the assumption of Gaussian error propagation:

$$\sigma_{t1} = \sigma_{T_a} = \sigma_{T_b} = \sigma_{(T_a+T_b)} \cdot \frac{1}{\sqrt{2}} \quad (62)$$

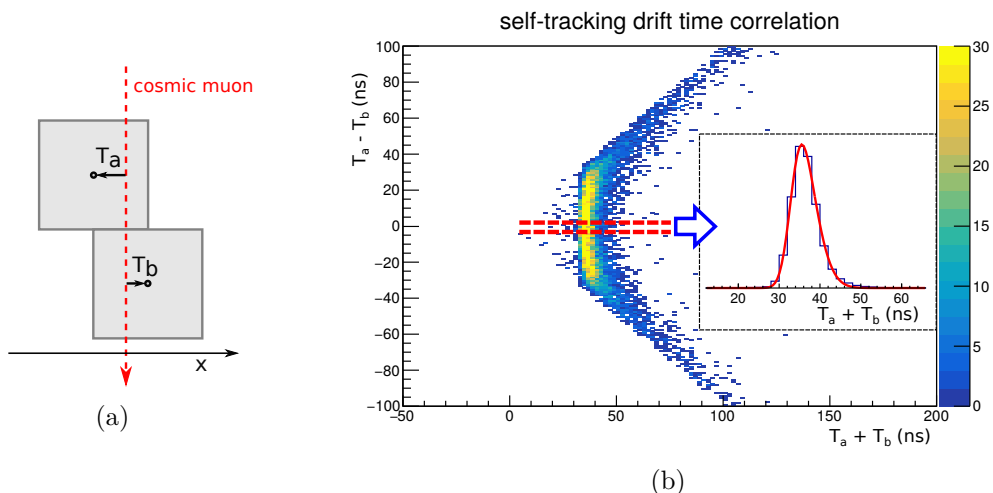


Figure 3.3: Illustration of the self-tracking method. Sketch of a shifted drift cell pair and a vertical track (a), and an exemplary time correlation histogram simulated with GARFIELD (b).

This method can only reliably determine  $\sigma_{t1}$  at a distance of half a cell pitch from the sense wire.

### 3.2.4 Set-up

The cosmic muon self-tracking set-up consists of two stacked MDC chambers with MDC I wire geometry at a distance of 30 cm. A sketch of the set-up is shown in figure 3.4. Two scintillators placed 10 cm below the lower chamber provide trigger and reference time  $t_0$  for impinging muons. The scintillators are placed next to each other to increase coverage. All drift times are measured relative to  $t_0$ . Only the lower chamber is used to assess the time precision via self-tracking. The upper chamber, in combination with the lower one, serves to limit and determine the angle  $\vartheta_{xz}$  of the muon track in the cross section plane (figure 3.4b). For a precision measurement it is necessary to have tracks impinging very close to perpendicular, since  $T_a + T_b$  is very sensitive to the inclination angle of the track.

An earlier version of the self-tracking set-up used a single MDC in combination with a narrow rod-shaped scintillator, parallel to the sense wire orientation, placed at a variable height above the drift chamber. By varying the height of the scintillator it was possible to set the limit of the solid angle of selected cosmic muons. Due to the compromise between small solid angle (measurement precision) and usable muon rate (statistics), this set-up did not yield satisfactory results. In the improved set-up with two stacked drift chambers, the statistics problem is solved by allowing a finite solid angle while measuring the projected inclination angle  $\vartheta_{xz}$  and correcting the recorded data for systematic shifts caused by non-zero  $\vartheta_{xz}$ . In total, four drift chamber layers are read out with eight channels per layer. The sixteen active drift cells in the lower chamber feature fifteen cell combinations which provide a self-tracking geometry. For the benefit of statistics, the data from all self-tracking configurations is combined in the analysis after applying the angle correction. The chamber is operated at a high voltage of 1750 V and a gas mixture of 70% Ar and 30% CO<sub>2</sub>.

### 3 Extraction of drift time

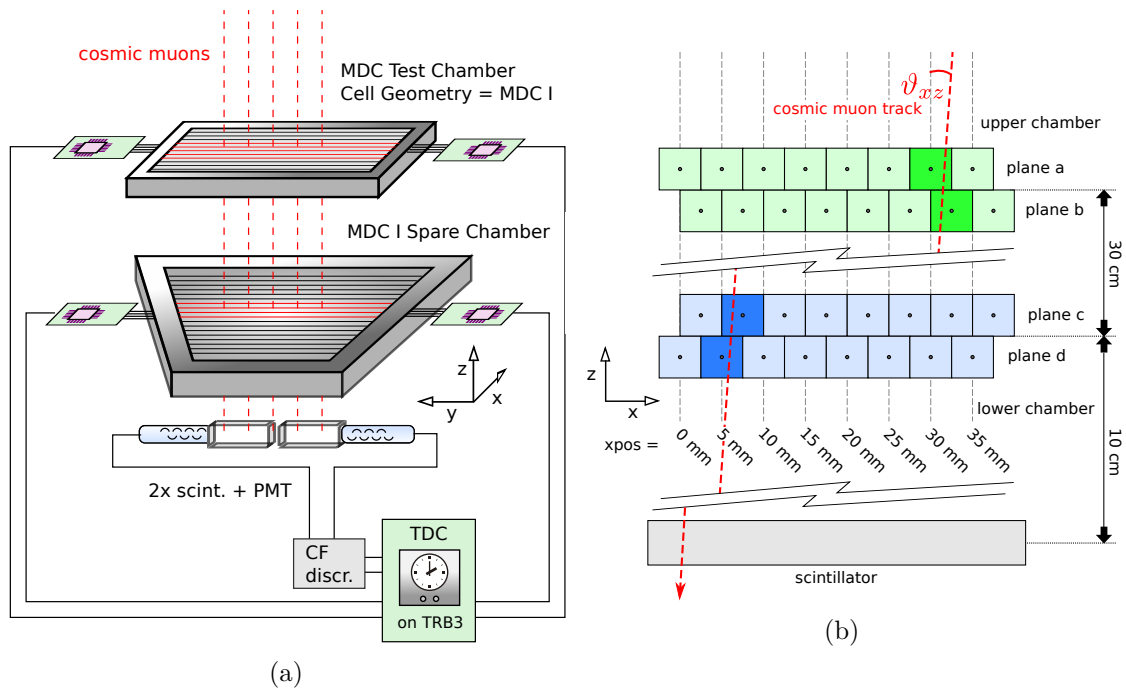


Figure 3.4: Schematic sketch of the cosmic self-tracking set-up (a), and cross section of the active drift cells (b).

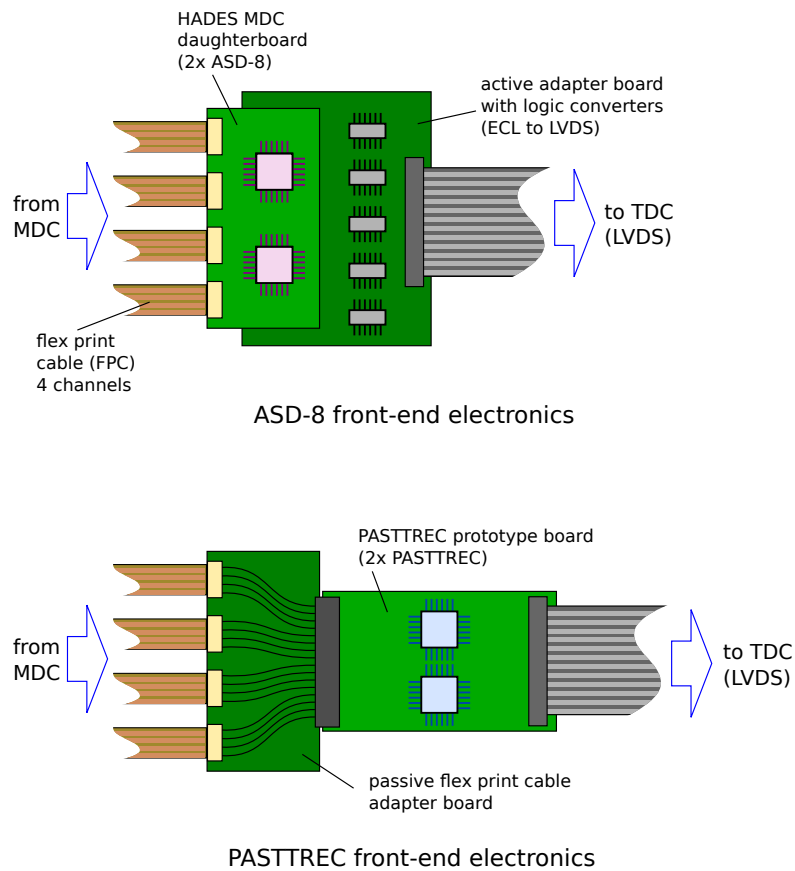


Figure 3.5: Schematic sketch of the front-end electronics used in the set-up.



### 3.2.5 Front-end electronics and signal coupling

To operate the ASD-8 ASIC at an MDC chamber, already existing spare MDC daughterboards are employed. In order to use these with the same TDC and data acquisition system as the PASTTREC ASIC, they are not connected to their proper motherboards, but instead connected to a special adapter board which converts the ECL<sup>5</sup> signals at the ASD-8 outputs to LVDS. For the test operation of PASTTREC a prototype test board is used, which was designed at JU Krakow. PASTTREC already features digital LVDS outputs which are compatible with the inputs of the employed TDC. To connect the prototype board to the MDC flex print cables, a passive adapter board is used, which was designed for this purpose. A sketch of both versions of front-end electronics is shown in figure 3.5. The differential logical output signals of the front-end electronics are fed into a high precision TDC [Ugu13] implemented on a multi purpose FPGA platform (TRBv3 [Mic11]). The recording, pre-processing and online monitoring of the TDC data stream, as well as the calibration of the TDC data, is handled by the Go4 [Ada11] software framework. When properly calibrated, the TDC measurement precision is better than 50 ps and can thus be neglected in comparison to other measurement uncertainties of the set-up.

Concerning the coupling between sense wire and the signal input of the ASICs, as shown in figure 3.6, the schematics differ. The coupling concept implemented on the ASD-8 daughterboard was retained: A voltage divider consisting of two 200  $\Omega$  resistors and an AC coupling capacitor. This circuit effectively increases the input impedance of the ASD-8 analog input from 120  $\Omega$  to 275  $\Omega$  as seen by the sense wire. The coupling between sense wire and PASTTREC was implemented analog to the coupling of the PANDA straw tubes: One 1 M $\Omega$  resistor to keep the sense wire at its working potential (GND for MDC, +HV for straw tube) followed by an AC coupling capacitor. The input impedance of the PASTTREC analog input is seen unaltered by the sense wire. In contrast to PASTTREC, ASD-8 possesses a differential input. In the HADES MDCs, the inverted additional input is connected to a line which runs in parallel with the sensing line on the FPCs and ends either in the chamber frame close to the point where the sense wire is soldered to the FPC (MDC I) or at the point where the FPC reaches the chamber frame (MDC II-IV). The purpose of the pseudo-differential additional line is to cancel out electromagnetic interference which is picked up in equal amounts on the sense wire line and the additional line (i.e. common mode noise).

---

<sup>5</sup>Emitter-coupled logic, a high speed differential digital voltage signal standard

### 3 Extraction of drift time

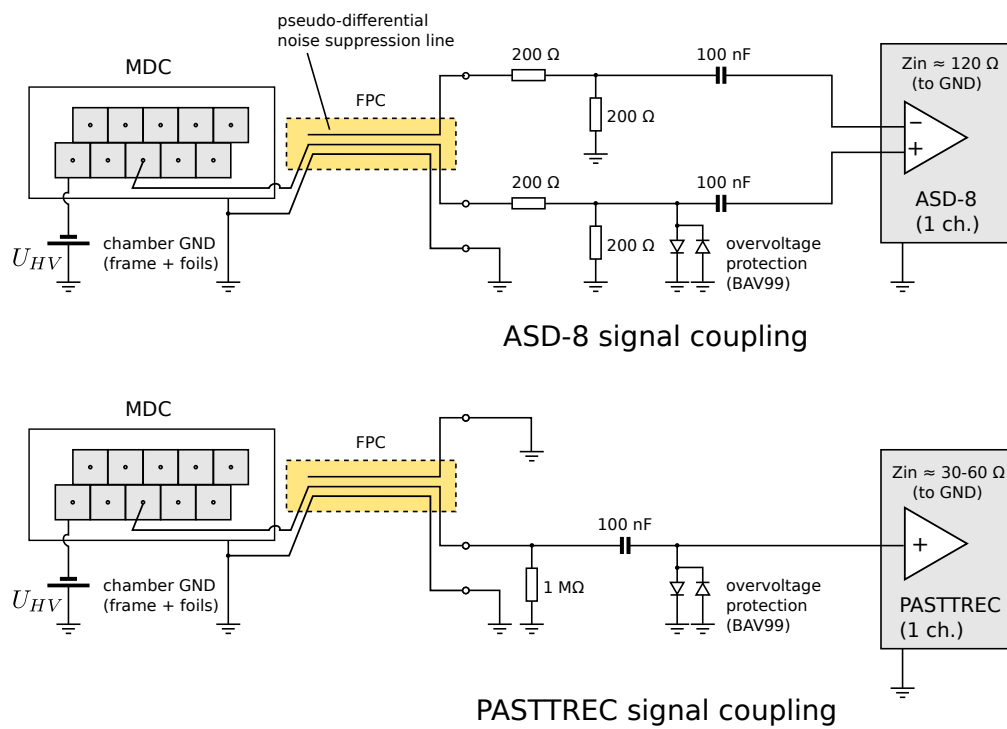


Figure 3.6: Schematics of the coupling of both read-out concepts to the drift chamber.

### 3.2.6 ASIC settings

As discussed in section 2.5.1, ASD-8 and PASTTREC differ in terms of their configurable features (see table 2.2). While ASD-8 only has the discriminator threshold as a free parameter (same for all eight channels), PASTTREC has multitude of digitally programmable settings, such as preamplifier gain, peaking time, threshold and four individual shaper parameters. Even though PASTTREC, too, sets the threshold for all eight channels simultaneously, there is a baseline correction setting for each channel, which can be understood as a threshold fine-tuning. This feature is not explored in the scope of this thesis.

A very low threshold setting should yield the best time precision. On the other hand a low threshold makes the discriminator prone to fire due to electronic or pick-up noise. A high rate of random firing leads to detection efficiency losses, because the actual physical signal might occur within the dead time following a noise signal. In other words, it is desired to find the optimal compromise between a good signal to noise ratio, a good efficiency and a good time precision. For ASD-8 a well performing compromise was found by setting the threshold voltage input to 1.26 V <sup>6</sup>. Since the rate of usable cosmics does not allow for extensive exploration of the large settings space of PASTTREC, some reasonable assumptions and compromises had to be made. Based on the extensive studies of P. Strzempek [Str17], the group at JU Krakow has found optimal PASTTREC settings for the operation of the straw tubes to be used in the future PANDA STT. Even though the PANDA straw tubes are not identical to the MDC cells but merely similar, their preferred ASIC settings were used as a starting point.

During the course of the cosmic muon self-tracking test the PASTTREC ASIC is operated with the following settings:

- gain: 1 mV/fC
- peaking time: 10 ns
- threshold: 10 (20 mV, 2 mV/LSB)
- tail cancellation shaper settings:  
 TC1C=10.5 pF, TC1R=27 k $\Omega$ ,  
 TC2C=0.9 pF, TC2R=20 k $\Omega$

The above shaper settings are identical with the optimal settings for the PANDA straw tubes while operating the ASIC at a gain of 1 mV/fC and a peaking time of 15 ns. However, for this test, the peaking time was lowered to the minimum setting of 10 ns with the aim to achieve the best possible time precision. The chosen settings are not necessarily the optimal settings for reading out an MDC cell with the PASTTREC ASIC. A more detailed investigation of the settings space is performed during the beam test (see section 3.3).

### 3.2.7 Analysis

#### Coincidence matrix

First we verify the consistency of the self-tracking geometry, i.e. that apart from the edges, each cell in the lower chamber overlaps with two other cells in the neighboring

---

<sup>6</sup>For a table comparing the analog threshold voltage to the digital values used in the current HADES DAQ, see section A.5 in the appendix.

### 3 Extraction of drift time

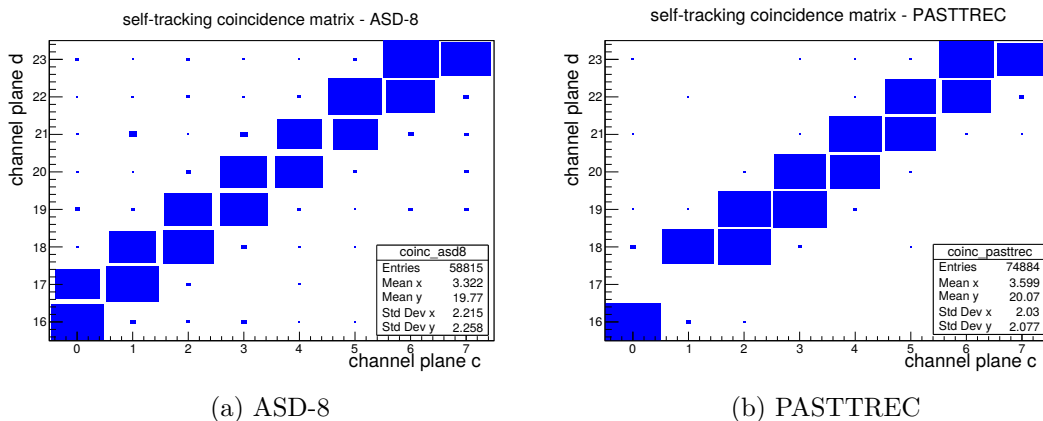


Figure 3.7: Coincidence matrix of the channels in plane c (0-7) versus the channels in plane d (16-23) for ASD-8 (a) and PASTTREC (b). The nomenclature refers to figure 3.4b. The plots demonstrate the coincident firing of geometrically overlapping shifted cells due to vertically impinging muons. Furthermore a dead channel (17) on the PASTTREC board is revealed.

plane. Overlapping cells fire in coincidence when a sufficiently vertical muon impinges on the detector. The coincidence can be graphed in form of a coincidence matrix which is shown in figure 3.7, where the active channels of plane c are correlated with those of plane d. The physically overlapping cell combinations are represented by the diagonal and upper next-to-diagonal elements. Non-overlapping combinations also produce hits due to noise. In comparison to the old ASD-8 front-end electronics, the PASTTREC-based read-out produces less unphysical coincidences due to noise and has a higher firing rate uniformity from channel to channel. The matrix plot also reveals a dead input channel (channel 17) in the PASTTREC board reading out plane d.

#### Inclination angle determination and correction in the x-z plane

The projected incident angle  $\vartheta_{xz}$  (see figure 3.4b) is determined by a crude tracking procedure. Because the space-time relation including the effects of the electronics is not known yet, the drift time information is not used for tracking. In each chamber, a muon track passes through at least two adjacent, shifted cells in neighboring layers. Events with more than one hit per layer are discarded. The measured x coordinate in the respective detector (upper detector:  $x_{ab}$ , lower detector:  $x_{cd}$ ) is then simply the center of the overlap region of the two fired shifted cells. The spatial measurement precision in x direction for a sense/field wire pitch (width of the cell overlap) of  $a = 2.5$  mm is consequently

$$\sigma_x = a \cdot \frac{1}{\sqrt{12}} = 0.72 \text{ mm} \quad (63)$$

under the reasonable assumption, that the track position is uniformly distributed over the cell overlap region. With the chamber distance  $d = 30$  cm, this results in a  $\vartheta_{xz}$  measurement precision of:

$$\vartheta_{xz} = \text{atan} \left( \frac{x_{ab} - x_{cd}}{d} \right) \approx \frac{x_{ab} - x_{cd}}{d} \quad (64)$$

$$\sigma_{\vartheta_{xz}} = \frac{\sqrt{2} \cdot \sigma_x}{d} = 0.19^\circ \quad (65)$$

In the given geometry, the inclination angle can range from  $-6.7^\circ$  to  $6.7^\circ$  and its distribution is triangle shaped, which is shown by a numerical simulation and measurement in figure 3.8. At such small angles, the cosmic muon angle distribution is approximately flat and the projected area of the drift chamber acceptance is approximately constant. Consequently the triangle shape can be understood as the convolution of the two identical box-shaped acceptances, corresponding to the groups of active channels in both drift chambers.

For inclined tracks, the sum of both drift times ( $T_a + T_b$ ) is systematically shifted by  $\Delta(T_a + T_b)$ . The shift only depends on  $\vartheta_{xz}$  and can be geometrically calculated, as shown in figure 3.9. Applying the rules of error propagation we can conclude, that with the given  $\sigma_{\vartheta_{xz}} = 0.19^\circ$ , we can correct the shift in  $(T_a + T_b)$  to a precision of  $\sigma_{(T_a+T_b),\vartheta_{xz}} = 0.27$  ns, assuming a drift velocity of  $v_D = 66 \mu\text{m ns}^{-1}$ , which is derived from a GARFIELD simulation of the drift cell (see section 5.3).

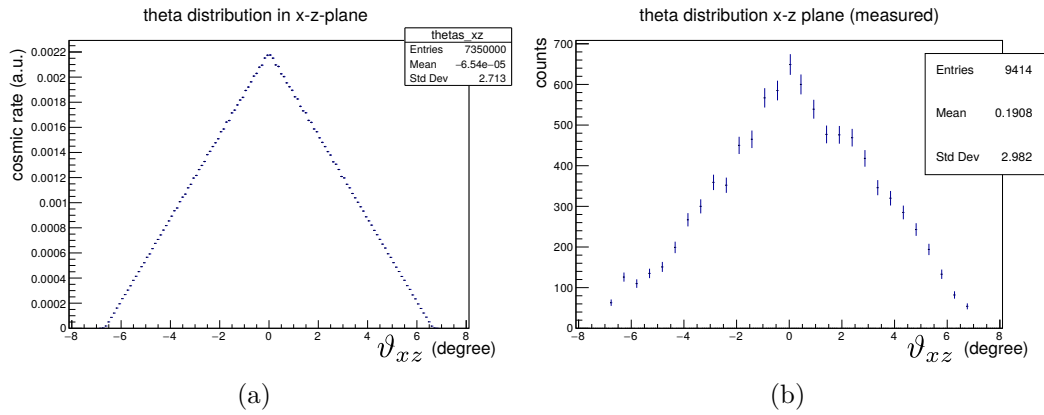


Figure 3.8: Distribution of projected incident angle  $\vartheta_{xz}$  of accepted tracks. (a): Simulation, (b): Measurement.

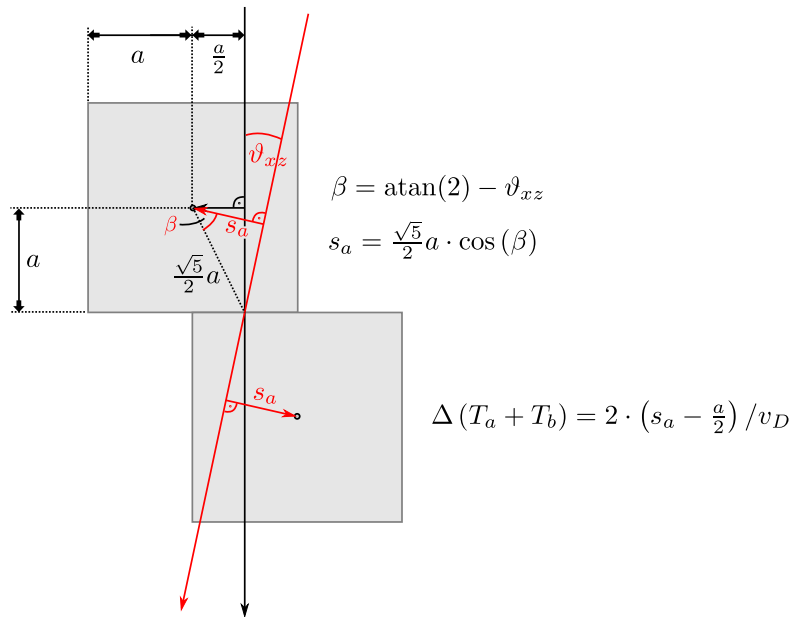


Figure 3.9: Geometric calculation of the shift in  $T_a + T_b$  due to non-perpendicular tracks.

### Self-tracking drift time correlations and feature extraction

Figure 3.10 (a) and figure 3.11 (a) show the recorded self-tracking drift time correlations as a two-dimensional histogram for both versions of read-out electronics. At first sight, the two boomerang-like shapes look very similar, while the PASTTREC data appears to be more diffuse in x direction. As discussed before, the goal is to extract the width of the drift time sum distribution for central tracks. In the following, we select the tracks passing near the center of the cell overlap by demanding the condition  $|T_a - T_b| < 10$  ns. This corresponds to cutting out a central horizontal slice of the boomerang-shape ranging from  $-10$  ns to  $10$  ns. The curvature in this region is relatively small compared to the width of the distribution in horizontal direction. Figure 3.10 (b) and figure 3.11 (b) show the distribution of the drift time sum for the selected slice of the dataset.

Although the distribution resembles a Gaussian, the attempt to fit it with a standard normal distribution reveals a skewness, and thus a slight mismatch in the fit, especially for the PASTTREC data. A better fit function was found in the *skew normal distribution*, which is explained in detail in the appendix, section A.2. In contrast to the standard normal distribution, it has an additional free parameter  $\alpha$  (shape) which determines the skewness  $\gamma_1$  of the distribution:

$$\gamma_1 = \frac{4 - \pi}{2} \frac{(\delta\sqrt{2/\pi})^3}{(1 - 2\delta^2/\pi)^{3/2}} \quad \text{with} \quad \delta = \frac{\alpha}{\sqrt{1 + \alpha^2}} \quad (66)$$

For  $\alpha = 0$  the skewness  $\gamma_1$  is zero and the skew normal distribution is identical with a standard normal distribution. While the central part of the drift time sum peak is excellently described with a skew normal fit, the minor tails to both sides are underrepresented. Therefore the fit model is extended to allow a small Gaussian pedestal, co-aligned with the mean of the skew normal function. The pedestal is regarded as background. The extracted feature is the width, i.e. the analytical standard deviation of the skew normal fit function.

### 3.2 Time precision tests with cosmic muons

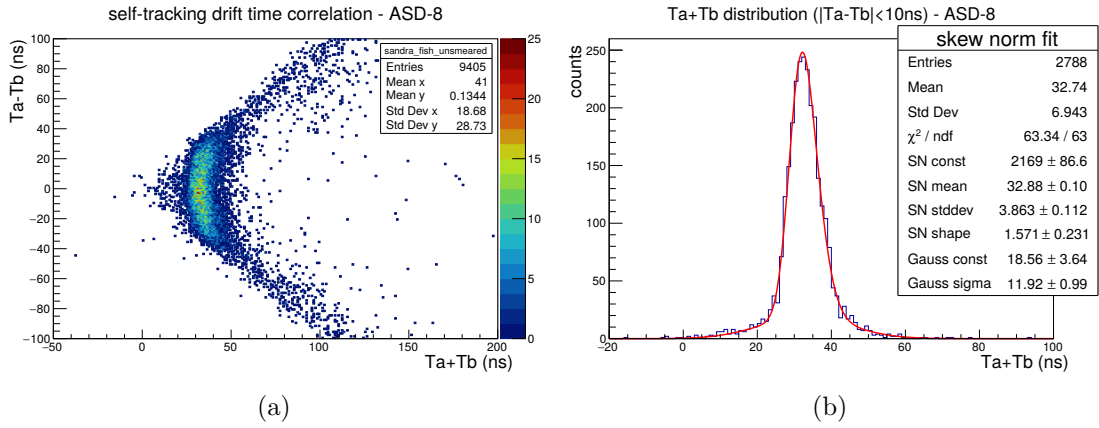


Figure 3.10: Correlation of difference and sum of drift times (a) and drift time sum distribution (b) for  $|T_a - T_b| < 10$  ns recorded with ASD-8. The drift time sum distribution is fitted with a skew normal distribution.

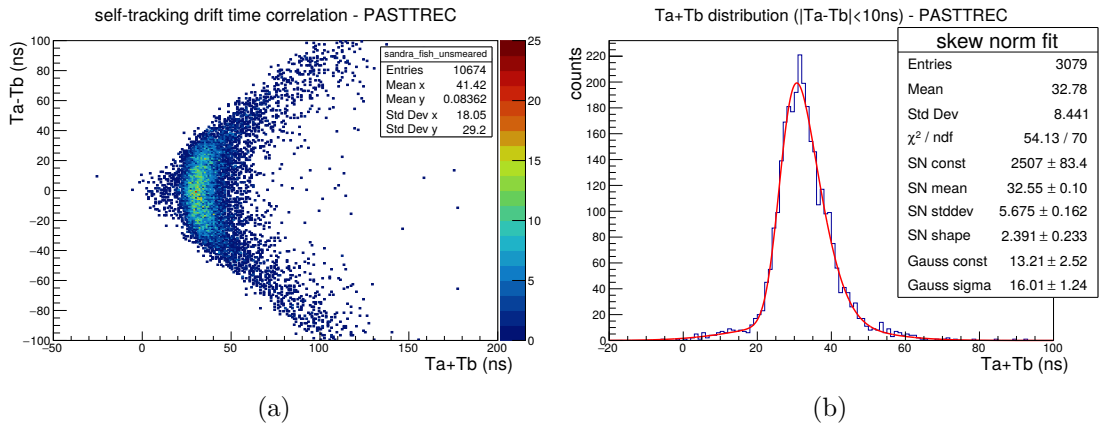


Figure 3.11: Correlation of difference and sum of drift times (a) and drift time sum distribution (b) for  $|T_a - T_b| < 10$  ns recorded with PASTTREC. The drift time sum distribution is fitted with a skew normal distribution.

### 3.2.8 Error analysis

To interpret and compare the measured precisions quantitatively it is important to assess and quantify all contributing factors carefully. This is done in the following.

#### Scintillator precision

The two scintillators deliver a trigger and reference time signal. The uncertainty of this reference signal affects all other drift time measurements. The statistical reference time uncertainty was assessed by placing one scintillator on top of the other and measuring the time difference between signals for cosmic muons traversing both scintillators (see figure 3.12). The distribution of the time difference follows a Gaussian with a width of  $\approx 0.5$  ns. Since this width is the combination of two individual measurements, and both scintillators and attached photomultipliers are identical in type, we can calculate the precision of a single scintillator as

$$\sigma_{t_0, \text{scint}} = 0.5 \text{ ns} \cdot \frac{1}{\sqrt{2}} = 0.35 \text{ ns} \quad (67)$$

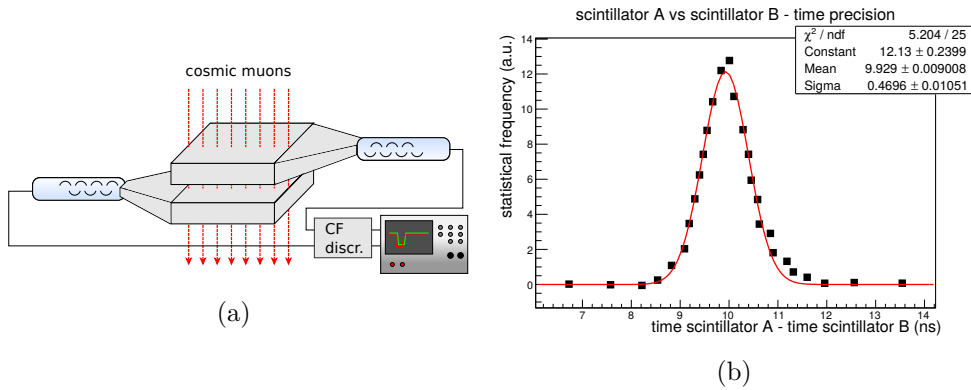


Figure 3.12: Determination of scintillator time precision. (a): Set-up, (b): Distribution of time difference.

#### Effect of inclination angle in y-z plane

While the projection of the inclination angle in the x-z plane  $\vartheta_{xz}$  is very limited and very well known for each measured track, the projection in the y-z plane  $\vartheta_{yz}$  has a wide range due to the geometry of the set-up, i.e. the length of the drift cells and dimensions of the scintillators (see figure 3.13a). The maximum accepted angle is  $45^\circ$ . A numerical simulation was carried out to calculate the distribution of  $\vartheta_{yz}$  on basis of the geometry and the assumption that the cosmic muon rate is proportional to  $\cos^2(\vartheta)$  (figure 3.13b). Based on the angular distribution it is possible to calculate the distribution of the effective track length  $d_{\text{scint}}$  between the lower drift chamber and the scintillator (figure 3.13c). From the standard deviation  $\sigma_{d_{\text{scint}}}$  of the effective track length, we can determine the uncertainty of the drift time measurement due to inclined muon tracks. Assuming muons move at the speed of light, one finds that the additional  $t_0$  uncertainty is

$$\sigma_{t_0, d_{\text{scint}}} = c_0 \cdot \sigma_{d_{\text{scint}}} = 29 \text{ ps} \quad (68)$$

$$\text{with } \sigma_{d_{\text{scint}}} = 8.75 \text{ mm.} \quad (69)$$



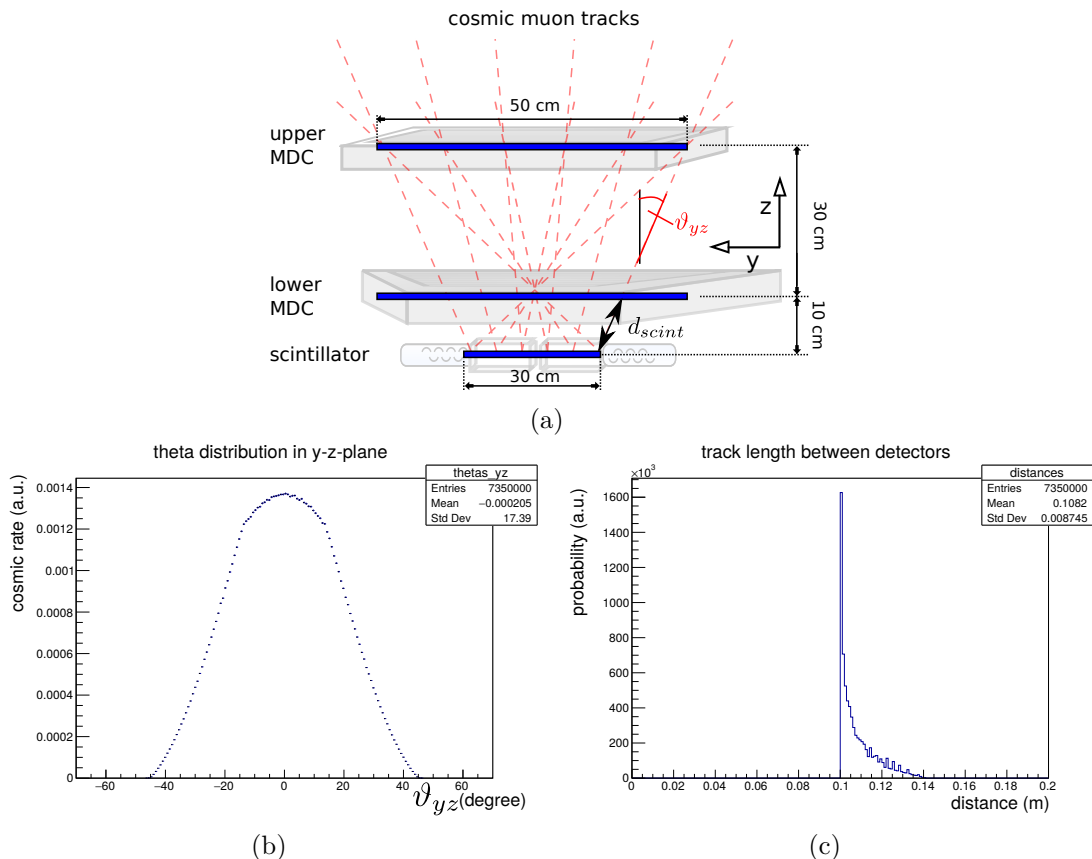


Figure 3.13: (a): Schematic cross section of the set-up in the y-z plane, (b): Simulated track inclination angle distribution in the y-z plane, (c): Simulated distribution of effective distance between scintillator and lower MDC.

This deviation is very small compared to other uncertainties in the system and can be neglected. However, another quantity is distributed in the same way, depending on the incident angle  $\vartheta_{yz}$ : The track length within the drift cell (see figure 3.14). Inclined tracks leave a longer trace of ionization in the cell and thus the charge signal is directly affected. On average, the track length in the cell is 8.2% larger than in the perpendicular case, leading to a 8.2% larger charge signal. In comparison to a perpendicular impinging minimum ionizing particle, the mean ionization of cosmic muons in the given solid angle acceptance is 37.4% higher (+27% due to higher-than-MIP muon energy and +8.2% due to inclination).

### Propagation delays and time offset correction

One obvious source of drift time measurement uncertainty is the propagation delay along the cell, i.e. the time needed for the signal to travel along the sense wire to reach the read-out electronics. In the lower chamber, muons impinge on a length of  $\approx 35$  cm, which corresponds to a delay of 1.2 ns for signals propagating at the speed of light along the sense wire. Fortunately the drift chamber design foresees neighboring zero-degree layers to be read out on opposite sides. This way, when a shifted self-tracking cell pair fires in coincidence from a muon impinging at a certain position, the propagation delays along the two sense wires in both directions add up to a constant. In the self-tracking method only the sum of both drift times ( $T_a + T_b$ ) is analyzed. Consequently a constant shift of

### 3 Extraction of drift time

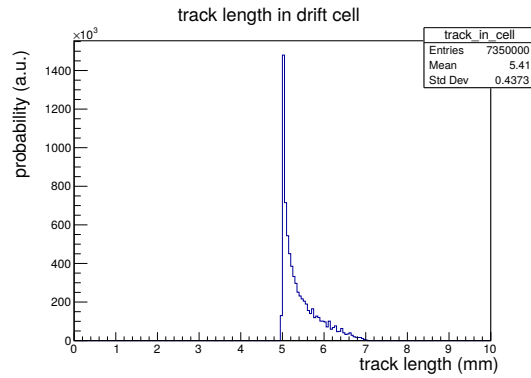


Figure 3.14: Distribution of the track length inside a 5 mm × 5 mm drift cell, which is relevant for the energy loss and the charge signal in the detector.

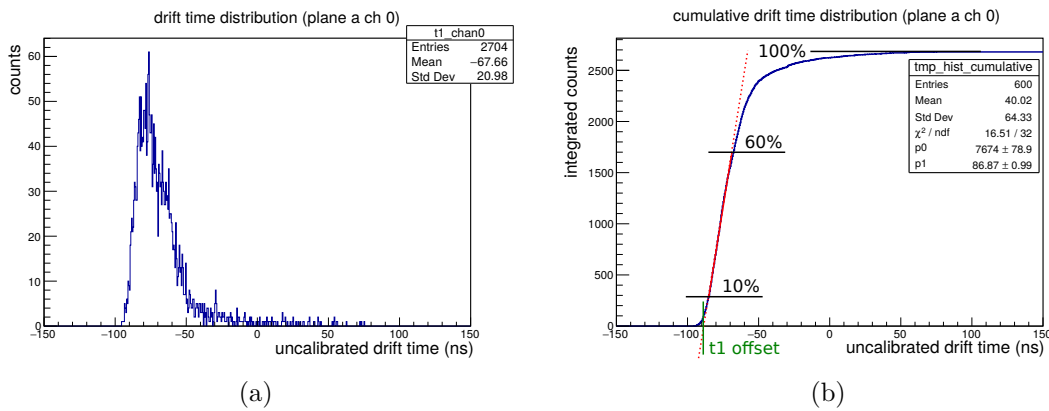


Figure 3.15: Drift time delay correction procedure. (a):  $t_1$  distribution (uncorrected) of single drift cell vs scintillator, (b): cumulative distribution of (a) with linear fit between 10% and 60% of the total integral. The offset for the  $t_1$  correction is calculated as the intersection of the linear fit function with the x axis. The negative raw time values are due to long cables and delays in the constant fraction discriminator for the scintillator signal.

the sum does not affect the width of the distribution.

Apart from the delay along the sense wire, there is signal delay on every kind of signal carrying cabling, analog and digital, between the drift chambers, the scintillators and the TDC. Also processing/switching delays in the analog and digital electronics play a role. The net sum of all delays for each channel are assessed and removed by a correction procedure:

- For each active drift cell a histogram is generated and filled with the arrival time difference between drift cell (detector) and scintillator (reference) signal pulses. This is the raw/uncorrected drift time distribution. One example is shown in figure 3.15a.
- The histogram is integrated, so it holds the cumulative distribution. Each channel displays an approximately linear rise in the cumulative distribution between 10% and 60% of the total integral. This region is fitted with a linear function. An example is shown in figure 3.15b.

- The desired  $t1$  offset for the correction is calculated as the intersection of the linear fit function with the x axis.
- All drift time data recorded by this channel are corrected by subtracting the above calculated offset. The procedure is performed for each drift cell individually.
- Two individual scintillators are used for providing reference time and both can trigger the data acquisition. Recorded datasets triggered by different scintillators are kept separate and are calibrated independently.

The idea is to attain a correction offset, so that when subtracted, the earliest possible arriving signals (i.e. by ionization traces in direct vicinity of the sense wire) have a corrected measured  $t1$  of 0 ns. Calculating the offset by the first (earliest) entries in the raw drift time distribution has the disadvantage, that even a single noise event can disturb the correction if it occurs earlier than the first real signal. The above procedure is more robust, since it exploits a feature of the distribution, which is invariant for small fractions of noise hits<sup>7</sup>.

The correction procedure produces two sets of correction offsets: one set of all drift cell offsets for each scintillator. The error of this correction is estimated by comparing the differences between the two sets of correction offsets. The spread of the correction offset difference between both datasets is depicted in figure 3.16. The standard deviation over all active channels is the same for both ASICs, within one percent. We conclude, that the  $t1$  offset correction procedure can be performed to a precision of

$$\sigma_{t1,offset} = 0.19 \text{ ns} \quad (70)$$

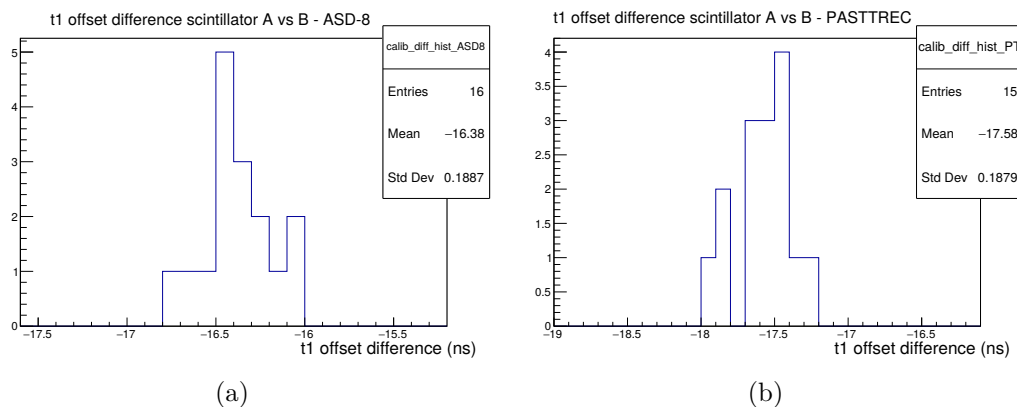


Figure 3.16: Estimation of the  $t1$  offset correction precision: Difference between  $t1$  offset parameters between scintillator A and scintillator B. Recorded with ASD-8 (a) and PASTTREC (b). The statistics range over the 16 (15, one dead channel) active channels in the lower chamber.

<sup>7</sup>The method is inspired by a similar offset calibration technique for the HADES drift chambers [Mar05].

### Combined statistical error

Combining all discussed errors, for a  $t1$  measurement of a single drift cell we have to assume a set-up related statistical error of

$$\sigma_{t1, \text{ set-up}} = \sqrt{(\sigma_{t0, \text{ scint}})^2 + (\sigma_{t0, d_{\text{scint}}})^2 + (\sigma_{t1, \text{ offset}})^2} \quad (71)$$

$$= 0.40 \text{ ns.} \quad (72)$$

When calculating the statistical error of the sum of two drift times ( $T_a + T_b$ ) in a self-tracking cell pair, we have to keep in mind, that the uncertainties concerning the  $t_0$  measurement by the scintillator are not statistically independent in the same event and thus add up. A similar argument holds for the  $t1$  offset correction error: In a self-tracking cell pair, the active channels are not combined randomly, instead the cells are always correlated with the same neighbors. It is therefore safer to assume, that the  $t1$  offset errors add up every time.

$$\sigma_{(T_a+T_b), \text{ set-up}} \quad (73)$$

$$= \sqrt{(\sigma_{(T_a+T_b), \vartheta_{xz}})^2 + (2 \cdot \sigma_{t0, \text{ scint}})^2 + (2 \cdot \sigma_{t0, d_{\text{scint}}})^2 + (2 \cdot \sigma_{t1, \text{ offset}})^2} \quad (74)$$

$$= 0.84 \text{ ns} \quad (75)$$

### Systematic errors and fit error

The width of a distribution represents a mean difference between many measurements underlying the same systematic errors. Because in the cosmic muon self-tracking set-up we are interested in a measurement precision which corresponds to a width of a distribution, many static systematic errors cancel out. However, since the set-up has to run approximately one week to acquire sufficient statistics for one ASIC, there is the possibility for systematic drifts in the system, e.g. slowly changing discriminator thresholds for the scintillators or varying electromagnetic interference levels in the drift chamber sense wires. Because of the sparse statistics due to the limited cosmic rate, no systematic error analysis concerning slow time dependent systematic shifts has been conducted.

Another source of systematic error is the analysis. Fitting the measured and corrected ( $T_a + T_b$ ) distribution with a specific fit function, in this case a skew normal distribution, introduces an unknown systematic error. We attempt an estimation of the systematic fit error by comparing the results of the fit with the parameters of a pure Gaussian fit.

	ASD-8	PASTTREC
StdDev skew normal fit	$(3.863 \pm 0.112) \text{ ns}$	$(5.675 \pm 0.162) \text{ ns}$
StdDev Gaussian fit	$(4.492 \pm 0.088) \text{ ns}$	$(6.216 \pm 0.115) \text{ ns}$
Difference/systematic error	$0.629 \text{ ns (16\%)}$	$0.541 \text{ ns (10\%)}$

### 3.2.9 Results

In the end, we want to assess the measurement precision of the MDC including electronics. Therefore we want to separate the intrinsic uncertainties of the detector from the additional uncertainties caused by the cosmic muon self-tracking set-up:

$$\sigma_{(T_a+T_b), \text{ fit}} = \sqrt{\left(\sigma_{(T_a+T_b), \text{ MDC}}\right)^2 + \left(\sigma_{(T_a+T_b), \text{ set-up}}\right)^2} \quad (76)$$

$$\sigma_{t1} = \sigma_{T_a, \text{ MDC}} = \frac{1}{\sqrt{2}} \cdot \sigma_{(T_a+T_b), \text{ MDC}} \quad (77)$$

$$= \frac{1}{\sqrt{2}} \cdot \sqrt{\left(\sigma_{(T_a+T_b), \text{ fit}}\right)^2 - \left(\sigma_{(T_a+T_b), \text{ set-up}}\right)^2} \quad (78)$$

As a systematic error for the resulting time precisions we assume an uncertainty of 16% (ASD-8) and 10% (PASTTREC), which dominates the numerical statistical fit errors.

	ASD-8	PASTTREC
$\sigma_{(T_a+T_b), \text{ fit}}$	$(3.86 \pm 0.61) \text{ ns}$	$(5.68 \pm 0.57) \text{ ns}$
$\sigma_{(T_a+T_b), \text{ MDC}}$	$(3.77 \pm 0.60) \text{ ns}$	$(5.61 \pm 0.56) \text{ ns}$
$\sigma_{t1}$	$(2.67 \pm 0.43) \text{ ns}$	$(3.97 \pm 0.40) \text{ ns}$

### 3.3 Time precision tests with proton beam

#### 3.3.1 Motivation

The cosmic muon self-tracking set-up was useful for the commissioning of a stable data acquisition system for the read-out and comparison of both analog ASICs. However the downside is, that the performance is measured with particles producing on average an estimated amount of 37% more ionization than minimum ionizing particles and the time precision was only determined at a position at half the distance between sense and field wire. Furthermore, due to the low rate of triggered cosmics (circa 1 week for one dataset) not all relevant combinations of ASIC settings can be investigated systematically.

To overcome these limitations, a small rectangular shaped test chamber with MDC I wire geometry and was provided by GSI and operated at the COSY accelerator, which provides a beam of minimum ionizing protons. With the beam test set-up it is possible to directly measure the space-time relation and the drift time measurement precision at any distance from the sense wire with sufficient statistics.

#### 3.3.2 Set-up

##### Beam

The beam is a pure proton beam with a kinetic energy and momentum of

$$E_{\text{kin,beam}} = 1.93 \text{ GeV} \quad (79)$$

$$p_{\text{beam}} = 2.70 \text{ GeV}/c. \quad (80)$$

At this energy protons are minimum ionizing particles as they possess a relativistic velocity of

$$\beta\gamma = \frac{p_{\text{beam}}}{m_p \cdot c_0} = 2.889. \quad (81)$$

The particle velocity is

$$v_p = 2.833 \times 10^8 \text{ m/s}. \quad (82)$$

##### Main detectors

A simplified sketch of the beam test set-up is depicted in figure 3.17. The MDC test chamber is irradiated with a few centimeters wide<sup>8</sup> minimum ionizing proton beam, while 5 cm behind it a segmented diamond detector is placed, providing data acquisition trigger and reference time  $t_0$ , as well as the reference track position, assuming parallel tracks. The drift chamber is a prototype chamber with MDC I wire geometry and a wire length of 50 cm. The diamond detector features two adjacent electrodes which measure  $2.1 \text{ mm} \times 2.1 \text{ mm}$  each and are separated by a  $90 \mu\text{m}$  wide gap.

In the case both diamond segments fire in coincidence, we assume that a beam particle hit gap between the electrodes. This way it is possible to select tracks within a circa  $90 \mu\text{m}$  thin slice of a relatively wide beam. The diamond gap is oriented in parallel with the sense wires of the drift chamber and the diamond detector is attached to a precisely movable gantry with remote controlled stepper motors. By moving the diamond detector parallel to the sense wire plane it is possible to trigger on tracks at any position within a drift cell. This facilitates the measurement of the drift time  $t_1$  and the drift time precision  $\sigma_{t_1}$  at specific distances from the sense wire.

<sup>8</sup>For an estimation of the beam profile, see figure 3.20b.

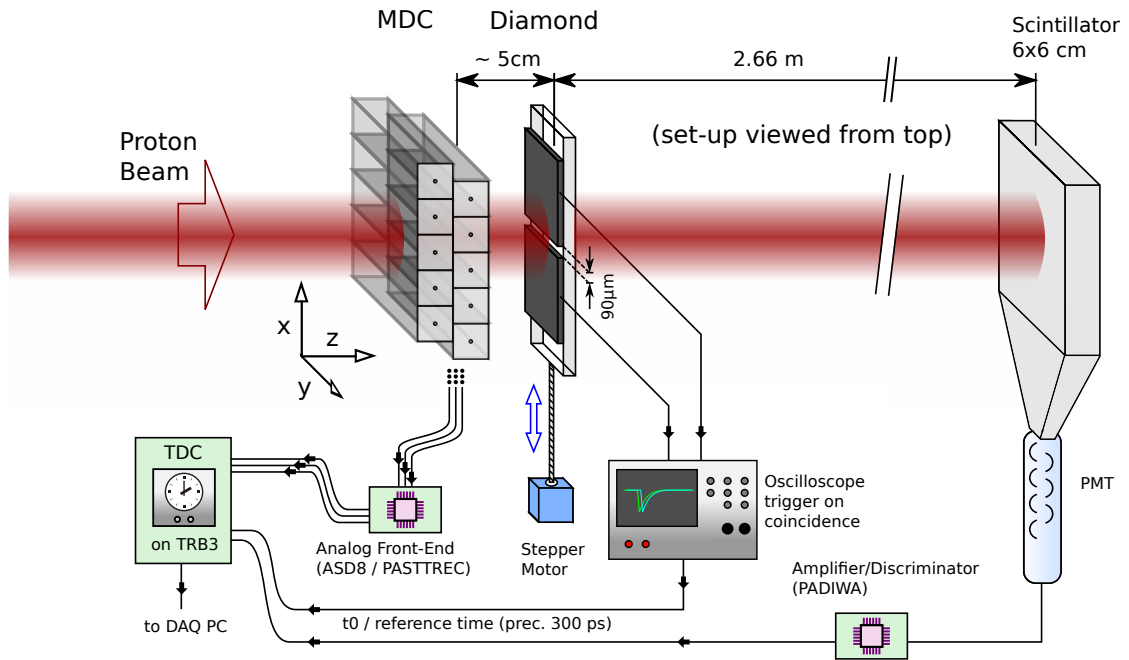


Figure 3.17: Schematic sketch of the beam test set-up (not to scale).

### Auxiliary detector

At a distance of 2.66 m behind the diamond detector a 6 cm × 6 cm scintillator is placed on axis with the beam. The signal from this detector is used as an additional trigger condition to clean up the track selection. Requiring a narrow coincidence between diamond and scintillator time measurements (plus a veto on coincidences outside of the desired window) discards events in which pile-up occurred.

### Electronics

Just like in the cosmic muon self-tracking set-up a precision FPGA-based TDC [Ugu13] is used to measure and digitize times. By configuration, the first leading edge registered by a TDC channel in a recorded event defines the measured  $t_1$ . Alternatively, the TDC can be operated in multi-hit mode, then several hits can be recorded and analyzed in the same trigger window. The front-end electronics are connected the same way as in the cosmic muon tracking set-up (see section 3.2.5). The analog signals from the two neighboring diamond electrodes are read out with an oscilloscope, which is configured to generate a trigger pulse when both electrodes fire in coincidence. The coincidence window is determined by the time of the diamond signals above the trigger threshold which can be estimated with  $\approx 10$  ns (depending on pulse height). This is due to the fact, that the oscilloscope implements a logical AND of both discriminated diamond signals. The scintillator signal is discriminated by a PADIWA board [Nei13] which provides a linear amplifier and a discriminator with remote programmable threshold.

### 3.3.3 Analysis

#### Time structure of the beam and random correlations

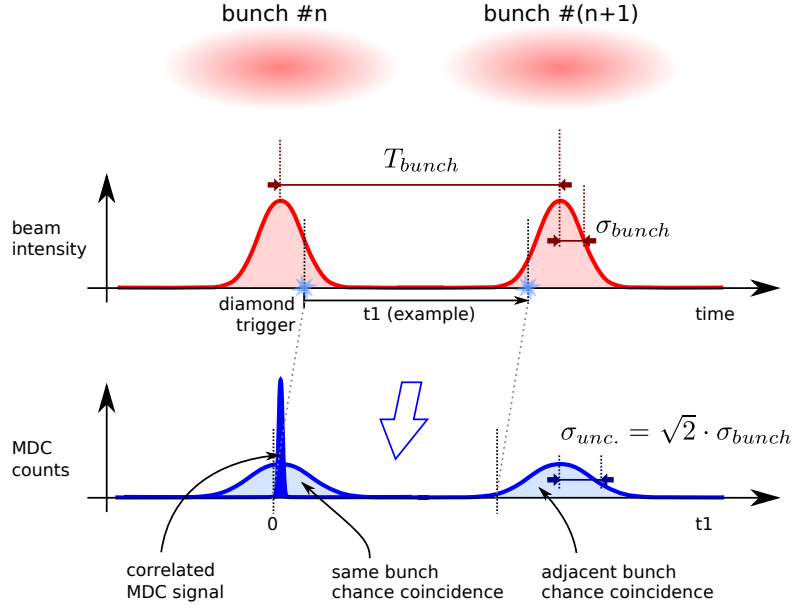


Figure 3.18: Sketch of the beam time structure.

The proton beam is bunched. Typically accelerator beam bunches have a Gaussian particle density profile in longitudinal direction, which automatically results in a Gaussian intensity profile in time (see figure 3.18). Let us assume we trigger on either electrode of the diamond detector (electrode A OR electrode B) and not on the gap. It is reasonable to assume that the trigger rate of the diamond detector is proportional to the average momentary beam intensity at the detector's position. A particle going through the diamond has already produced a signal in the upstream MDC cell which has a sharp time correlation with the diamond signal.

With a certain probability, which is also proportional to the beam intensity, a second beam particle will create an additional MDC signal within the read-out window. Especially in the adjacent bunch after the diamond was triggered, one measures pure random coincidences with the drift cell. Because both, the probability of observing a particle in the diamond detector and the probability of measuring a random coincidence in the MDC cell are proportional to the momentary beam intensity, the time difference, i.e. the  $t1$  of the random coincidence is distributed like the convolution of the intensity profile of a beam bunch with itself (neglecting the electron drift time distribution, which is much narrower than the width of the bunch). Consequently, the width of the uncorrelated MDC signal  $t1$  distribution is:

$$\sigma_{unc.} = \sqrt{2} \cdot \sigma_{bunch} \quad (83)$$

Figure 3.19 shows the drift cell  $t1$  distribution recorded with trigger on the full diamond detector, i.e. on either electrode. The shape of the distribution fits the above assumption. The left side of the distribution features a sharp peak with a Gaussian pedestal, while the right side can be fitted by a pure Gaussian with a width of  $\sigma_{unc.} = (68 \pm 5)$  ns. This corresponds to a bunch width of  $\sigma_{bunch} = (48 \pm 4)$  ns. Further we can determine the period between bunches to  $T_{bunch} = (670 \pm 20)$  ns. Relating the area of the right-hand



### 3.3 Time precision tests with proton beam

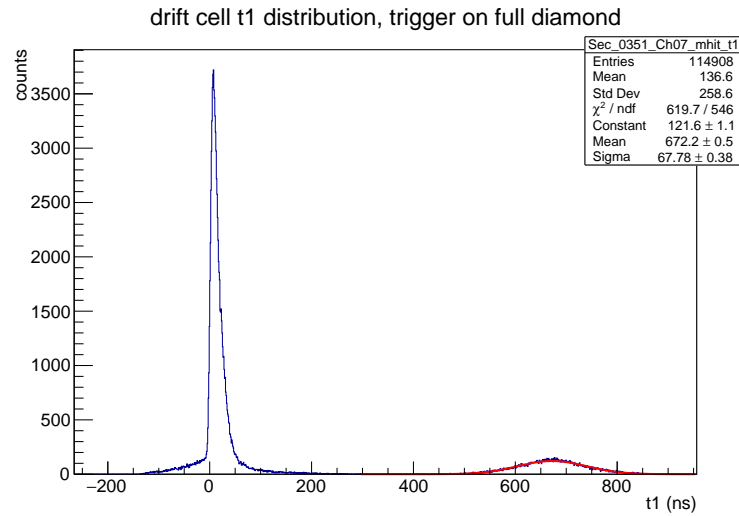


Figure 3.19: Multi-hit  $t_1$  distribution of drift cell signal with trigger on either electrode of the diamond detector.

side Gaussian and the number of triggers in the recorded dataset we can calculate that the probability for measuring an uncorrelated additional particle in the MDC is circa 20% in each bunch.

#### Intensity weighted acceptance of the diamond detector

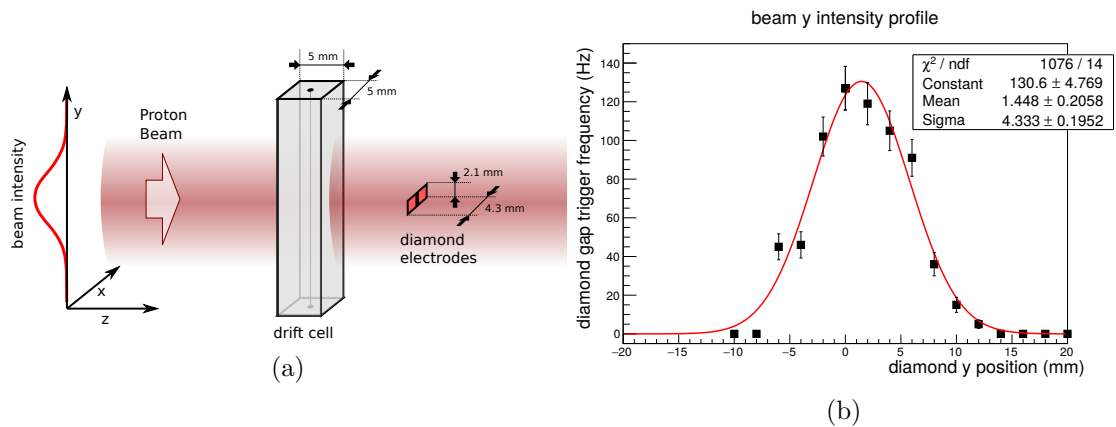


Figure 3.20: Drift cell and diamond electrode dimensions to scale (a) and beam intensity profile in  $y$  direction (b), fitted with Gaussian (fitted with equal weights for all bins).

Both, the drift cell and the full diamond detector have a comparable dimension in  $x$  direction: 5 mm vs 4.3 mm (see figure 3.20a). However, in  $y$  direction the drift cell is hit by the full beam, while the diamond detector only covers a small fraction (2.1 mm) of the intensity profile (figure 3.20b). From geometric considerations we can calculate that the diamond detector, when placed in the center of the  $y$  intensity profile, only receives 16.5% of the beam particles which hit the drift cell (that is 8.25% per electrode).

### 3 Extraction of drift time

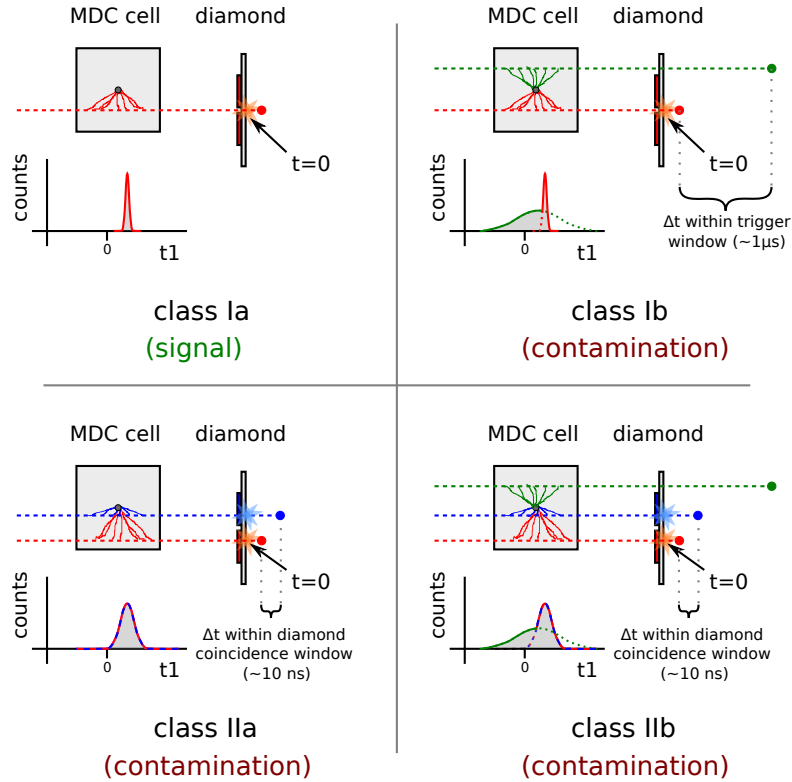


Figure 3.21: Possible detector signal coincidence classes.

#### Random coincidences as signal contamination

To assess the time precision performance of the drift cell we trigger on the coincidence of both diamond electrodes. In the following we want to distinguish all relevant classes of random detector coincidences and their effect on the observables of interest. In the default measurement mode, the TDC is operated in single hit mode which means that the first arriving signal determines the  $t_1$  measurement of the respective channel. Thus, in case a coincidence class consists of more than one particle  $t_1$  distribution, the distributions do not add but cut into each other. Locally, this is also the case for multi-hit measurements due to the dead time of the electronics. During the data taking with the described set-up the following relevant cases of signal coincidences can occur (see figure 3.21):

**Class Ia** A beam particle (red) traverses the MDC cell at a defined position and hits the diamond detector gap, thus causes a coincident firing of both diamond electrodes and triggers the data acquisition. This is the only case of interest for measuring the detector performance. The measured  $t_1$  distribution is very narrow and reflects the drift time distribution of a straight track at a fixed position. The probability per beam particle to cause a class Ia event is independent of the beam intensity. From the ratio of the diamond gap area ( $2.1 \text{ mm} \times 90 \mu\text{m}$ ) and the area under both diamond electrodes ( $2.1 \text{ mm} \times 4.3 \text{ mm}$ ) we calculate, that 2.3% of all particles impinging the active area of the diamond hit the gap and trigger the acquisition.

**Class Ib** A beam particle (red) traverses the MDC cell at a defined position and hits the detector gap (class I). In addition a second beam particle (green) traverses the MDC cell at a random position and produces an additional signal. In case the uncorrelated second particle traverses the set-up first (and depending on the

drift time of its ionization signal) it will determine the  $t1$  measurement and thus contaminate the detector performance measurement. As in the case when triggering on the full diamond, the probability of measuring an uncorrelated additional beam particle in the drift cell is proportional to the momentary beam intensity and thus the contamination  $t1$  distribution is very wide and reflects the longitudinal particle density profile of the beam bunch. Per triggered class I event, there is a 20 % chance for an additional uncorrelated beam proton hitting the drift cell. The probability has a Gaussian shape and a width of  $\approx \sigma_{unc.} = 68$  ns.

**Class IIa** Two beam particles traverse the MDC cell at undefined positions and each hit one diamond detector electrode within the narrow coincidence window ( $\approx 10$  ns) for triggering the data acquisition. The contamination is relatively narrow and is similar<sup>9</sup> to the  $t1$  distribution of a fully or partially irradiated drift cell (depending on diamond position), broadened by the width of the diamond coincidence window.

It was estimated that when the drift cell is hit by a proton, there is a 20 % probability that a second uncorrelated proton hits the drift cell during the same bunch. As discussed before, the diamond detector only receives circa 16.5 % of the beam particles which hit the drift cell, i.e. circa 8.25 % per electrode. The probability for an additional uncorrelated particle hitting the diamond is consequently  $20 \% \cdot 16.5 \% = 3.3 \%$ . Going further, we can state, that given one diamond electrode was hit, there is a  $20 \% \cdot 8.25 \% = 1.65 \%$  probability for the other electrode being hit during the same bunch. Just like the  $t1$  distribution of the uncorrelated particles measured by the drift cell, the time difference between the signals of both diamond electrodes has a Gaussian distribution with a width of  $\sigma_{unc.} = 68$  ns. We can estimate, that for a diamond electrode coincidence window of 10 ns, and given one electrode was hit, the probability for the other electrode being hit in coincidence drops to circa 0.2 %.

**Class IIb** The data acquisition is triggered by a random coincidence of two beam particles (red, blue) each hitting one diamond electrode (class IIa). The  $t1$  measurement of the drift cell is determined by an independent third particle (green).

Figure 3.22 shows the raw  $t1$  distribution of the drift cell with trigger on the diamond gap only. The dataset was recorded with the TDC in multi-hit mode and displayed with a logarithmic y-axis. There is a narrow peak near  $t = 0$  which corresponds to the coincidence classes Ia and IIa, i.e. cases, where the same particle or particles generate an MDC signal and trigger the data acquisition. Underneath the peak there is a much broader distribution with a peculiar shape. It comprises coincidence events of classes Ib and IIb. This claim can be confirmed by comparing it to the random coincidences in the next bunch, which can be seen as a second perfectly Gaussian shaped bump with its center at around 667 ns and a width of  $\sigma_{II} = 73$  ns. The pedestal underneath the narrow peak can be interpreted as being of the same origin, but cut on the left side by the TDC data acquisition window and suppressed by the dead time effect of the events in the narrow peak.

### 3 Extraction of drift time

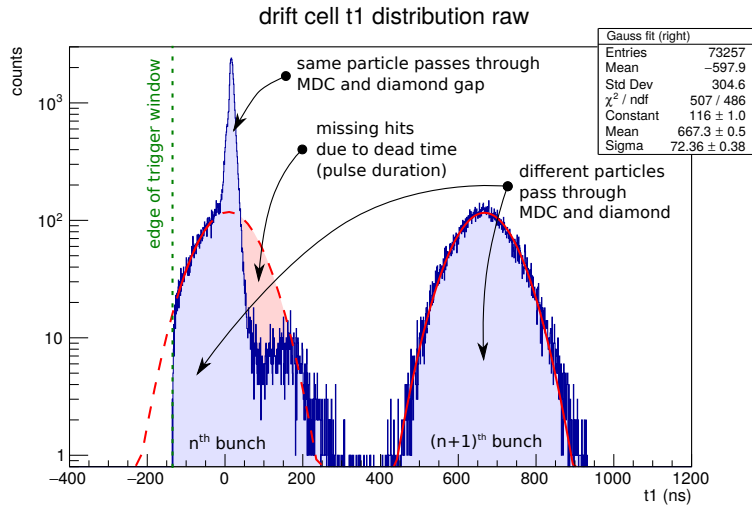


Figure 3.22: Raw measured  $t_1$  distribution with trigger on diamond gap. The distribution was recorded with PASTTREC and in multi-hit mode.

#### Auxiliary detector cut

The contamination of the data by coincidence classes Ib, IIa, and IIb can be reduced by applying a cut on  $t_1$  of the auxiliary detector. The  $t_1$  distribution of the scintillator (shown in figure 3.23a) has a prominent narrow peak. When fitted with a Gaussian, a peak width of  $\sigma_{aux} = 1.27$  ns is extracted. The auxiliary detector cut requires datasets to have an auxiliary detector  $t_1$  within  $\sigma_{aux}$  around the peak position. The cut discards events where a second particle passed through the system earlier than  $\sigma_{aux}$  before the triggering beam particle. This cut affects all contamination classes. Unfortunately, the auxiliary detector has a constant noise floor which affects the efficiency of the scintillator and the cut. In addition, the ToT distribution (figure 3.23b) is fitted with a Gaussian and an additional cut is performed on a  $\pm 2 \cdot \sigma_{ToT,aux}$  region around the ToT peak

<sup>9</sup>similar, but not identical, since there might be two tracks in the cell. Furthermore, depending on the position of the diamond gap, there are constraints on the positions of both tracks, since each track has to hit a separate diamond electrode.

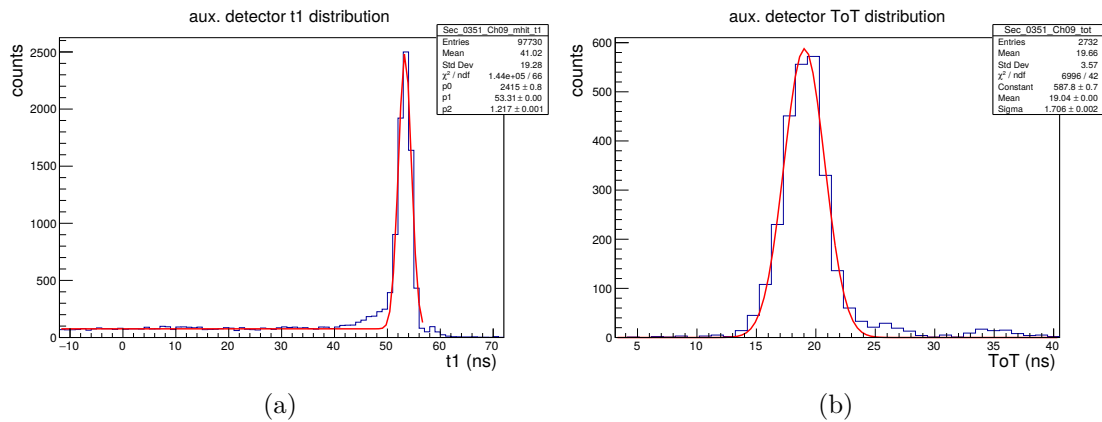


Figure 3.23:  $t_1$  (a) and ToT (b) distribution of the auxiliary detector. The ToT distribution was plotted after applying the  $t_1$  cut.

### 3.3 Time precision tests with proton beam

center. The ToT cut reduces events where a second particle arrives later than the triggering particle and the combined signals lead to an unusually long ToT measurement. The effect of the auxiliary detector cut is graphed in figure 3.24. The raw drift cell  $t_1$  distribution is shown in red and the same distribution after applying the cut is shown in blue. Both distributions are scaled to the same peak height. As expected, the cut drastically suppresses the broad leading Gaussian tail due to coincidences of class Ib and IIb. Furthermore, the leading "shoulder" of the main peak is reduced, which can be attributed to a suppression of class II events. Unfortunately, with this set-up class II events can only be suppressed but not be eliminated completely, because two perfectly coincident particles, each randomly hitting one of the diamond electrodes, cannot be distinguished from a single particle hitting the diamond gap.

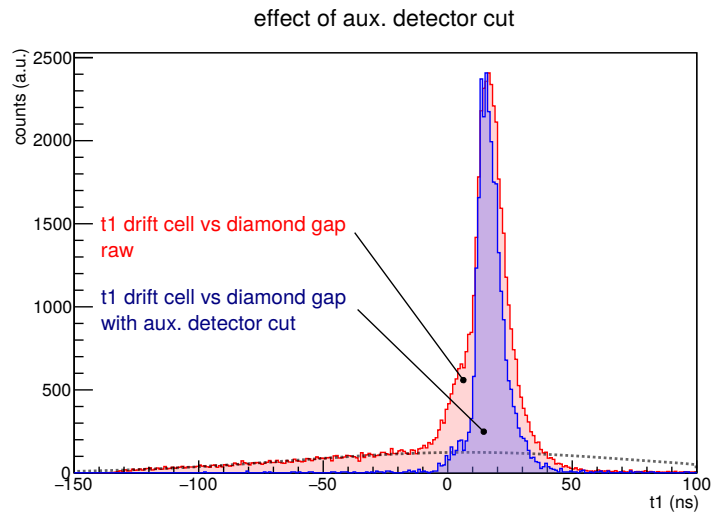


Figure 3.24: Effect of auxiliary detector cut.

### 3 Extraction of drift time

#### Feature extraction

The drift cell  $t_1$  distribution (see figure 3.25) is fitted with the skew normal distribution, which was introduced in section 3.2.7 and which is explained in detail in the appendix, section A.2. The fit function is extended with a broad Gaussian pedestal which is co-aligned with the mean of the skew normal peak, to describe the tails of the measured distribution. The features of interest are the mean  $\mu_{t_1,fit}$  and the standard deviation  $\sigma_{t_1,fit}$  of the skew normal distribution. The pedestal Gaussian is regarded as background. The  $t_1$  means at different positions within the cell yield the space-time relation of the drift cell, while the standard deviation is a measure for the time precision of detector and read-out electronics. To estimate the error of the extracted  $\sigma_{t_1,fit}$ , it is compared with the width of a plain Gaussian fit of the data. The discrepancy is used as the systematic error.

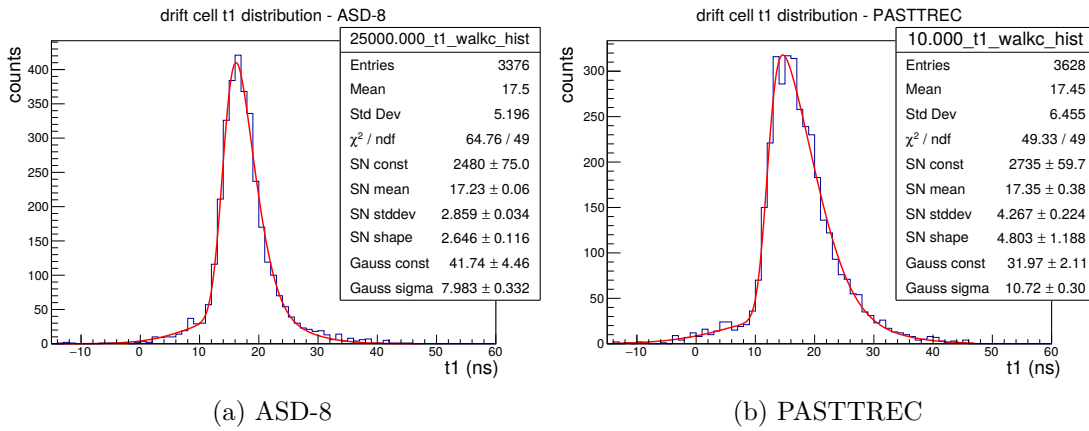


Figure 3.25:  $t_1$  distribution recorded with both front-end ASICs. Feature extraction (mean, standard deviation) is done by fitting a skew normal distribution with Gaussian pedestal to the  $t_1$  data after applying cuts.

### Walk correction

As discussed in the beginning of this chapter (section 3.1), when discriminating a signal with finite rise time by use of a plain comparator the walk effect plays a role. The walk effect describes a systematic shift of the measured  $t1$  depending on the input signal amplitude. A variation in input signal height results in a spread in  $t1$  for otherwise identical pulses. It has been found that the quality of the data recorded with PASTTREC can be improved offline by applying a walk correction. As an indirect measure for the pulse height the time over threshold ( $ToT$ ) is available. For a walk correction a correlation between  $ToT$  and  $t1$  needs to be found and exploited. A two-dimensional histogram relating  $ToT$  and  $t1$  is filled with TDC data from perpendicular particle tracks at a distance of 1.25 mm from the sense wire (figure 3.26a). The histogram has a clear skew for low  $ToT$  values towards larger  $t1$ . The walk  $\Delta t1_{walk}$  is modeled as an exponential function of  $ToT$ .

$$\Delta t1_{walk}(ToT) = a \cdot e^{-b \cdot ToT} \quad (84)$$

The free parameters  $a$  and  $b$  are determined by a two stage fitting procedure.

- The  $t1/ToT$  correlation histogram (figure 3.26a) is split in a multitude of  $ToT$  classes and the resulting  $t1$  histograms are fit individually with a Gaussian to obtain the most probable  $t1$  for each  $ToT$  class.
- The extracted data points  $t1_{MP}$  vs  $ToT$  are fitted with the above exponential function.

The walk correction is applied by subtracting the exponential correction term from the raw  $t1$  values:

$$t1 \rightarrow t1 - \Delta t1_{walk}(ToT) \quad (85)$$

The  $t1/ToT$  correlation histogram after the correction is depicted in figure 3.26b. Obviously the walk can be mitigated to a value well below the statistical  $t1$  fluctuations within the individual  $ToT$  classes.

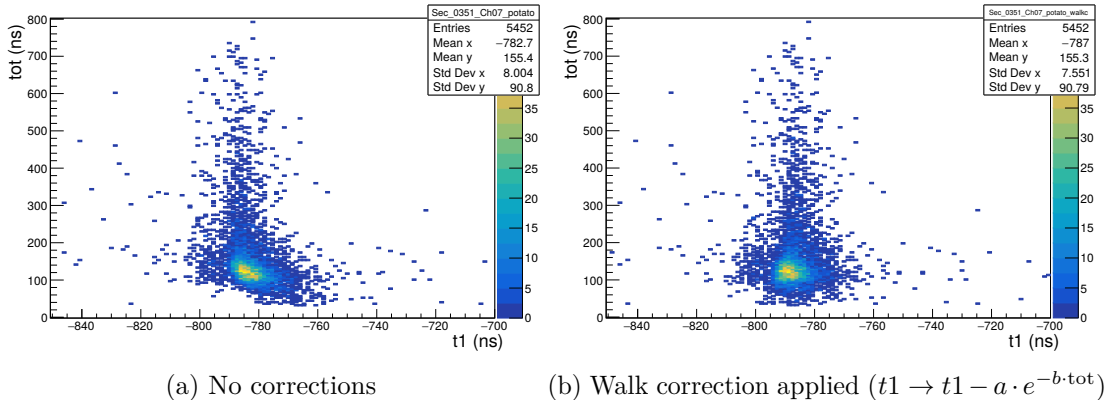


Figure 3.26: Visualization of the walk correction exploiting the correlation between time over threshold ( $tot$ ) and drift time ( $t1$ ). The correlation, i.e. the  $t1$  walk, is modeled as an exponential function of  $tot$ .

### 3 Extraction of drift time

An exponential correction function was chosen because of the following reasons:

- As shown in section 2.5.2, a three-stage unipolar shaper produces an approximately linear rising edge. This implies a linear relation between pulse height  $A$  of the shaped signal and the walk.

$$A \propto \Delta t_{walk}$$

- After shaping, the ion tail of the drift chamber is reduced to a mere exponential decay. By discriminating at a fixed threshold one can assume that  $ToT$  is proportional to the logarithm of the pulse height.

$$ToT \propto \log(A) \Rightarrow A \propto e^{const \cdot ToT}$$

And thus:

$$\Delta t_{walk} \propto e^{const \cdot ToT}$$

- For high  $ToT$  values (high pulse amplitude), the measured  $t1$  converges against the true arrival time of the pulse. Likewise, the chosen correction approaches zero for high  $ToT$  values due to the negative exponential dependence.

The magnitude of the walk effect depends on the discriminator threshold. Figure 3.27 shows the dependence of the  $t1$  precision on the threshold with and without automatic walk correction for each data point. As expected, the discrepancy between uncorrected and walk corrected precision is growing with increasing threshold, while for very small thresholds, the difference is negligible. In order to achieve optimal detection efficiency and noise immunity, i.e. signal to noise ratio, it can be desirable to not operate at the lowest possible threshold, but at a medium threshold and correct for the walk. However, for every threshold an individual walk correction calibration has to be found.

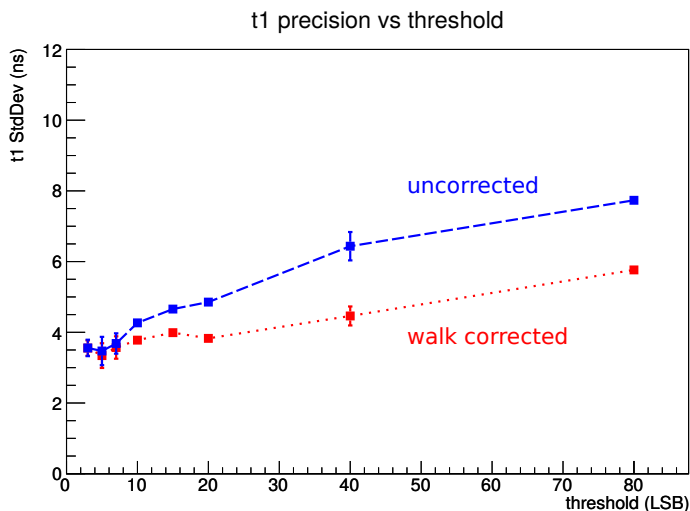


Figure 3.27: Time precision of drift cell with PASTTREC read-out as a function of threshold. Datasets were recorded for perpendicular tracks at a distance of 1.25 mm from the sense wire.



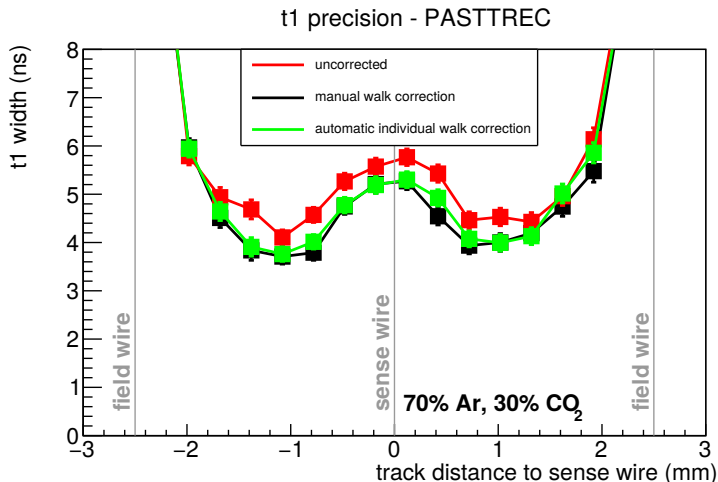


Figure 3.28:  $t_1$  precision measured with PASTTREC. Comparison of uncorrected data, automatic and manual walk correction.

Figure 3.28 shows the  $t_1$  precision as a function of track position within the drift cell. The same correction function can be applied to datasets from different positions with an average improvement in precision of 0.5 ns. Comparable results are achieved with an individual automatic walk correction for each individual data set. PASTTREC has a higher peaking time (10 - 35 ns) than ASD-8 (7 ns) and thus the walk effect is more prominent. The PASTTREC data shown above were recorded with the 15 ns peaking time setting. The data recorded with ASD-8 display a much smaller walk (see figure 3.29). The systematic skew is much smaller than the statistical spread of  $t_1$  per  $ToT$  slice, so a correction does not improve the  $t_1$  precision measurably.

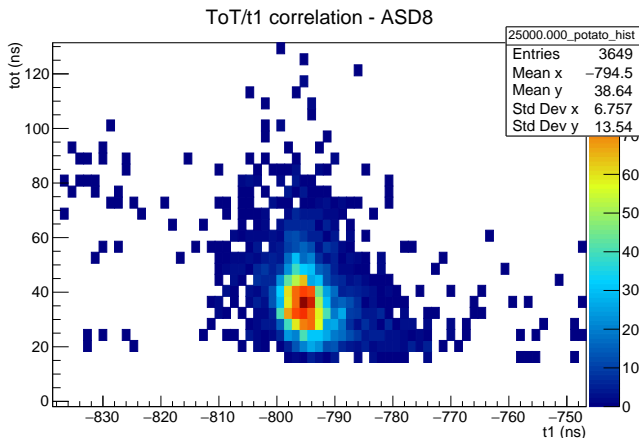


Figure 3.29:  $ToT/t_1$  correlation histogram for ASD-8. Due to the fast peaking time, the walk effect does not need to be corrected.

### 3.3.4 ASIC settings

Unlike the cosmic muon tracking system, the beam test allows for collecting enough statistics for evaluating an ASIC setting in a relatively short time. Thus the large settings space of PASTTREC can be explored to some extent in order to optimize the performance.

### 3 Extraction of drift time

However, because of the large parameter space, a pragmatic approach had to be chosen to make good use of the limited beam access time.

Of the four possible peaking time settings (10 ns, 15 ns, 20 ns, 35 ns) the fastest three settings were investigated. Likewise from the four possible preamplifier gain settings (0.67 mV/fC, 1 mV/fC, 2 mV/fC, 4 mV/fC) only the three highest gains are chosen for investigation. This pre-selection results in nine possible combinations of peaking time and gain (see figure 3.30). For each combination a threshold scan is performed at mid distance between sense wire and field wire, i.e. the position where the detector has the best time precision. A threshold scan means recording the drift time uncertainty as a function of the threshold setting of the PASTTREC ASIC. For pragmatic reasons, the list of investigated thresholds was reduced to the settings 3, 5, 7, 10, 15, 20, 40 and 80. From each scan the threshold with the best time precision was chosen as the optimal threshold for the respective gain/peaking time combination. As a general trend it was observed, that the time precision improves with a higher gain setting, while the signal to noise performance, which is related to the detection efficiency decreases. The inverse can be observed with increasing peaking time. The four degrees of freedom for the tail cancellation circuit were not varied. Instead the default settings [Str17] found for the PANDA straw tube system were retained. The best performing setting w.r.t. detection efficiency and time precision has been found with the following parameters:

- gain: 4 mV/fC
- peaking time: 15 ns
- threshold: 10
- tail cancellation shaper settings:  
 TC1C=10.5 pF, TC1R=27 kΩ,  
 TC2C=0.9 pF, TC2R=20 kΩ

These settings are used as the default in all following considerations. It has to be noted, that favored settings differ significantly from the settings used for the cosmic muon tracking set-up. For ASD-8, just like in the muon set-up, a threshold voltage of 1.26 V was used. Thus, at least for the ASD-8, the results from both set-ups can be compared directly.

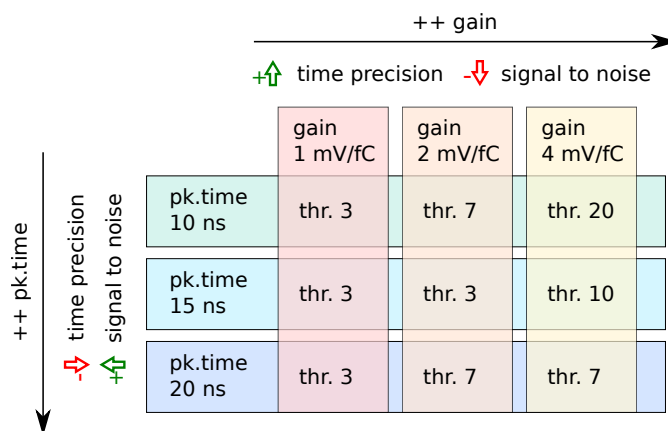


Figure 3.30: Matrix of investigated combinations of peaking time and gain settings for PASTTREC and optimal discriminator threshold for each combination.

### 3.3.5 Error analysis

#### Reference time error

To assess the timing error introduced by using an oscilloscope for reading out the diamond electrodes, a pulser signal is split and one branch is directly fed into the TDC, while the other branch is processed by the oscilloscope. Its trigger output is connected to a second TDC channel. The difference between both channels is histogrammed in figure 3.31. The spread introduced by the scope has a standard deviation of  $\sigma_{t_0, \text{scope}} = 0.3 \text{ ns}$ . This is the lower limit of the  $t_0$  time precision.

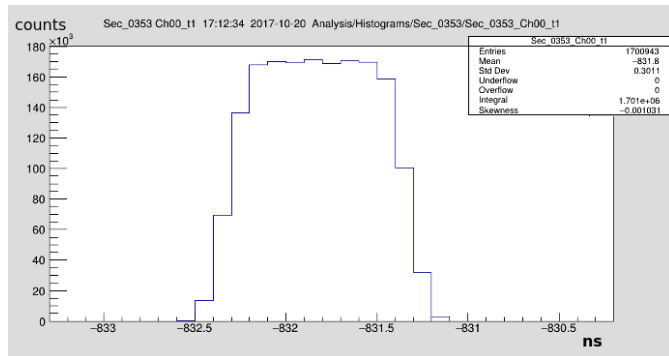


Figure 3.31: Time precision of oscilloscope trigger output.

The upper limit of the  $t_0$  measurement precision can be estimated by correlating the signals of the auxiliary detector and the full diamond detector (trigger on electrode A OR B). Both detectors are hit by the same monochromatic beam protons. As shown in figure 3.32, the time difference distribution has a sharp peak which is well approximated with a Gaussian of width  $\sigma = 0.78 \text{ ns}$ . The peak has an asymmetric tail to the left, which is interpreted as pileup coincidences (particles which fly past the diamond detector but hit the auxiliary detector shortly before the triggering particle).

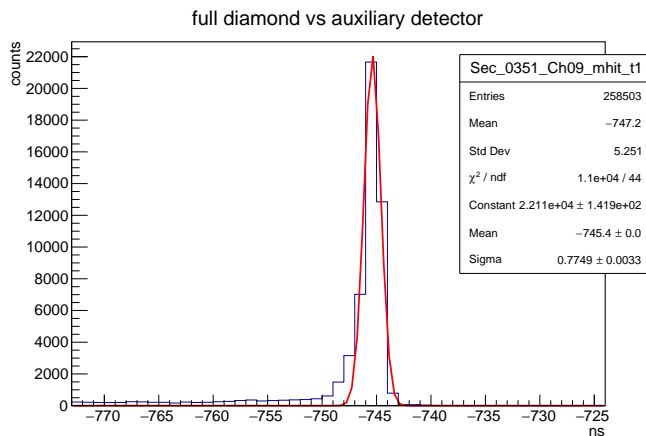


Figure 3.32: Time precision of diamond detector and auxiliary detector.

Assuming the auxiliary scintillator has a similar time precision as the scintillator used in the cosmic muon tracking set-up ( $\sigma_{t_0, \text{scint}} = 0.35 \text{ ns}$ ) one can estimate the upper limit

### 3 Extraction of drift time

for the reference time precision:

$$\sigma_{t_0} = \sqrt{(0.78 \text{ ns})^2 - \sigma_{t_0, \text{scint}}^2} \quad (86)$$

$$= 0.70 \text{ ns} \quad (87)$$

#### Diamond gap

Triggering on the diamond gap is the mechanism to select a narrow slice of the incoming proton beam, consequently this detector determines the spatial precision of the set-up. The gap has a width of  $90 \mu\text{m}$ . Assuming a perfectly parallel beam and a uniform hit distribution across the gap width, we select tracks with an RMS deviation in the  $y$  direction of

$$\sigma_{y, \text{gap}} = 90 \mu\text{m} \cdot \frac{1}{\sqrt{12}} = 26.0 \mu\text{m}. \quad (88)$$

It has to be noted, that the above error consideration is only an assumption, as the exact charge sharing behaviour between the electrodes is unknown.

#### Multiple scattering

A limiting factor for the spatial precision of the beam set-up is multiple scattering. The term describes the deflection of the particle trajectory while passing through matter. An exaggerated scattering trajectory is depicted in figure 3.33. For small angle scattering, the deflection can be approximated by the following formula [Hig75] [Lyn91]:

$$\theta_{\text{plane}}^{\text{rms}} = \frac{13.6 \text{ MeV}}{\beta c p} z \sqrt{x/X_0} (1 + 0.038 \ln(x/X_0)) \quad (89)$$

$$\psi_{\text{plane}}^{\text{rms}} = \frac{1}{\sqrt{3}} \theta_{\text{plane}}^{\text{rms}} \quad (90)$$

$$y_{\text{plane}}^{\text{rms}} = x \cdot \psi_{\text{plane}}^{\text{rms}} = \frac{x}{\sqrt{3}} \theta_{\text{plane}}^{\text{rms}} \quad (91)$$

The characteristic material constant for particle deflection is the radiation length  $X_0$ . Further the projectile charge number  $z$  plays a role.

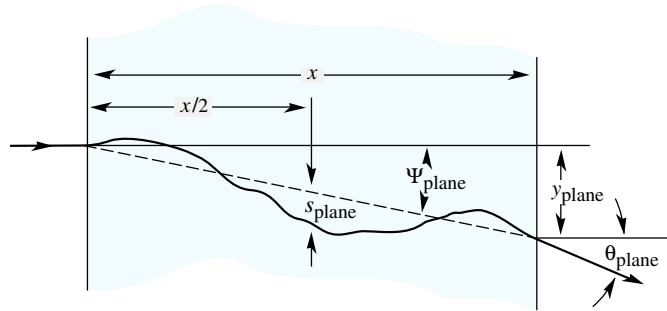


Figure 3.33: Multiple scattering in a homogeneous material. Image taken from [PDG16].

The relevant material budget (amount of matter in the particle trajectory) which fundamentally limits the spatial precision of the beam set-up is shown in figure 3.34. In the first order, when assuming a parallel incoming beam, only the material between the drift cell (device under test) and the diamond detector contributes to the uncertainty. The system only triggers on trajectories which are scattered into the diamond gap at

### 3.3 Time precision tests with proton beam

$y = y_{\text{diamond}}$ . These trajectories do not necessarily pass through the drift cell at the same  $y$  position but at  $y = y_{\text{diamond}} \pm \Delta y_{\text{MS}}$ . In order to estimate an upper limit for  $\Delta y_{\text{MS}}$  we calculate the multiple scattering deflection of a straight track parallel to the beam axis starting at the device under test, passing through

- 9 mm of detector gas (70 % Ar, 30 % CO<sub>2</sub>),
- the chamber window foil (12 μm Kapton, 400 nm aluminum) and
- 8 mm of air,
- a protective polyethylene foil (50 μm),
- a chemical beam monitor film (250 μm plastic)
- 33 mm of air.

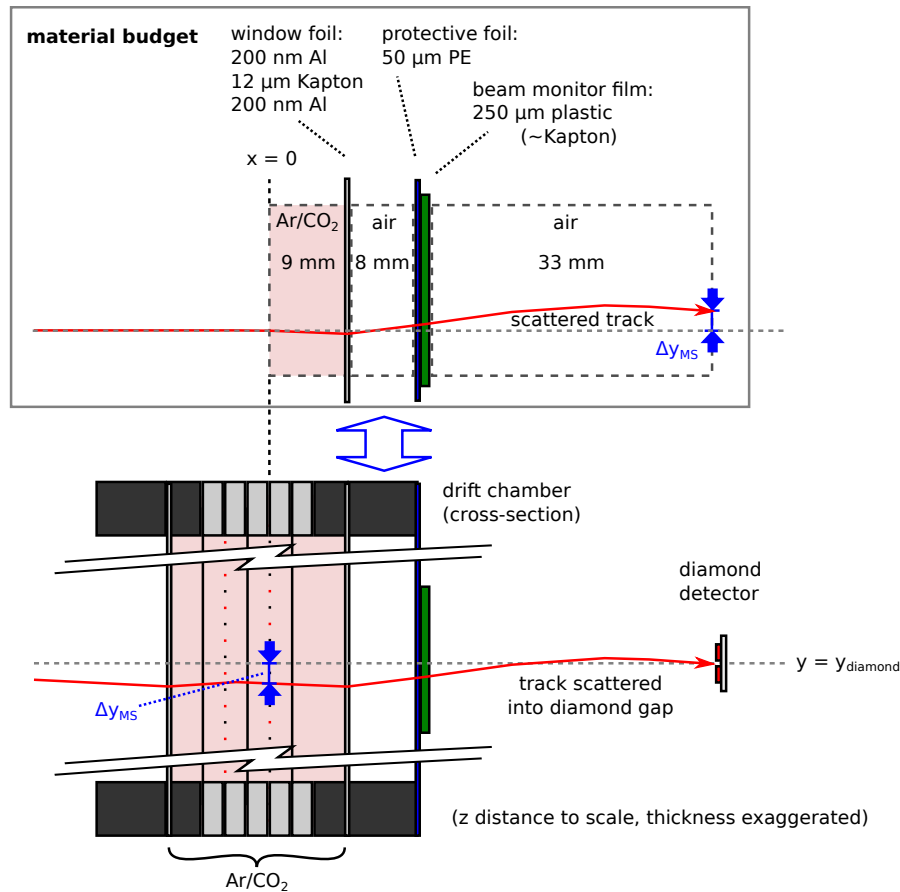


Figure 3.34: Material budget limiting the spatial precision of the set-up. The trajectory of the scattered track is exaggerated.

### 3 Extraction of drift time

Material	Thickness $x$	$X_0$ (m)	$\theta_{\text{rms}}$ (mrad)	$y_{\text{rms}}$ ( $\mu\text{m}$ )	$\sum \theta$ (mrad)	$\sum y$ ( $\mu\text{m}$ )
detector gas	9 mm	197 (CO <sub>2</sub> )	0.022	0.116	0.024	0.116
window foil	12 $\mu\text{m}$	0.29 (Kapton)	0.021	0.000	0.044	0.117
foil metallization	400 nm	0.09 (Al)	0.006	0.000	0.047	0.117
air	8 mm	303.9	0.016	0.076	0.061	0.590
protective foil	50 $\mu\text{m}$	0.50 (PE)	0.035	0.001	0.101	0.594
beam monitor film	250 $\mu\text{m}$	0.29 (Kapton)	0.115	0.017	0.216	0.636
air	33 mm	303.9	0.036	0.681	<b>0.252</b>	<b>8.38</b>
diamond	310 $\mu\text{m}$	0.121	0.208	0.037	0.461	8.50
air	266 cm	303.9	0.409	628	0.869	1860

Table 3.1: Cumulated spatial and angular deviation in the set-up due to multiple scattering.

The intermediate and cumulative results are shown in table 3.1. For the beam monitor film a high-density plastic material was assumed and the radiation length of Kapton was used. For the detector gas, the radiation length of pure CO<sub>2</sub>, which is shorter than the radiation length of argon. The calculation is extended by the scattering in the diamond detector and the air between diamond and auxiliary detector. In the calculation the worst case is assumed, i.e. that the  $y_{\text{rms}}$  and the  $\theta_{\text{rms}}$  of the individual layers add up every time:

$$\sum \theta = \theta_n = \sum_{i=1}^n \theta_{\text{rms},i} \quad (92)$$

Due to the very small amount of deflection it is allowed to sum the angles linearly ( $\sin(\theta) \approx \theta, \tan(\theta) \approx \theta$ ). Consequently, when calculating the cumulated  $y$  deviation, the net inclination due to all previous scattering processes is retained:

$$\sum y = \sum_{i=1}^n \left( x_i \cdot \frac{1}{\sqrt{3}} \theta_{\text{rms},i} + x_i \cdot \theta_{i-1} \right) \quad (93)$$

Even with the systematic overestimations, the multiple scattering due to the discussed material budget only causes a net deflection of  $\Delta y_{\text{MS}}$  of 8.4  $\mu\text{m}$ . In comparison with the uncertainty due to the limited width of the diamond gap ( $\sigma_{y,\text{gap}} = 26.0 \mu\text{m}$ ), the multiple scattering can be neglected in the quadratic sum.

#### Worst case scenario: divergent beam

In the case of a divergent beam it is possible to estimate the maximum occurring parallax, given that a beam particle hits the diamond gap and the auxiliary detector. A geometric construction of the parallax is shown in figure 3.35. It is found that

$$\Delta y_{\text{parallax}} = 3 \text{ cm} \cdot \frac{5 \text{ cm}}{266 \text{ cm}} = 564 \mu\text{m}. \quad (94)$$

In the limit of a strongly divergent beam the auxiliary detector is hit with uniform probability, so the standard deviation of the parallax error is

$$\sigma_{y,\text{parallax}} = 2 \cdot \Delta y_{\text{parallax}} \cdot \frac{1}{\sqrt{12}} = 326 \mu\text{m}. \quad (95)$$

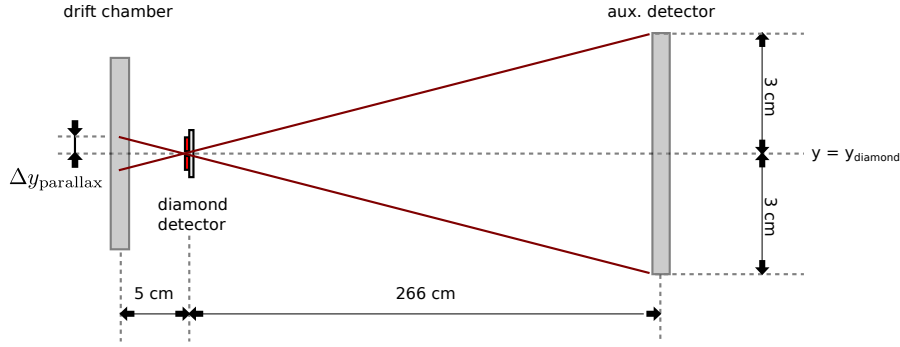


Figure 3.35: Parallax error in case of non-parallel beam.

When spatial information from the auxiliary detector is used, one has to account for the multiple scattering in the  $310\ \mu\text{m}$  thick diamond detector and the 266 cm of air between diamond and auxiliary detector. The additional scattering entities are already included in the previous calculation (see table 3.1). Multiple scattering accounts for an uncertainty of 1.86 mm at the auxiliary detector, which can be neglected in the following considerations. Combining the uncertainties of finite gap width, multiple scattering and the parallax we calculate the worst case  $y$  precision:

$$\sigma_{y,\text{worst case}} = \sqrt{(26\ \mu\text{m})^2 + (36\ \mu\text{m})^2 + (326\ \mu\text{m})^2} = 329\ \mu\text{m} \quad (96)$$

### Combined statistical $t1$ error of set-up

We distinguish between two extreme scenarios, i.e. a perfectly parallel beam and a completely divergent beam. In case of the parallel beam, the  $t1$  measurement precision is calculated as

$$\sigma_{t1} = \sqrt{(\sigma_{t0})^2 + \left(\frac{1}{v_D} \cdot \sigma_{y,\text{gap}}\right)^2} \quad (97)$$

$$= 0.80\ \text{ns}, \quad (98)$$

assuming a mean drift velocity of  $v_D = 66\ \mu\text{m ns}^{-1}$ . In case of a strongly divergent beam we obtain

$$\sigma_{t1,\text{worst case}} = \sqrt{(\sigma_{t0})^2 + \left(\frac{1}{v_D} \cdot \sigma_{y,\text{worst case}}\right)^2} \quad (99)$$

$$= 5.11\ \text{ns}. \quad (100)$$

### 3.3.6 Self-Tracking

Analog to the analysis of the cosmic muon tracking data, the self-tracking method, as described in section 3.2.3, can be applied to extract the  $t1$  precision from the correlations of two overlapping cells with identical read-out. Just as with the cosmic data, the precision is extracted by plotting the drift time sum under the condition, that the drift time difference is smaller than 10 ns. The resulting distribution is fitted with a skew normal fit (again allowing a small Gaussian pedestal which is discarded as background). The standard deviation of the fit corresponds to  $\sqrt{2}$  times the time precision at a distance of half a cell width (1.25 mm) from the sense wire. With the beam set-up, the self-tracking method can be used with two different modes of data taking:

### 3 Extraction of drift time

- When triggering on the full diamond (trigger on electrode A OR B) the drift time correlation has a similar “boomerang” shape as the correlations recorded with the cosmic set-up (see figure 3.36 and figure 3.38), because the whole overlap region of the staggered cells is illuminated.
- When triggering on the diamond gap (trigger on electrode A AND B), only correlations from tracks through the center of the overlap region are accepted. Only the center part of the “boomerang” shape remains (see figure 3.37 and figure 3.39).

As expected, the projections of both datasets for  $|T_a - T_b| < 10$  ns have similar shape and width. Self-tracking as an indirect method for extracting the time precision has the advantage, that its error depends less on the spatial precision of the diamond gap trigger and the angular homogeneity of the beam. It serves as a means of cross-checking the consistency of the direct  $t1$  and  $t1$  precision measurements at mid-distance from the sense wire. For the extraction of the  $t1$  precision the trigger is set on the diamond gap.

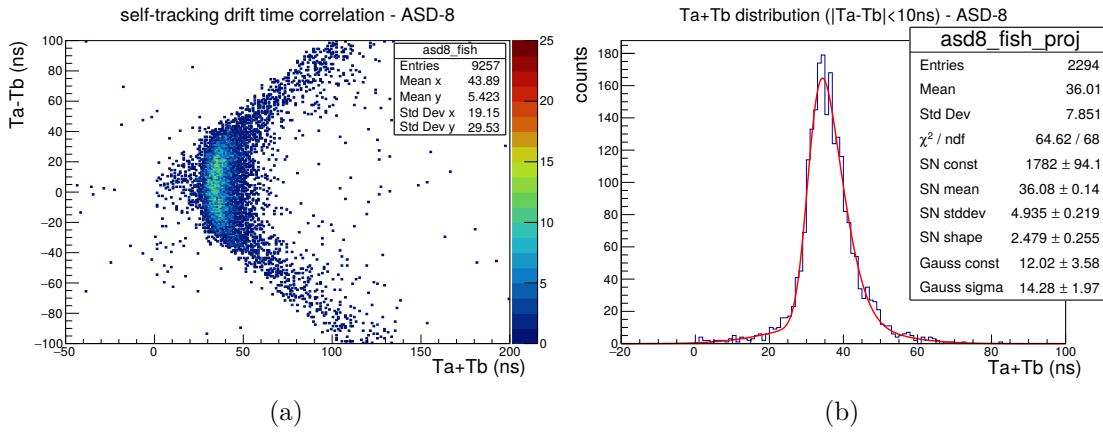


Figure 3.36: Self-tracking  $t1$  correlation recorded with ASD-8 and trigger on full diamond.

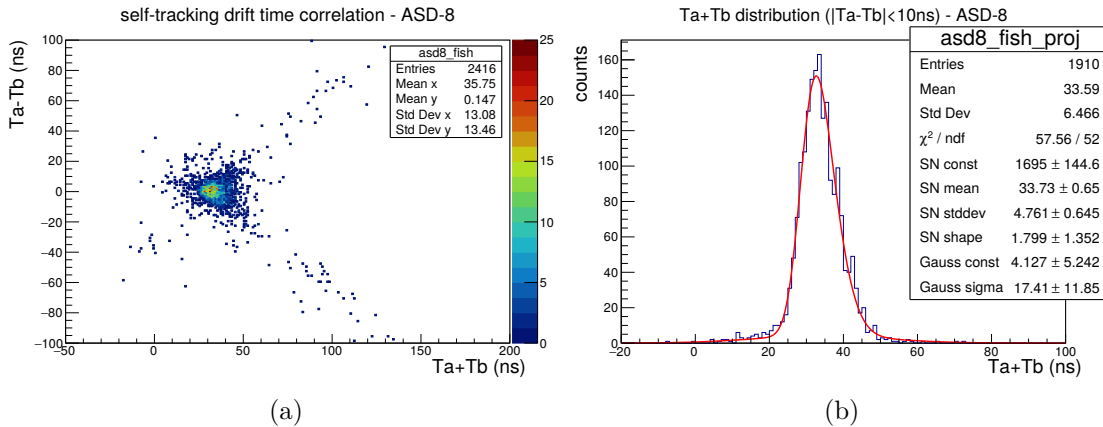


Figure 3.37: Self-tracking  $t1$  correlation recorded with ASD-8 and trigger on diamond gap.



### 3.3 Time precision tests with proton beam

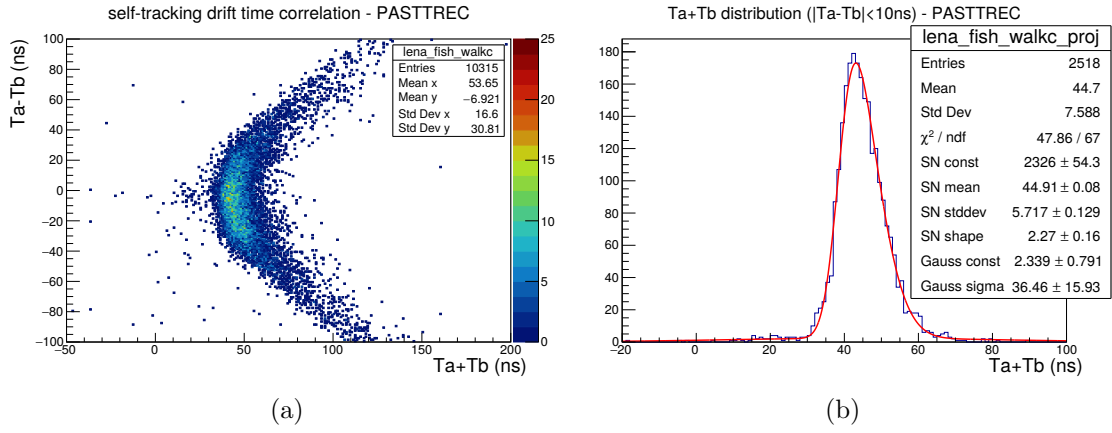


Figure 3.38: Self-tracking t1 correlation recorded with PASTTREC and trigger on full diamond.

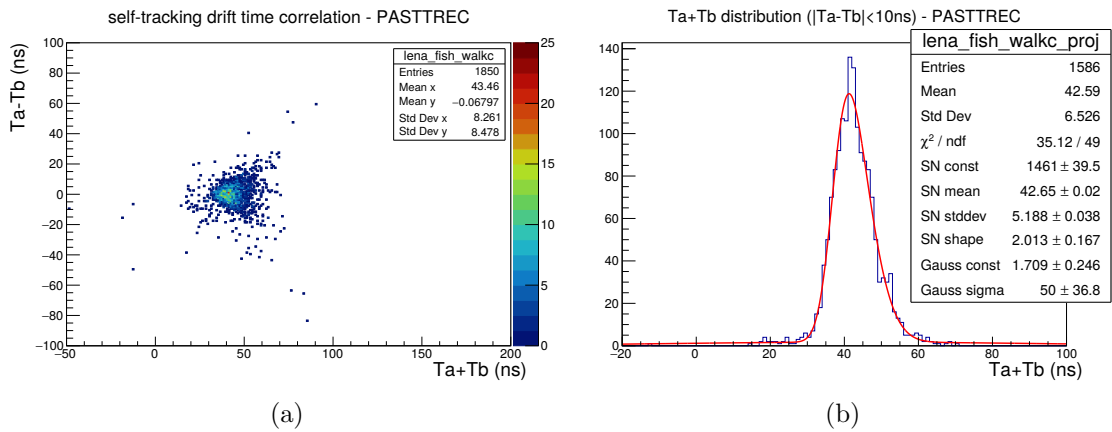


Figure 3.39: Self-tracking t1 correlation recorded with PASTTREC and trigger on diamond gap.

### 3.3.7 Self-Tracking error

To estimate the error of the  $t1$  precision determined via the self-tracking method in this set-up, we consider the worst case scenario again, in which we have a divergent beam and the auxiliary detector is hit uniformly. When triggering on the diamond gap, we have a maximum parallax angle of

$$\theta_{\text{parallax}} = \text{atan} \left( \frac{3 \text{ cm}}{266 \text{ cm}} \right) \approx \frac{3}{266} = 0.65^\circ. \quad (101)$$

With a uniform hit distribution on the auxiliary detector, this relates to a standard deviation in  $\theta$  of

$$\theta_{\text{RMS}} = 2 \cdot \frac{3}{266} \frac{1}{\sqrt{12}} = 0.37^\circ. \quad (102)$$

Using again the relation derived in the cosmic muon tracking set-up (see section 3.2.7, figure 3.9), we can calculate the maximum statistical error for measuring  $T_a + T_b$  due to track inclination as

$$\sigma_{(T_a+T_b),\theta} = 0.50 \text{ ns}. \quad (103)$$

Considering the  $t_0$  error, which affects both,  $T_a$  and  $T_b$  in correlation we can calculate the worst-case statistical error of the set-up in self-tracking mode:

$$\sigma_{(T_a+T_b),\text{set-up}} = \sqrt{\left(\sigma_{(T_a+T_b),\theta}\right)^2 + (2 \cdot \sigma_{t_0})^2} \quad (104)$$

$$= 1.48 \text{ ns}. \quad (105)$$

This error is dominated by  $\sigma_{t_0}$  (pessimistic estimation of reference time error) and not by the worst case beam divergence. In contrast to the cosmic muon set-up,  $\sigma_{(T_a+T_b),\text{set-up}}$  is a worst case estimation. Thus it is not quadratically subtracted from the measured and fitted precision  $\sigma_{(T_a+T_b),\text{fit}}$  in order to calculate the true precision  $\sigma_{(T_a+T_b),\text{MDC}}$  of detector and electronics. However, by doing the latter one can estimate an asymmetric systematic error of the measured and fitted precision in the direction of a better performance. The systematic error introduced by the fitting method is once again estimated by comparing the standard deviation extracted via the skew normal fit with the standard deviation of a plain Gaussian fit.

### 3.3.8 Results

#### Direct measurements

The main results of the beam test are shown in figure 3.40. Both ASICs deliver a very similar space-time relation. It has to be noted, that due to unknown signal propagation delays in cables and electronics, no absolute drift times can be measured. However, all  $t1$  measurements have the same constant  $t1$  offset. The offsets were tuned to bring the measured space-time relations into accordance with simulation results (see section 5.5). In the outer regions of the cell, close to the field wires, the space-time correlations diverge slightly, i.e. PASTTREC measures systematically longer drift times. Regarding the drift time uncertainty, both ASICs deliver a “W”-shaped curve, whereas the uncertainties measured with ASD-8 are systematically circa 0.6 ns lower than the uncertainties measured with PASTTREC. With both ASICs the best time precision is achieved at approximately

### 3.3 Time precision tests with proton beam

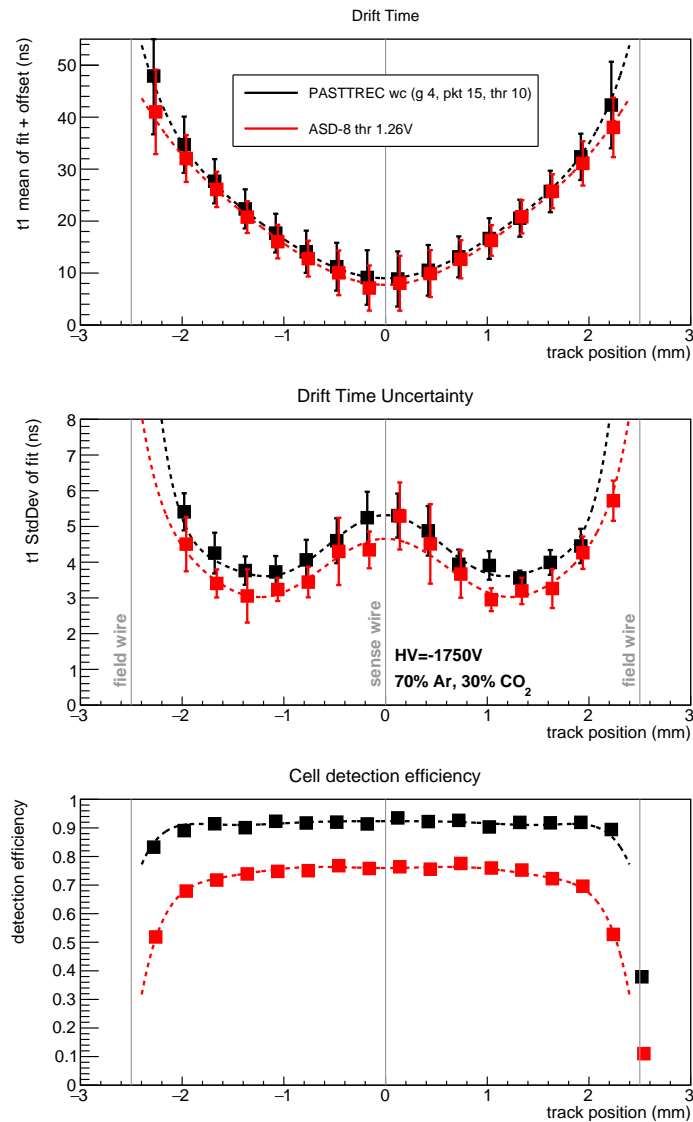


Figure 3.40: Measured space-time correlation  $t_1(x)$  and drift time uncertainty  $\sigma_{t_1}$  measured with both read-out ASICs. Error bars in the drift time plot correspond to the symbols in the drift time uncertainty plot. All plots are interpolated with a symmetric 8<sup>th</sup> order polynomial.

half the distance between sense wire and field wire, i.e. at a track position of  $\pm 1.25$  mm. Furthermore, the detection efficiency is depicted. The efficiency curves of both ASICs possess a plateau in the center of the cell with a slight decline towards the edges of the cell. The efficiency is calculated as the number of detector pulses within a window of 20 ns around the  $t_1$  peak divided by the number of triggers (coincidence of diamond gap trigger and auxiliary detector). The PASTTREC read-out has a much higher detection efficiency (92%, plateau) than the ASD-8 read-out (76%, plateau). To have a direct comparison, PASTTREC was also operated with the same settings again which were used in the cosmic muon tracking set-up (gain 1 mV/fC, peaking time 10 ns, threshold 10) and without walk correction. All three curves for both ASICs can be fitted with a symmetric 8<sup>th</sup> order polynomial function (orders 0,2,4,6,8) to interpolate the curve, while exploiting the symmetry of the cell for more stable results. From the interpolation we

### 3 Extraction of drift time

can extract the following data:

	drift velocity x= $\pm 1.25$ mm	time precision x= $\pm 1.25$ mm	time precision x=0 mm	detection efficiency x=0 mm
ASD-8 (thr 1.26V)	$(66 \pm 1) \mu\text{m/ns}$	$(3.0 \pm 0.4) \text{ ns}$	$(4.7 \pm 0.4) \text{ ns}$	76%
PASTTREC (walk cor.) (pkt 15 ns, gain 4, thr 10)	$(68 \pm 3) \mu\text{m/ns}$	$(3.6 \pm 0.3) \text{ ns}$	$(5.3 \pm 0.3) \text{ ns}$	92%
Cosmic set-up settings:				
PASTTREC (pkt 10 ns, gain 1, thr 10)	$(70 \pm 3) \mu\text{m/ns}$	$(5.2 \pm 0.5) \text{ ns}$	$(7.8 \pm 0.5) \text{ ns}$	75%

Table 3.2: Drift velocity and time precision extracted from the interpolation fit of the direct measurements. The drift velocity is calculated from the first derivative of the interpolated space time relation. The systematic error of the precision is calculated as the average systematic error of interpolated data points. The error of the drift velocity is attained by fitting left and right half of the symmetric cell independently and taking the biggest observed discrepancy in the derived velocity.

#### Self-tracking measurements

The results of the self-tracking method are shown in table 3.3. For PASTTREC, both the direct measurement and the self-tracking measurement yield very similar results for the time precision (3.6 ns direct, 3.7 ns self-tracking), while for ASD-8 the precision is slightly worse via the self-tracking method (3.0 ns direct, 3.4 ns self-tracking). As discussed above, in case of a strongly divergent beam leading to a uniform illumination of the auxiliary detector, we expect the self-tracking time precision to be significantly better than the directly measured time precision, because the self-tracking relies far less on a parallel beam. In fact we observe the opposite, i.e. that the directly measured time precision is the same or better than the precision measured via self-tracking. This means that the angular spread of the beam is relatively small and most likely negligible. The worse time precision measured via the self-tracking method is most likely explained by the higher systematic dependence of the  $t_0$  measurement error. As before, PASTTREC was, in addition, operated with the settings used in the cosmic muon tracking set-up for comparison.

	$\sigma_{(T_a+T_b)}$	$\sigma_{t1}$
ASD-8 (thr 1.26V)	$4.7^{+0.37}_{-0.61} \text{ ns}$	$3.37^{+0.26}_{-0.43} \text{ ns}$
PASTTREC (walk cor.) (pkt 15 ns, gain 4 mV/fC, thr 10)	$5.31^{+0.24}_{-0.45} \text{ ns}$	$3.67^{+0.13}_{-0.28} \text{ ns}$
Cosmic set-up settings:		
PASTTREC (pkt 10 ns, gain 1 mV/fC, thr 10)	$7.77^{+0.62}_{-0.77} \text{ ns}$	$5.5^{+0.44}_{-0.54} \text{ ns}$

Table 3.3: Results of the self-tracking method applied to the beam test data.

### 3.4 Summary and discussion of drift time precision measurements

The time precision of the MDC I cell read-out with two different ASICs was assessed in two different set-ups using two complementary methods. The cosmic muon tracking set-up allowed for an indirect measurement of the time precision at mid-distance (1.25 mm) between sense wire and the field wire via the self-tracking method. The beam test set-up allowed for both, a direct measurement of the drift time precision at any distance from the sense wire and an indirect measurement via self-tracking. This set-up confirmed, that the time precision of an MDC I cell is indeed the best at mid-distance between sense wire and field wire.

In the cosmic set-up, the PASTTREC chip was operated with non-optimal settings (gain 1 mV/fC, peaking time 10 ns). During the beam test, due to the access to higher statistics, better settings could be found (gain 4 mV/fC, peaking time 15 ns) and the performance was even more enhanced by applying a walk correction on the recorded data. For comparison, the PASTTREC settings used in the cosmic set-up were evaluated again during the beam test. The time precisions, determined by all methods are depicted for comparison in figure 3.41. Comparing the direct measurements and self-tracking results from the beam test, one observes that both methods yield similar results which are consistent within their systematic errors for both ASICs and for both investigated PASTTREC settings. Due to the consistency of both techniques, one can assume that the amount of angular spread of the beam is not the limiting factor for determining the time precision with this set-up. The new PASTTREC settings, found during the beam test, and the additional walk correction significantly improve the time precision by circa 1.5 ns in contrast to the initially used settings.

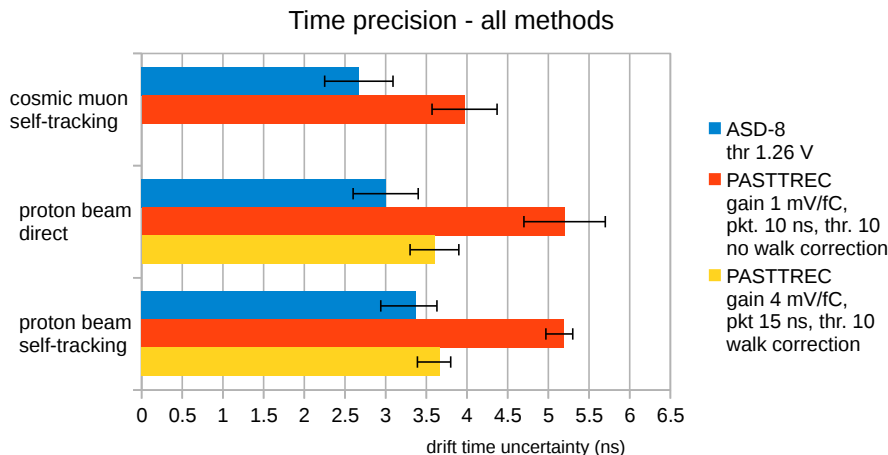


Figure 3.41: Comparison of drift time precisions determined by all employed methods.

Comparing the beam test results to the cosmic muon tracking results one observes a slight decline in the ASD-8 performance and a noticeable decline in the PASTTREC performance. A possible explanation is the higher average deposited charge in the non-minimum ionizing muon tracks in the cosmic set-up, compared to the true minimum ionizing protons in the beam test set-up. As discussed before, the average muon has a kinetic energy of 4 GeV, which leads to 27% more ionization than a minimum ionizing particle. In fact, when the average inclination of tracks in the cosmic set-up is considered, the amount of ionization is 37.4% higher than for a minimum ionizing particle. A higher

### 3 Extraction of drift time

ionization density along the track results in a faster rise of the shaped signal above the discriminator threshold, and thus less arrival time fluctuations.

The relatively poor detection efficiency, especially the efficiency measured with ASD-8, can be attributed to the influence of electromagnetic interference. During the beam test, when operated at the desired settings, i.e. the desired discriminator thresholds, both ASICs produce digital pulses caused by noise with a rate between hundreds of kHz and few MHz, depending on the activity of devices in the beam test cave. Reacting to a noise signal introduces a dead time, during which actual detector signals are lost and thus the detection efficiency is reduced. Furthermore it is known to the community, that the ASD-8 chip is prone to self-oscillation [Sch01], caused by the feedback of the digital output signals into the sensitive analog inputs. In the oscillating state, a channel is not able to process a detector signal properly. This phenomenon results in a loss of efficiency. Without developing elaborate grounding and shielding concepts for ASD-8 based hardware, it is impossible to achieve optimal detection efficiency [Sch01]. In order to operate ASD-8 in direct comparison to PASTTREC, an active adapter board was designed to host a HADES MDC I ASD-8 daughterboard, so that both ASICs can be read out with the same TDC. For pragmatic reasons no extensive studies on optimizing the adapter board for optimal grounding and noise/oscillation immunity could be performed in the scope of this thesis. However, one can state, that the PASTTREC chip appears to have less problems concerning pick-up noise and self-oscillation, when using similar measures for providing the connection between the respective read-out board and the drift chamber ground.

## 4 Measuring energy loss

Both ASICs, ASD-8 and PASTTREC provide energy loss information, i.e. a quantity that is related to the amount of ionization charge in the detector cell. In both cases the measured observable is the time over threshold duration  $ToT = t_2 - t_1$ . The measured  $ToT$  is not necessarily a linear function of the charge. In the following section a method is presented to determine a charge calibration function  $Q(ToT)$  for both ASICs using a programmable signal generator which mimics a drift chamber signal. Unlike the real detector signal the mimic signal is static and does not undergo fluctuations. The calibration set-up is then further used to study the intrinsic time and charge measurement capability of both electronics. Subsequently the charge measurement precision of the joint system comprising MDC and PASTTREC is assessed using monochromatic X-ray photons from an  $^{55}Fe$  source. Finally the calibrated charge measurement capability of PASTTREC is applied to analyze the charge spectra of minimum ionizing protons recorded during the beam test.

### 4.1 ASIC settings

For recording the charge calibration function, both ASICs were operated with the respective optimal settings which were empirically determined during the beam test. For ASD-8, the threshold was set to 1.26 V. PASTTREC was programmed with the following settings:

- gain: 4 mV/fC
- peaking time: 15 ns
- threshold: 10
- tail cancellation shaper settings:  
TC1C=10.5 pF, TC1R=27 k $\Omega$ ,  
TC2C=0.9 pF, TC2R=20 k $\Omega$

### 4.2 Recording the charge calibration function

As discussed before, an essential feature of the shaper in the read-out ASICs is to integrate the input pulse charge and to create an output pulse with an amplitude that is proportional to the received charge. When measuring the time over threshold duration, we record a quantity that is a function to the amplitude, and thus the signal charge can be obtained via the respective calibration function.

If the input pulse is short compared to the peaking time of the shaper ( $< \text{peaking time}/2$ ), the shaped pulse resembles the delta response of the shaper and the amplitude only depends on the charge of the input pulse. In the case of drift chamber read-out, this is not the case. Due to the peculiar shape of wire chamber signals, i.e. the  $\frac{1}{t}$  signal tail, a significant amount of input signal charge does not contribute to the amplitude or  $ToT$  of the shaped pulse, a feature which is termed the ballistic deficit. In general, the measured  $ToT$  does not only depend on the input charge but also on the signal shape. Consequently the calibration function is recorded using a programmable pulse generator which is configured to reproduce the exact shape of a drift chamber signal with varying amplitude and thus varying charge. The waveform generator is programmed with the previously recorded drift chamber signal, described in section 2.4.2, which is the detector's raw signal in response to X-ray photons from an  $^{55}Fe$  source. This signal is very similar

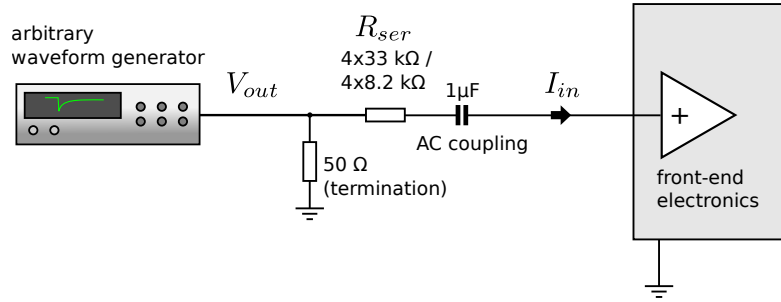


Figure 4.1: Schematic of the charge calibration set-up.

to the impulse response function of the detector and it features the characteristic long ion tail.

The output of the waveform generator is connected to the read-out electronics according to the schematic in figure 4.1. First the output line is terminated with a  $50\ \Omega$  resistor to avoid reflections and to have a defined voltage  $V_{out}$  at the coupling circuit. In the following the signal is fed into the signal input via a resistor and an AC coupling capacitor wired in series. The serial resistor  $R_{ser}$  has a resistance much larger than the input impedance  $Z_{in}$  of the signal input. Thus almost the entire input voltage is dropped across  $R_{ser}$ . As a consequence, the current flowing into the signal input is proportional to  $V_{out}$  and can be easily calculated:

$$R_{ser} \gg Z_{in} \quad (106)$$

$$I_{in}(t) = \frac{V_{out}(t)}{R_{ser} + Z_{in}} \approx \frac{V_{out}(t)}{R_{ser}}. \quad (107)$$

This way, also the charge of the pulse is known for arbitrary amplitude settings, as it is simply the integral of the current over time. Although the waveform sample only captures the first  $1.6\ \mu\text{s}$  of the drift chamber pulse, the total charge  $Q^{total}$  at  $T^+$  (after the complete ion drift) can be estimated by comparison with the SPICE simulation (see section 2.4.4). It is found, that  $Q^{total}/Q(1.6\ \mu\text{s}) \approx 1.53$ . However, in the relevant cases, the shaped pulse returns to the baseline long before the end of the pulse sample is reached. Nevertheless, for the charge measurement calibration the estimated  $Q^{total}$  value is used.

Figure 4.2 shows the charge calibration curve recorded with PASTTREC. The same range of voltages is recorded twice with different serial resistors ( $4 \times 33\ \text{k}\Omega$  and  $4 \times 8.2\ \text{k}\Omega$ ) to cover different dynamical ranges. As expected, both curves lie on top of each other. In practice,  $R_{ser}$  consists of four identical resistors wired in series, to reduce the parallel capacitance of  $R_{ser}$ . If not mitigated, the parallel capacitance significantly contributes to the signal injection and the injected charge differs from the calculated value. When recorded with the full parallel capacitance of a single resistor, the calibration curves recorded with different  $R_{ser}$  do not align. For ASD-8, the respective calibration curve is shown in figure 4.3.

As discussed in section 3.3.3 (walk correction), in theory the tail cancellation circuit shortens the  $\frac{1}{t}$  shaped signal tail to a mere exponential decay. When discriminated against a fixed threshold, one expects a logarithmic dependence of the time over threshold duration on the signal amplitude/charge. The calibration curves of both ASICs begin, as expected, with a logarithmic rise. For comparison, this region was fitted with a logarithm in the above figures. Towards higher induced charges, at a certain point the calibration curve transitions to an approximately linear rise. This is a feature of the non-linear behavior of the analog circuit, which comes into play for large signals.



## 4.2 Recording the charge calibration function

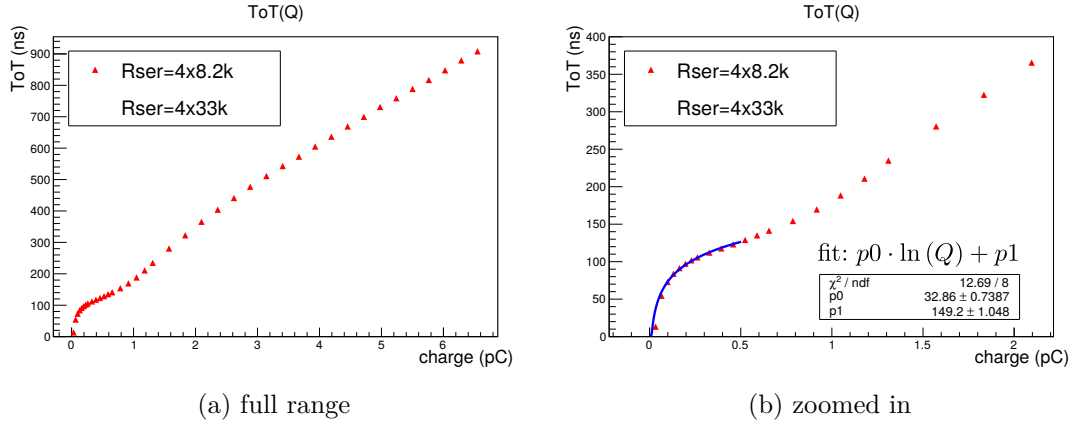


Figure 4.2: Charge calibration function of PASTTREC recorded with arbitrary waveform generator. Statistical error bars are smaller than symbols. ASIC settings: gain: 4 mV/fC, pk. time: 15 ns, threshold: 10, TC1C=10.5 pF, TC1R=27 kΩ, TC2C=0.9 pF, TC2R=20 kΩ

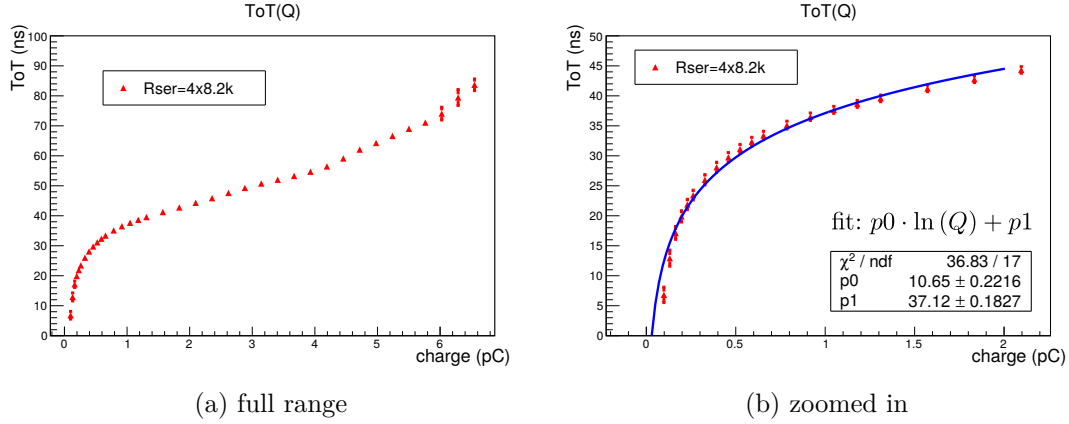


Figure 4.3: Charge calibration function of ASD-8 recorded with arbitrary waveform generator. Threshold voltage=1.26 V

### 4.2.1 Intrinsic charge measurement precision of electronics

Using the acquired calibration function  $Q(ToT)$  on the very same data that it was derived from, one can calculate the charge measurement precision of both versions of front-end electronics in the given set-up. The relative charge precision is graphed in figure 4.4. This quantity is calculated as follows:

$$\frac{\sigma_Q}{Q} = \frac{\sigma_{ToT}}{Q} \cdot \frac{dQ(ToT)}{dToT}. \quad (108)$$

PASTTREC yields a charge precision of better than 5% below 1 pC and well below 1% above 1 pC. With ASD-8, the charge precision is below 8% and declines more slowly for higher injected charges. These values are not necessarily the true intrinsic charge measurement precision of the electronics, since the measurement set-up can introduce unknown additional sources of error. However, the intrinsic charge measurement precision is at least as good as the above values.

## 4 Measuring energy loss

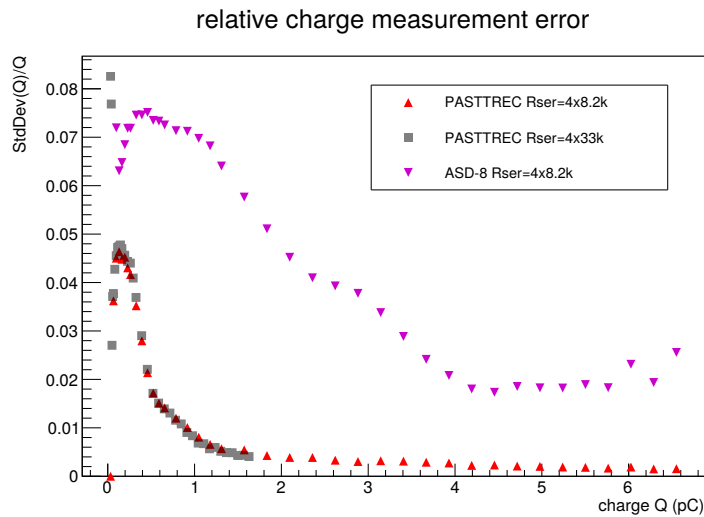


Figure 4.4: Relative charge measurement precision assessed with both ASICs in the charge calibration set-up.

### 4.2.2 Intrinsic time measurement precision of electronics

As a side product, the calibration set-up also measures an upper limit of the intrinsic time precision of the electronics. The plain standard deviation of the  $t_1$  measurement (no fit) is graphed in figure 4.5 for both ASICs. Above a signal charge of 100 fC, the PASTTREC time precision is better than 0.5 ns, and above 200 fC, the ASD-8 time precision is better than 0.5 ns. As it was stated for the intrinsic charge measurement precision, also this measured quantity can depend on additional uncertainties introduced by the measurement set-up. Still, the intrinsic time precision is better or equal to the measured precision.

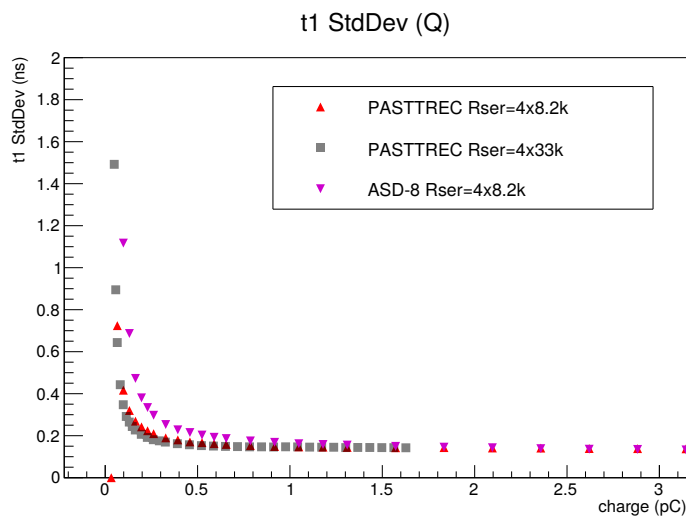


Figure 4.5: Time precision of both ASICs measured with the charge calibration set-up.

### 4.3 Charge measurement precision with $^{55}\text{Fe}$ source

In order to test the charge measurement capability with real detector signals, both ASICs are connected to a prototype chamber with MDC I wire geometry which is then irradiated with X-ray photons from an  $^{55}\text{Fe}$  source. The read-out electronics are connected to the drift chamber as described in section 3.2.5, and the ASICs are operated with the same settings which were used for the charge measurement calibration. While the photons can only deposit fixed amounts of ionization, the total charge of the detector signal can be varied by operating the detector at different high voltage settings, and thus, different gas amplification factors. Because the X-ray photon only interacts with the detector at a distinct position, where it transfers all its energy, it cannot be tracked like a cosmic muon or a minimum ionizing proton. Therefore there is no means to trigger the data acquisition on the advent of a photon absorption. As a consequence the system records both, true detector signals and noise.

#### 4.3.1 Ionization by $^{55}\text{Fe}$ radiation in Argon, escape peak

As discussed in section 2.4.3, for all practical applications  $^{55}\text{Fe}$  can be regarded as an emitter of monochromatic X-ray radiation with an energy of 5.9 keV. In an MDC detector cell, which is mostly filled with Argon, the X-ray photons can interact with the gas atoms via the photo effect. For the given photon energy of 5.9 keV, the interacting electron of the argon atom is in the K-shell, which has a binding energy of  $E_k = 3.2$  keV [NIS18]. The ejected electron receives a kinetic energy of  $5.9 \text{ keV} - 3.2 \text{ keV} = 2.7 \text{ keV}$  and creates ionization in the detector gas in proportion to its energy. The excited remaining argon atom either de-excites via fluorescence, i.e. by emitting a photon, or via the Auger effect, i.e. by ejecting another electron with a kinetic energy of nearly  $E_k$ . In argon, fluorescence occurs with a probability of circa 15 %, while the transition via the Auger effect is favored with a probability of 85 % [Sau77]. In Argon, the fluorescence photon has a mean attenuation length (range) of circa 3 mm [NIS18]. Therefore it is possible for the photon to either deposit its energy in the cell or to escape the cell. As a result, the detector measures two distinct energies, the full 5.9 keV of the initial X-ray photon and the 2.7 keV in case the secondary photon escapes the cell. The latter is called the argon escape peak.

#### 4.3.2 Analysis

In the case of PASTTREC it is possible to record clear detector signals with a minimum amount of deterioration due to noise. In the case of the ASD-8 based hardware, however, the recorded spectra are dominated by noise and display no clear features for analysis. Therefore no further efforts were taken to analyze these data. Figure 4.6 shows the recorded raw time over threshold spectrum recorded with PASTTREC and the calibrated charge spectrum using the earlier recorded calibration function. The charge histogram is fitted with the superposition of two Gaussian functions, from which the location and the width parameter are extracted. To estimate the systematic error of the fit, the same fit is repeated but with identical regression weights for every bin, i.e. regardless of the bin content. The difference between the peak positions and widths extracted with both methods is used as systematic error. The procedure is repeated for every setting of the high voltage scan. The entirety of the spectra recorded with PASTTREC is shown in the appendix, section A.3.

## 4 Measuring energy loss

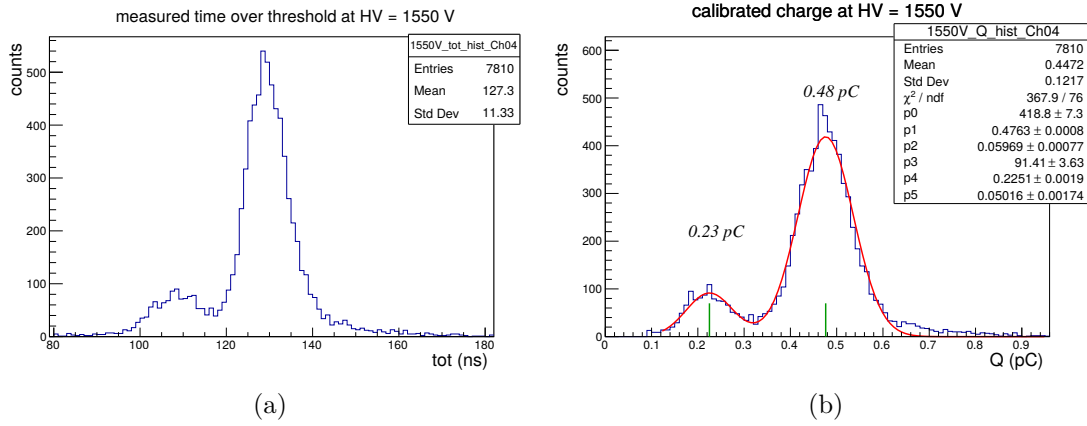


Figure 4.6: Time over threshold spectrum (a) and derived calibrated charge spectrum (b) recorded with PASTTREC.

### 4.3.3 Results

The measured charges of the main and the escape peak of the calibrated spectra are graphed in figure 4.7a. The width of the charge peaks is shown as error bars. For both peaks there is a similar, approximately exponential dependence between charge and high voltage. Regarding the charge ratio between main peak and escape peak, the measured ratio deviates only 10 % from the expected ratio of 5.9 keV/2.7 keV for voltages up to 1700 V. Above 1700 V the ratio drops because the main peak charge increases more slowly than the escape peak charge. The total amount of ionization charges  $n_T$  in the cell depends on the deposited energy  $\Delta E$  and the mean ionization energy  $W_i$ . It can be calculated as follows [Sau77]:

$$n_T = \frac{\Delta E}{W_i}. \quad (109)$$

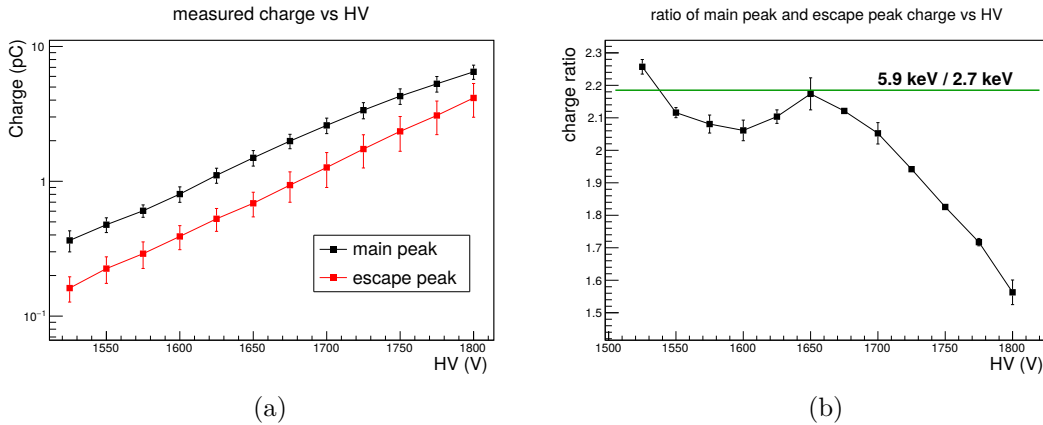


Figure 4.7: Measured charge (a) and ratio of charges of main and escape peak (b) measured with PASTTREC. The error bars in (a) indicate the width of the respective peaks.

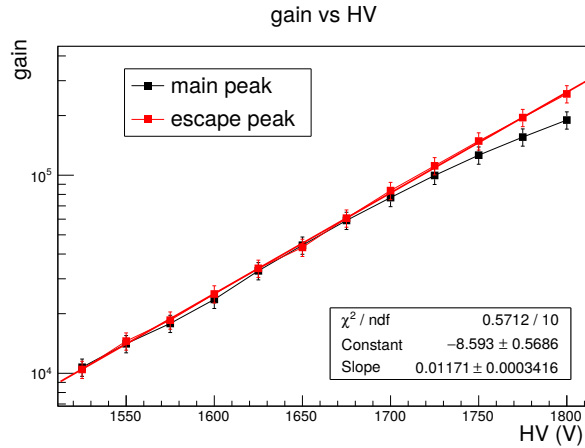


Figure 4.8: Gas amplification factor (gain). The escape peak gain curve is fitted with an exponential function. For the gain a systematic error of 10 % was assumed.

For a 70 % argon ( $W_i = 26 \text{ eV}$ ) and 30 %  $\text{CO}_2$  ( $W_i = 33 \text{ eV}$ ) mixture, we obtain a mean ionization energy of  $W_i = 0.7 \cdot 26 \text{ eV} + 0.3 \cdot 33 \text{ eV} = 28.1 \text{ eV}$ <sup>10</sup>. Hence, the main peak energy of 5.9 keV produces  $n_T = 210.0$  charges, while the escape peak energy is sufficient to produce  $n_T = 96.1$  charges. By normalizing the measured charges to the ionization charge before the gas amplification, one obtains the gas amplification gain, which is graphed in figure 4.8. As expected for a proportional counter, the gain curves of both peaks are nearly identical. Above 1700 V, however, the charge of the full photon ionization (main peak) undergoes less gas amplification than the charge of the alternative ionization process (resulting in the escape peak). The charge amplification process becomes non-linear not only above a certain high voltage, but also above a certain amount of total ionization. This behavior is interpreted as a local saturation effect of the avalanche gas amplification process due to space charge effects (see section 2.3.5). From this measurement it can be stated that at least for charges between 200 fC and 2 pC, the calibrated PASTTREC charge measurement can be considered linear within a relative margin of 10 %. The gain curves follow an exponential function. Fitting the unsaturated gain curve of the escape peak with an exponential leads to an empirical formula for the gas amplification factor  $G$  in an MDC I cell for the given gas mixture:

$$G = \exp(-8.6 + 0.0117 \cdot U_{HV}[\text{V}]). \quad (110)$$

At the high voltage working point of 1750 V, used during the beam test and the cosmic muon measurement, the formula yields a gain of  $1.4 \times 10^5$ .

Lastly we consider the relative charge measurement precision, which is calculated as the Gaussian width of the respective charge peak divided by the peak's mean charge. As shown in figure 4.9, the charge precision measured via the main peak is relatively constant around 13 %. Only for the lowest high voltage setting, corresponding to a charge of 370 fC, the precision degrades to circa 18 %. Via the escape peak, a charge precision of better than 30 % could be observed, which even reaches 19 % to 25 % below 1 pC. When taking a closer look at the charge spectra (appendix, section A.3), one observes, that for the lower high voltage settings, both the main and the escape peak are distinct features of the spectrum. For operating voltages starting at around 1700 V, both peaks are more and more overlapping as a consequence of the saturation of the gas amplification. Due to

<sup>10</sup>The weighted average of the gas mixture ionization energies is a simplified estimate, neglecting the microscopic interaction cross sections.

the higher statistics the main peak remains a clear feature of the spectrum and its width is correctly estimated, while the fit tends to overestimate the width of the less distinct escape peak.

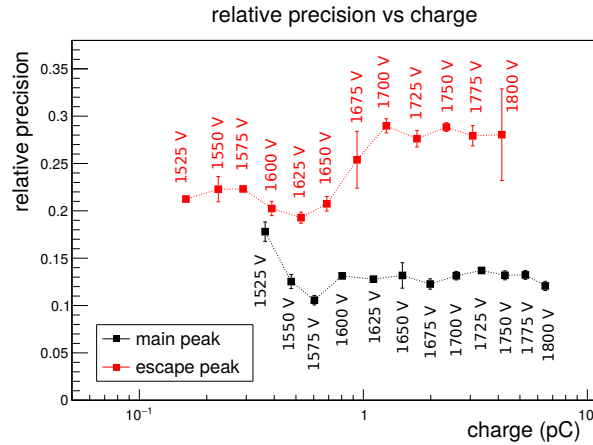


Figure 4.9: Relative charge measurement precision with PASTTREC, calculated as Gaussian peak width divided by peak charge.

#### 4.4 Charge measurement of minimum ionizing particles with PASTTREC

In the following, the charge calibration function recorded for PASTTREC is applied to the time over threshold data recorded during the beam test with minimum ionizing protons. In particular we want to measure the typical total pulse charge (after amplification) caused by a minimum ionizing particle at a typical high voltage working point of the detector. Furthermore, the influence of the track position relative to the sense wire on the measured  $ToT$  is of interest.

As discussed in section 2.2, charged particles of a fixed energy have a statistical energy loss in matter which is distributed according to a Landau distribution. A calibrated charge spectrum recorded for minimum ionizing tracks at a distance of 1.3 mm from the sense wire is shown in figure 4.10. Using the theoretical knowledge, the measured charge distribution is fitted with a Landau function (green graph). In addition, the distribution is fitted with a Langaus (red graph) function which is the convolution of a Landau function with a Gaussian, which accounts for a certain amount of measurement uncertainty. It can be observed, that the Langaus fit matches the measured charge spectrum better than a pure Landau fit.

A characteristic parameter of the Landau and the Langaus function is the most probable value (MPV). Figure 4.11 shows the dependence of the MPV when the track distance to the sense wire is varied. The entirety of the analyzed charge spectra underlying the plot are attached in the appendix, section A.4. Fitting the plots with a symmetric 8<sup>th</sup> order polynomial confirms the spatial symmetry of the data, which in turn reflects the physical symmetry of the detector cell. The observed “W”-shape resembles the time measurement precision derived from the very same data (see section 3.3.8). The discrepancy between the two fit methods can be interpreted as a systematic error margin.

Due to the fact that the drift cell has the same thickness at any position, the actual energy loss of the minimum ionizing particles cannot depend on the distance of the track from the sense wire. However, the reconstructed charge does. Unlike the ionization

#### 4.4 Charge measurement of minimum ionizing particles with PASTTREC

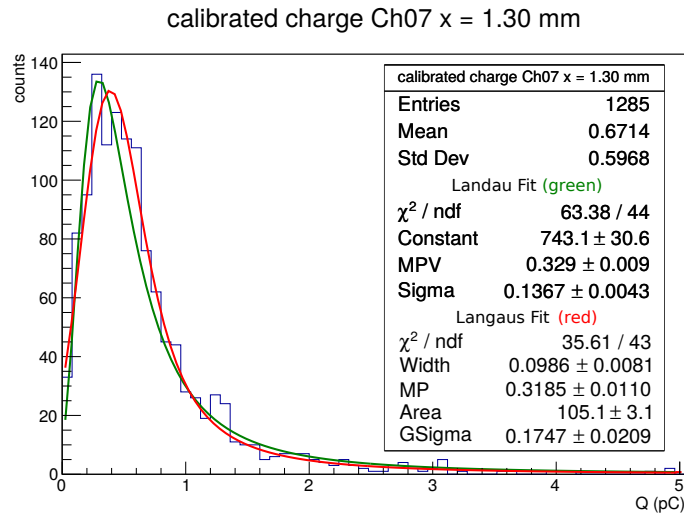


Figure 4.10: Charge spectrum of minimum ionizing proton tracks with a distance of 1.3 mm from the sense wire. The distribution is fitted with a Langaus function and with a pure Landau function for comparison.

caused by X-ray photons, the ionization from particle tracks are spatially extended. Therefore, when undergoing a drift motion in the electric field, not all ionization electrons arrive at the sense wire at the same time. Depending on the position of the particle track within the cell, the resulting detector signal shape, and thus the measured time over threshold, can differ, even though the underlying amount of charge is identical. For the inner  $-2$  mm to  $2$  mm of the MDC I cell, the most probable measured charge is  $350$  fC with a position dependent variation of circa  $20\%$ .

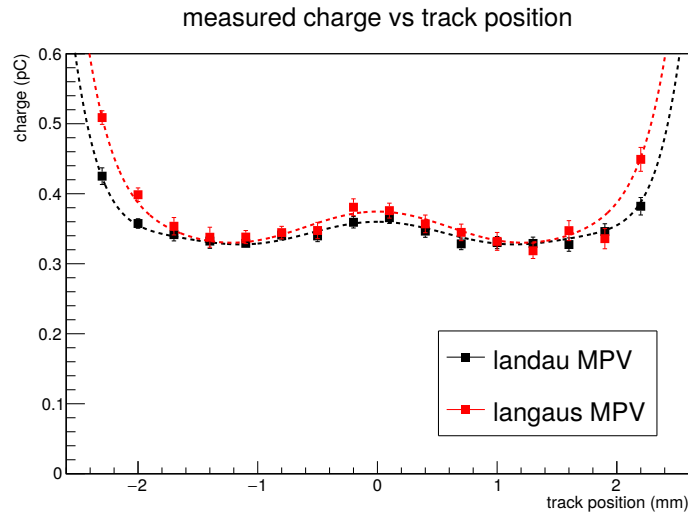


Figure 4.11: Most probable value of Landau/Langaus distribution as a function of track distance to sense wire, derived from charge spectra recorded with PASTTREC. Both plots are interpolated with a symmetric  $8^{th}$  order polynomial.

## 4 Measuring energy loss



## 5 Simulation

The operation of gas detectors, especially wire chambers is well understood. Applying this knowledge, however, is not trivial since many different mechanisms come to play simultaneously. To understand a specific type of wire chamber quantitatively a numerical simulation is very useful.

GARFIELD [GAR] is a simulation framework for gaseous detectors developed at CERN. It provides an interface to HEED, a program to simulate ionization in gasses due to charged particles, as well as an interface to MAGBOLTZ [MAG], a program to calculate the drift of electrons in arbitrary gas mixtures and electric and magnetic fields. An additional interface is provided to neBEM, a program able to calculate fields and potentials for nearly arbitrary three dimensional electrode and dielectric geometries [NEB]. Based on the exact wire geometry, the wire radii, the applied high voltage and the gas mixture, one or more HADES MDC cells can be simulated using GARFIELD. This allows understanding the exact shape of the drift field as well as studying the statistical time of arrival distributions of the individual ionization electrons at the sense wire. The latter is crucial for understanding the electrical signal of the chamber as well as the characteristic shape of the  $t_1$  measurement precision. The HADES MDC cells were simulated in GARFIELD before [Mar05]. However, due to the unavailability of the three dimensional field solving capabilities of neBEM in the past, only approximated two dimensional cross sections of an MDC cell could be calculated. Therefore the sense/field wires and the cathode wires were aligned in the same direction, while in reality the wire planes cross each other at angles of  $90 \pm 0^\circ$ ,  $90 \pm 20^\circ$  or  $90 \pm 40^\circ$ .

### 5.1 Cell geometry

In the following we focus on the simulation of a  $0^\circ$  MDC I cell, the same wire geometry that was used in the cosmic tracking set-up and the beam test. In this geometry, the cathode wires and the sense/field wires are arranged at a  $90^\circ$  relative (stereo) angle. In MDC I, the sense/field wire pitch is 2.5 mm, the cathode wire pitch is 2 mm and the distance between neighboring wire planes is again 2.5 mm. Consequently cross sections through MDC I cells are squares. Cathode and field wires have a diameter of  $80 \mu\text{m}$ , sense wires have a diameter of  $20 \mu\text{m}$ . A section of such a cell is shown in figure 5.1. For a consistent coordinate system for the simulation the following convention is chosen:

- The x-axis is chosen parallel to the sense wire.
- The y-axis is chosen parallel to the cathode wires.
- The z-axis is perpendicular to the wire planes, parallel to straight impinging particle tracks (beam axis of beam test).
- The sense wire is located at  $y = 0$ ,  $z = 0$ .
- Cathode wires are located at  $x = \pm 1 \text{ mm}$ ,  $x = \pm 3 \text{ mm}$ ,  $x = \pm 5 \text{ mm}$ , etc. ...

### 5.2 Field geometry

The electrode geometry of a HADES drift drift cell produces a unique electric field, which exerts the electrical force determining the ionization electron drift to the sense wire. For understanding the electric potential and the electric field, we study cross sections

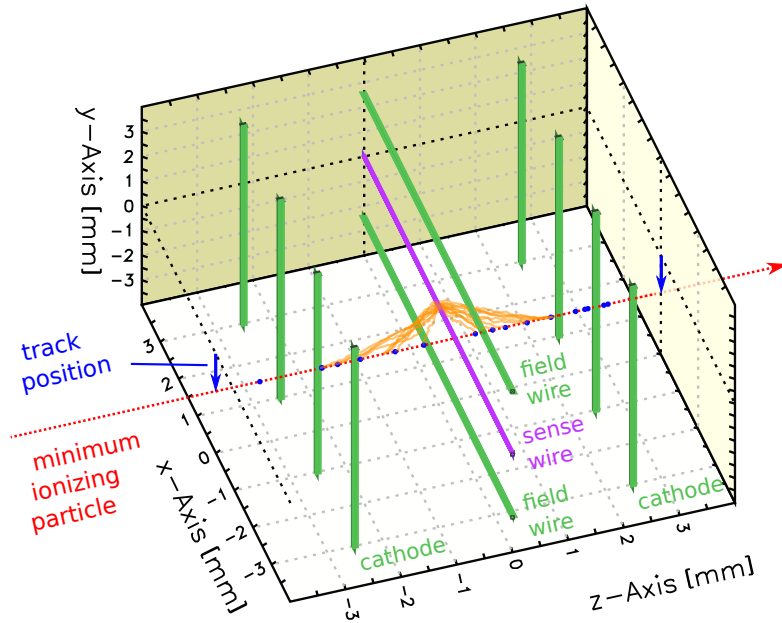
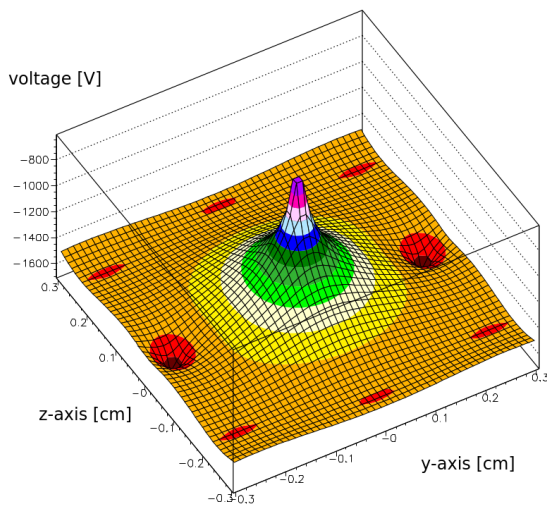


Figure 5.1: 3D view of a simulated minimum ionizing particle track and electron drift to the sense wire of a MDC I drift cell, generated in GARFIELD[GAR].

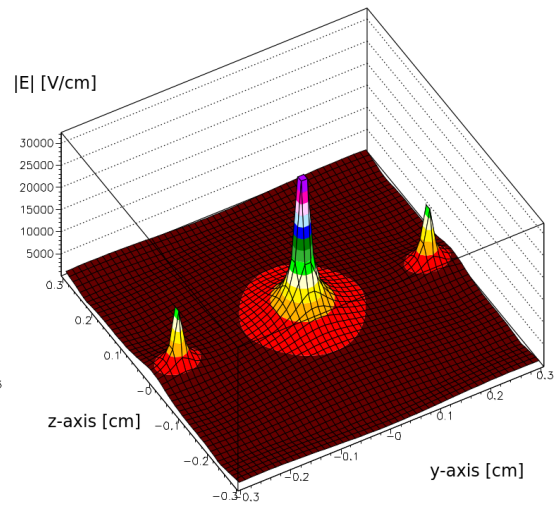
of the MDC cell. The two most distinctive cases are the cross section at  $x = 0$  and at  $x = \pm 1$  mm, i.e. cutting the cell in the middle between two cathode wires and cutting directly on the cathode wires. Surface plots of both, the potential and the absolute of the electric field for  $x = 0$  and  $x = \pm 1$  mm are presented in figure 5.2. All other cross sections have potential/field values in between the abovementioned extreme cases. In the simulation, the sense wire is set to a potential of 0 V, while the cathode wires and field wires are set to  $-1750$  V, analog to the operation high voltage used in the cosmic muon set-up and the beam test set-up.

To consider the two-dimensional cross sections more quantitatively, we study one-dimensional graphs of the potential and the total electric field strength along the y- and z-axis of the quadratic cross sections, as well as on the yz diagonal (see figures 5.3, 5.4 and 5.5). Apart from the cross sections at  $x = 0$  and  $x = \pm 1$  mm, an additional intermediate position at  $x = \pm 0.5$  mm is also evaluated.

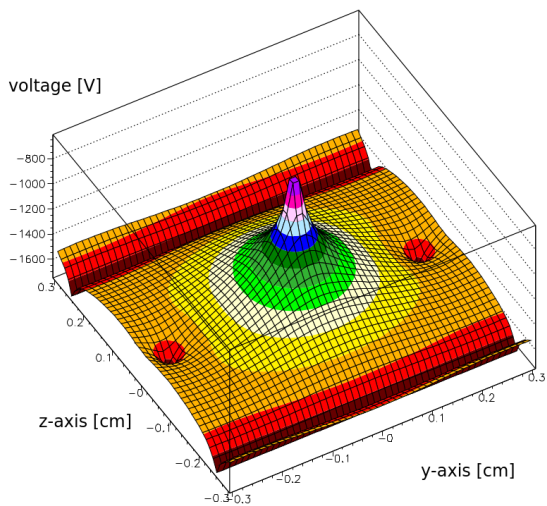
Although the electric field is the derivative of the potential ( $\vec{E} = -\nabla\varphi$ ), this does not necessarily mean, that the 1D cut of the field is the derivative of the 1D cut of the potential. This is only true if the electric field is oriented parallel to the 1D cut, which is the case for the center part of the cell because all field lines emerge from the sense wire. In the outer areas of the cell, however, the electric field does not need to point directly towards the sense wire. It is observed, that potential and field on the y-axis does not depend on the x position of the cross section, while the most drastic x dependence is seen along the z-axis. Further it can be observed, that between the cathodes ( $x = 0$ ) there are areas where the absolute of the electric field approaches zero. Since there is no or only little acceleration towards the sense wire, ionization created in the vicinity of these regions might not contribute at all to the detector output signal or only with a drastic delay.



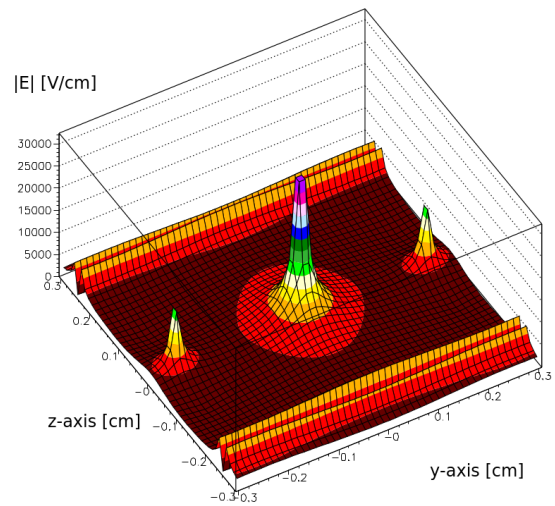
(a) Potential at  $x = 0$  (between cathodes).



(b) Field at  $x = 0$  (between cathodes).



(c) Potential at  $x = \pm 1$  mm (on cathodes).



(d) Field at  $x = \pm 1$  mm (on cathodes).

Figure 5.2: Electrical potential and electrical field strength for MDC I cross sections.

## 5 Simulation

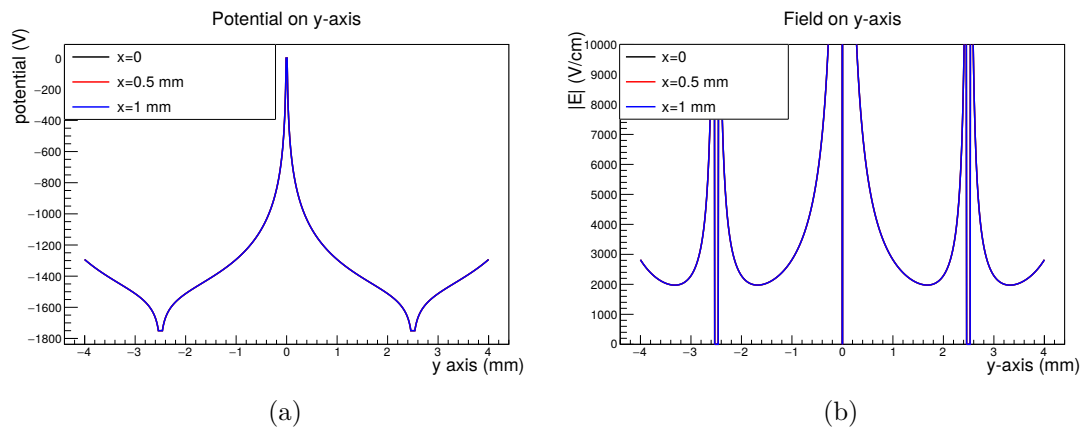


Figure 5.3: Potential (a) and electrical field (b) on y-axis of cell cross section at  $x = 0$  mm,  $\pm 0.5$  mm,  $\pm 1$  mm.

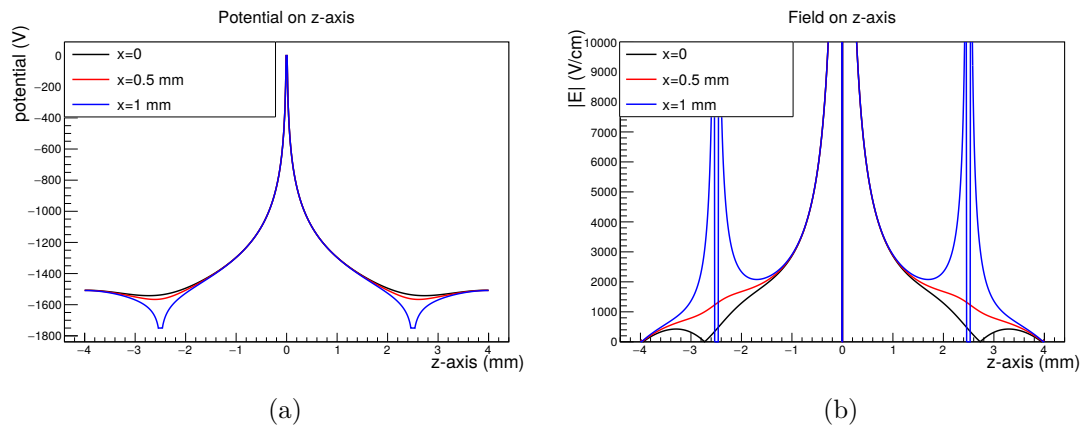


Figure 5.4: Potential (a) and electrical field (b) on z-axis of cell cross section at  $x = 0$  mm,  $\pm 0.5$  mm,  $\pm 1$  mm.

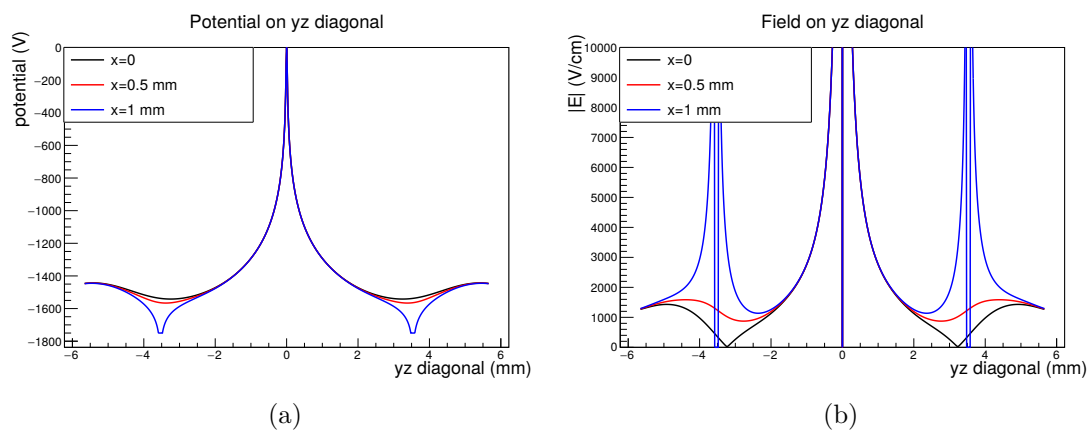


Figure 5.5: Potential (a) and electrical field (b) on yz diagonal of cell cross section at  $x = 0$  mm,  $\pm 0.5$  mm,  $\pm 1$  mm.

### 5.3 Electron drift velocity

Knowing the gas mixture, in our case 70 % Ar, 30 % CO<sub>2</sub>, GARFIELD is able to use MAGBOLTZ to calculate the effective properties of the gas. The effective electron drift velocity is calculated and plotted along the same one-dimensional cuts previously used to study the potential and the field, i.e. on the y-axis, the z-axis and the yz diagonal of cross sections through the cell in the middle between two cathode wires ( $x = 0$ ), on a cathode wire ( $x = \pm 1$  mm) and for one intermediate step ( $x = \pm 0.5$  mm). The results are shown in figure 5.6.

Obviously, the drift velocity is not constant over the cell. Especially in the middle between two cathode wires ( $x = 0$ ) the drift velocity drastically drops in z direction and towards the diagonal corners of the cell. At a distance of 1.25 mm from the sense wire, the simulation results yield an electron drift velocity of  $66 \mu\text{m ns}^{-1}$ , which is consistent with the experimentally measured drift velocity, assessed during the beam test (see section 3.3.8). Up to a radius of 1.25 mm, the drift velocity is a mere function of the radial distance from the sense wire (within a relative margin of 3 %), i.e. it is independent of the x position of the cross section and identical in y, z and diagonal direction. Beyond this radius, the drift velocity is more and more dominated by the field inhomogeneities of the wire geometry.

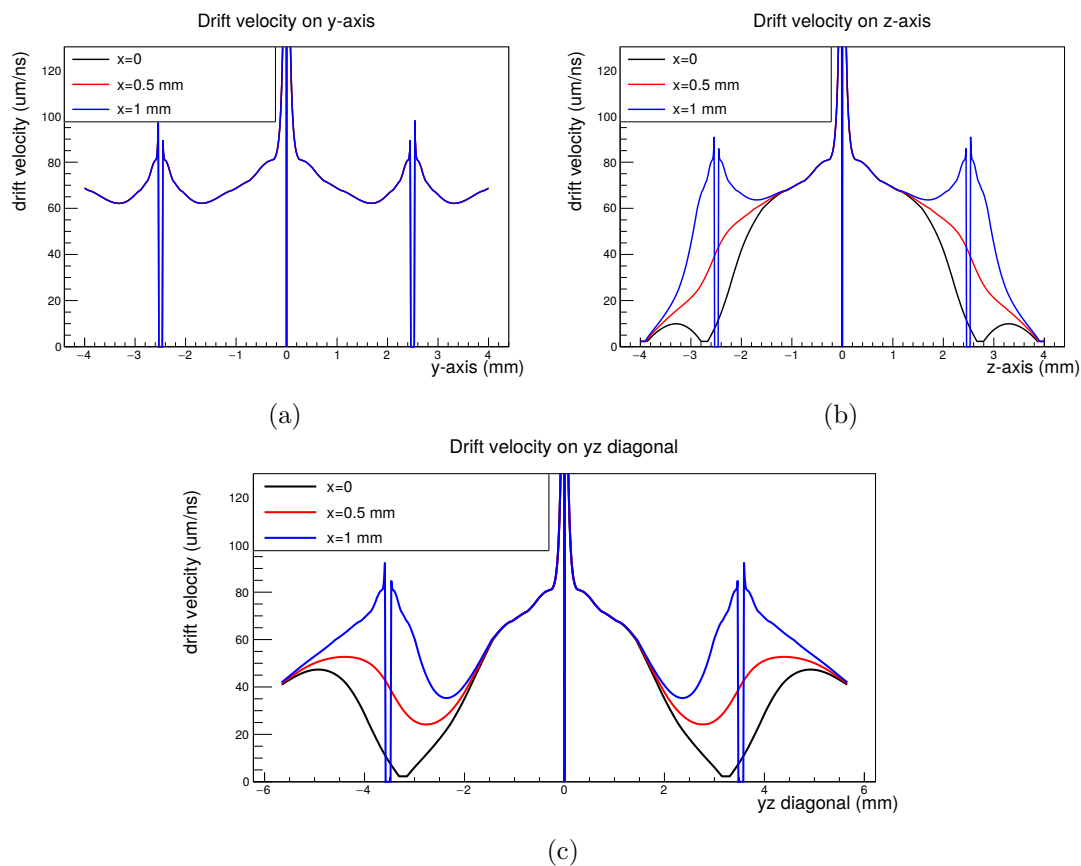


Figure 5.6: Simulated drift velocity in MDC I cell on the y-axis (a), z-axis (b) and yz diagonal (c) of cell cross section at  $x = 0$  mm,  $\pm 0.5$  mm,  $\pm 1$  mm. Sense wire at 0 V, cathode and field wires at  $-1750$  V, gas mixture 70 % Ar, 30 % CO<sub>2</sub>.

#### 5.4 Simulation of the beam test

In the following, GARFIELD is used to re-enact the beam test measurements in simulation. Therefore in total  $6 \times 10^5$  straight proton tracks (parallel to the z-axis) with a kinetic energy of 1.93 GeV are generated and distributed uniformly in y and x direction over the simulated cell. GARFIELD uses the HEED subprogram to simulate statistically distributed ionization clusters along the track, and MAGBOLTZ to calculate the drift trajectories of the ionization electrons from their point of creation to the sense wire via a Monte Carlo method. An example track is shown in figure 5.1.

The desired output of the simulation for further analysis is the drift time of each individual ionization electron, i.e. the time of arrival at the sense wire, given the ionization was created at  $t = 0$ . The drift time distribution of the entirety of the created ionization electrons is shown in figure 5.7. The two-dimensional histogram graphs the distribution for all possible y track positions. For a more quantitative study, we regard four exemplary cases, namely  $y = 0$ ,  $y = 0.5$  mm,  $y = 1.25$  mm,  $y = 2.0$  mm, which are shown in figure 5.8. In all cases, the resulting drift time distribution has a steep rise, a main “body” and a long tail. The position of the rise is obviously directly related to the distance from the sense wire and is determined by the fastest arriving electrons. All but the  $y = 0$  distribution feature a peak directly ensuing the initial rise. This can be explained geometrically: The greater the distance between sense wire and the linear extended ionization, the more ionization electrons can arrive at the same time. This is because the path to the sense wire, though it becomes longer, becomes more similar in length. It is observed, that while the total amount of arriving electrons is comparable in all cases, the time of arrival peak is most prominent around  $y = 1.25$  mm, i.e. at half the distance between sense wire and field wire. Though the above geometrical argument would favor an even more distinct peak for even greater y values, the inhomogeneities in the drift field and the increasing effect of electron diffusion counteract this effect. A small onsetting tail is also observed prior to the steep rise. This phenomenon is explained by the not unfrequent creation of delta electrons during the primary ionization of the gas. Those high energy electrons, when randomly passing close to the sense wire, are themselves capable of creating ionization electrons, which have a shorter drift time than the electrons originating from the actual particle track.

For a given particle track, the ionization electron which is closest to the sense wire will also be the first to arrive at the sense wire (when neglecting diffusion). Therefore the drift time of the first arriving electron will also have the closest correlation to the track position. The second, third and all later arriving electrons will carry less and less precise spatial information about the particle track. This is illustrated in figure 5.9, where the drift time distribution of the  $n^{th}$  electron is shown versus the track position. It is clearly visible, that for the first electron, there is a sharp, nearly linear correlation between drift time and track position. For all following electrons, the correlation has a similar but increasingly blurred shape.

The relevant read-out electronics covered in this thesis are of type amplifier-shaper-discriminator. As discussed in section 3.1, the shaper acts as an integrator, or figuratively spoken, a “counter” of electrons. To exceed a certain fixed discriminator threshold, the combined, i.e. integrated signal contributions of more than one incoming electron is usually required. While the ideal read-out electronics would register the first arriving electron, in the non-ideal case, depending on the applied threshold setting, the electronics are sensitive to the arrival of the  $n^{th}$  electron.

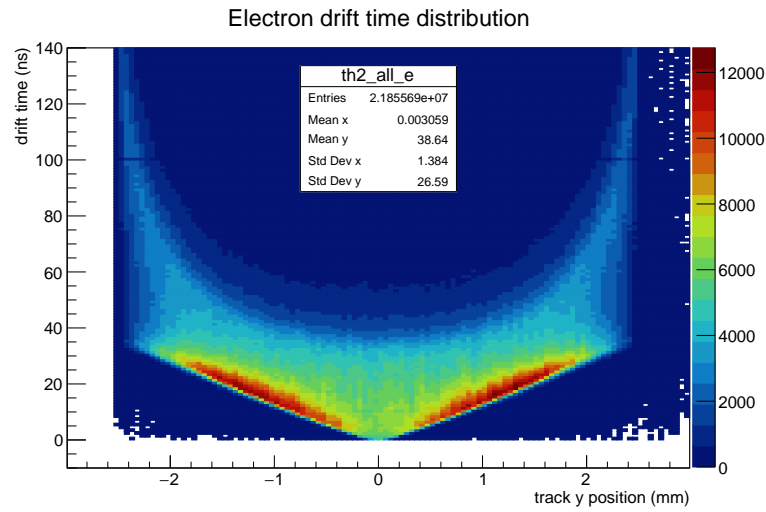


Figure 5.7: Ionization electron drift time distribution of  $6 \times 10^5$  straight minimum ionizing proton tracks, plotted versus track y position.

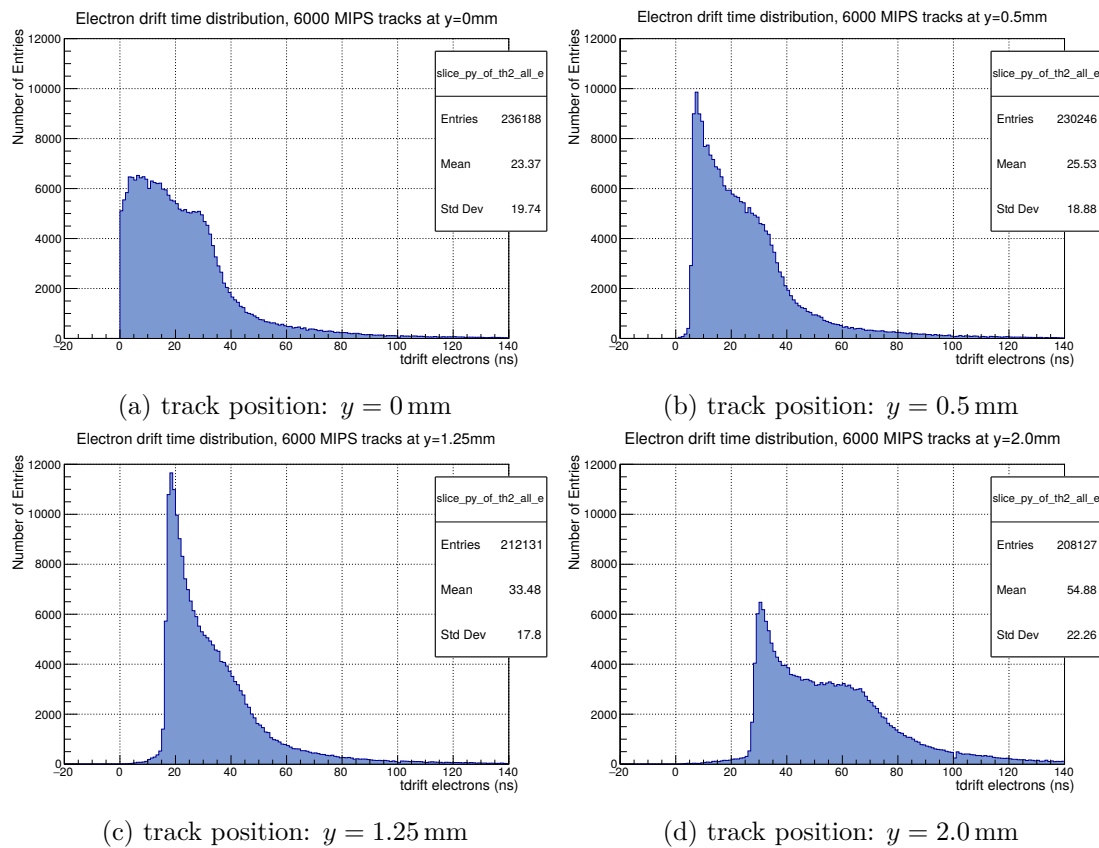


Figure 5.8: Drift time distributions of ionization electrons for straight MIPS tracks at selected distances from the sense wire. Each graph contains the combined statistics of 6000 individual minimum ionizing proton tracks.

## 5 Simulation

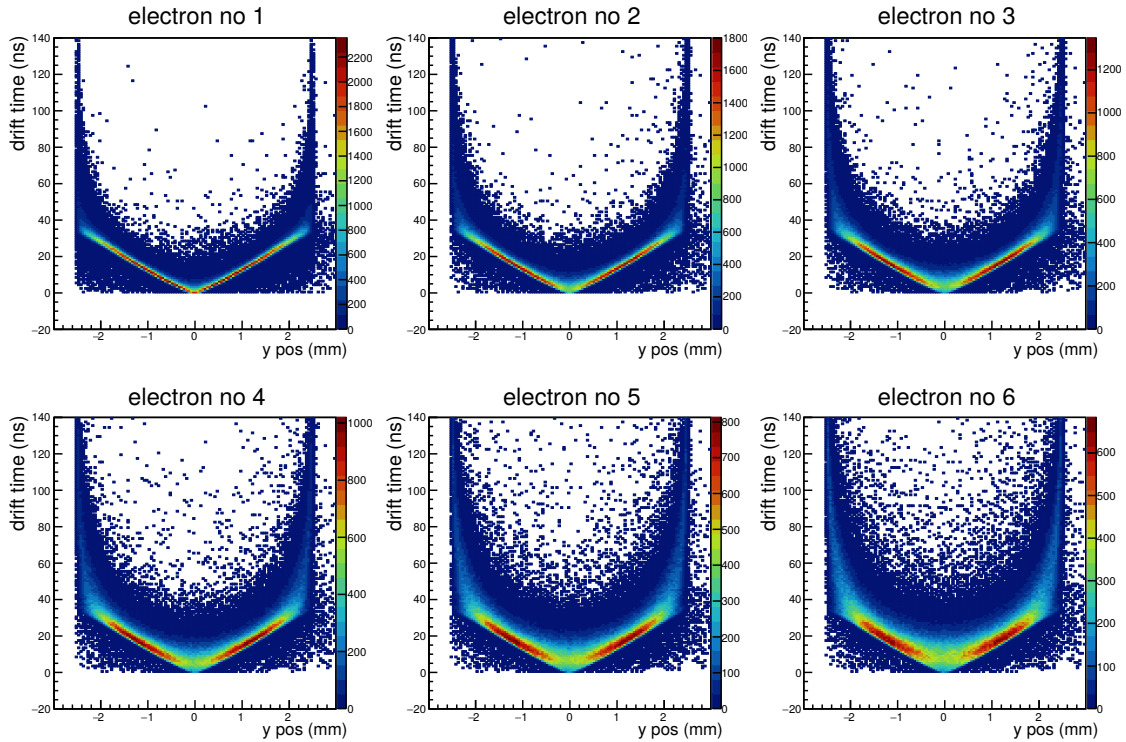


Figure 5.9: Drift time distribution of the first, second, ..., sixth electron arriving at the sense wire versus track y position.

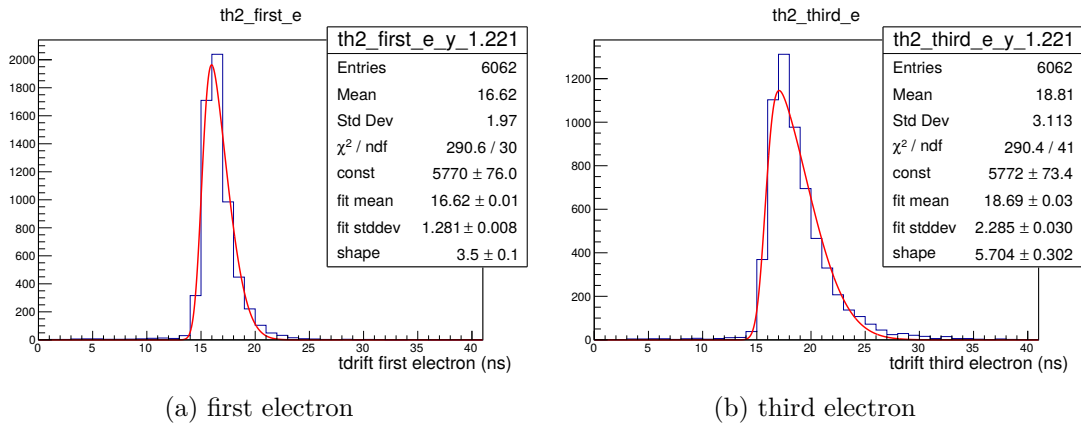


Figure 5.10: Exemplary drift time distribution for the first and the third arriving electron. Statistics from 6000 MIPS tracks at  $y = 1.25$  mm. The distributions are fitted with a skew normal distribution.



When regarding the simulated drift time distribution of the  $n^{\text{th}}$  arriving electron for a fixed position, one can observe, that the individual distributions are not symmetrical, but skewed. This is shown exemplarily in figure 5.10 for the first and third arriving electron at  $y = 1.25$  mm. For feature extraction and further analysis, the individual  $n^{\text{th}}$  electron distributions are fitted with a skew normal distribution (see appendix, section A.2). The parameters of interest are the mean and the standard deviation of the fit function. Finally, figure 5.11 combines all extracted parameters for all simulated  $y$  slices. For each  $n^{\text{th}}$  electron one obtains a space-time relation and the intrinsic time precision as a function of track position.

According to the simulation, a time precision of better than 2 ns is possible for the innermost  $\pm 2$  mm of the cell, given one is able to discriminate the first arriving electron. The individual  $n^{\text{th}}$  electron precision curves have a distinct “W” shape due to the fact that the best time precision is achieved in the middle between sense and field wire. The best time precision for the  $n^{\text{th}}$  electron coincides with the most prominent leading peak in the total electron drift time distribution (figure 5.8). It is comprehensible that if many electrons from the same track arrive in relative coincidence, the width of the  $n^{\text{th}}$  electron’s arrival time distribution is narrowed. Figuratively spoken: If the  $n^{\text{th}}$  electron is too late, due to the abundance of electrons, it simply becomes the  $(n + 1)^{\text{th}}$ , and another faster electron takes its place.

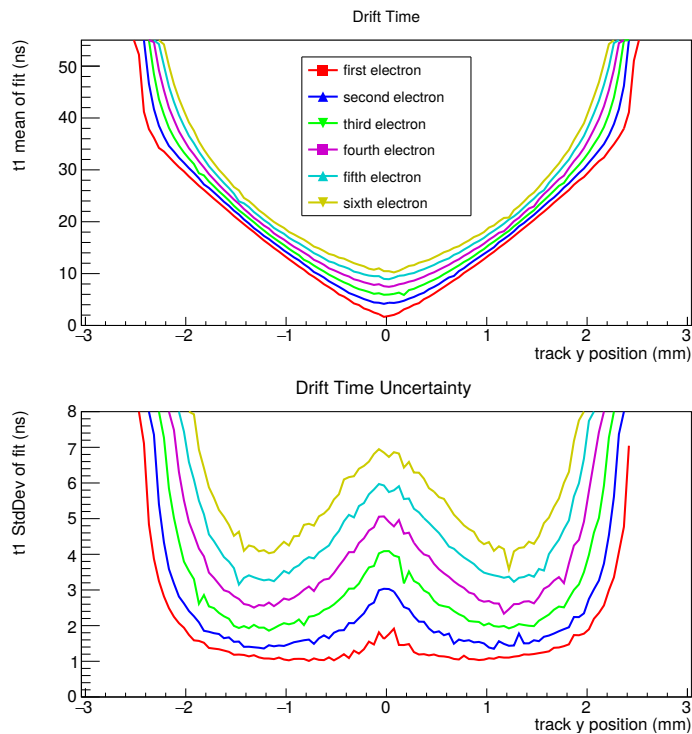


Figure 5.11: Drift time (space-time relation) and drift time uncertainty (time precision) for the first six arriving electrons.

## 5.5 Comparison to experimental beam test data

In the following we want to use the simulation results to qualitatively and quantitatively interpret the detector and electronics performance results assessed during the beam test.

The simulation is able to produce a “V” shape for the drift time and a “W” shape for the time precision (drift time uncertainty) vs track position which are very similar to the direct measurement results of the beam test (see section 3.3.8, figure 3.40). In both cases, simulation and measurement, the best time precision is achieved at half the distance between sense and field wire. Nevertheless, the simulated and the measured time precision, when overlaid, do not align, since the valleys of the measured “W” shape are less deep than the simulated ones. Still, the simulation only calculates uncertainties due to primary ionization statistics and electron diffusion. It does not take account of the shape of the analog signal and any form of electronic noise affecting it.

In order to emulate additional sources of noise, the simulation is repeated and the drift time distribution for each  $n^{\text{th}}$  electron is broadened by adding a Gaussian jitter. Obeying the laws of quadratic Gaussian error propagation, the additional uncertainty affects predominantly the valleys of the “W” shape, effectively raising them and flattening them out. For an additional RMS jitter of 2 ns, the simulated precision curves of the third and fourth electron reproduce well the shape of the precisions measured with ASD-8 and PASTTREC during the beam test (see figure 5.12), thus one is inclined to assume that with the chosen threshold settings ASD-8 is able to react to the third electron, while PASTTREC reacts to the fourth. The simulated space-time relations, i.e. the mean drift times extracted via the skew normal fits, remain practically unaffected by the additional jitter.

The experimentally measured drift times are subject to an unknown systematic offset, due to unknown delays in the cabling and the signal processing electronics. Thus, in figure 5.12, the measured data points are shifted in y direction to align best with the space-time relation for the third (ASD-8) and fourth (PASTTREC) arriving electron, according to the above assumption. Though the measured and the simulated space-time relations are very similar, the measured “V” shape is less acute in the center. There, the discrepancy is about 1.5 ns. An exemplary comparison of the measured  $t_1$  distribution (ASD-8, threshold 1.26 V) and the simulated drift time distribution (third electron + jitter) is displayed in figure 5.13. Apart from the small Gaussian background pedestal, which we allow for the measured data, the distributions are very similar.

If the simulated proton track is extended to not pass through a single cell only, but through a semi-overlapping cell pair, self-tracking can be simulated. The self-tracking method, used in both, the cosmic muon set-up and the beam test set-up, is explained in section 3.2.3. The characteristic shape of the self-tracking drift time correlations, which are observed in both experimental set-ups can be reproduced. With the additional Gaussian jitter of 2 ns the simulated self-tracking correlation of the third arriving electrons in both cells bears strong resemblance to its real world counterpart measured with ASD-8 during the beam test. The full correlation plot and the projection of its center ( $T_a + T_b$  distribution for  $|T_a - T_b| < 10$  ns) is shown in figure 5.14 and figure 5.15. When the  $T_a + T_b$  distributions are fitted with a skew normal distribution (allowing a small Gaussian pedestal for the experimental data), the standard deviation and the shape parameter of the skew normal fit are identical within the fit errors.

## 5.5 Comparison to experimental beam test data

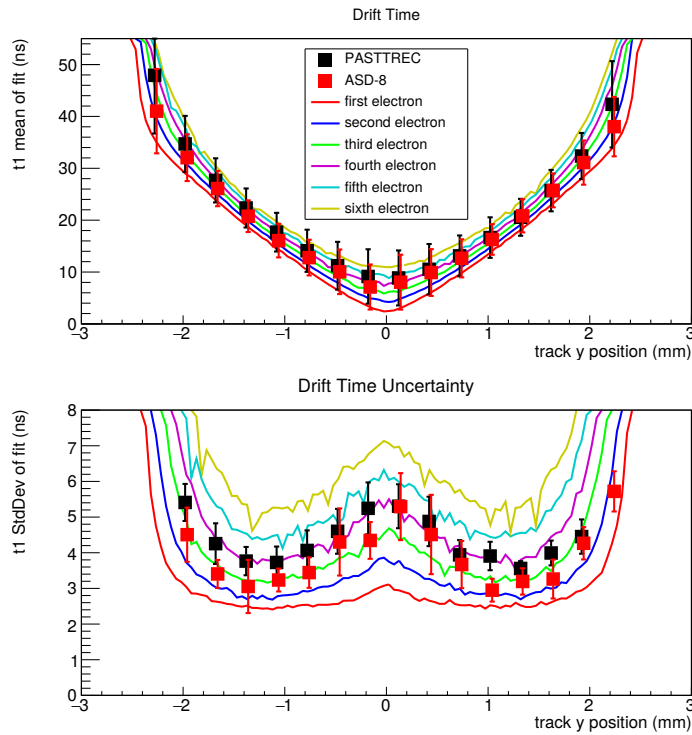


Figure 5.12: Comparison of GARFIELD simulation and the data measured at the beam test. The shape of the uncertainty curve is matched by the simulation by adding an artificial Gaussian jitter with a standard deviation of 2 ns to all simulated drift times.

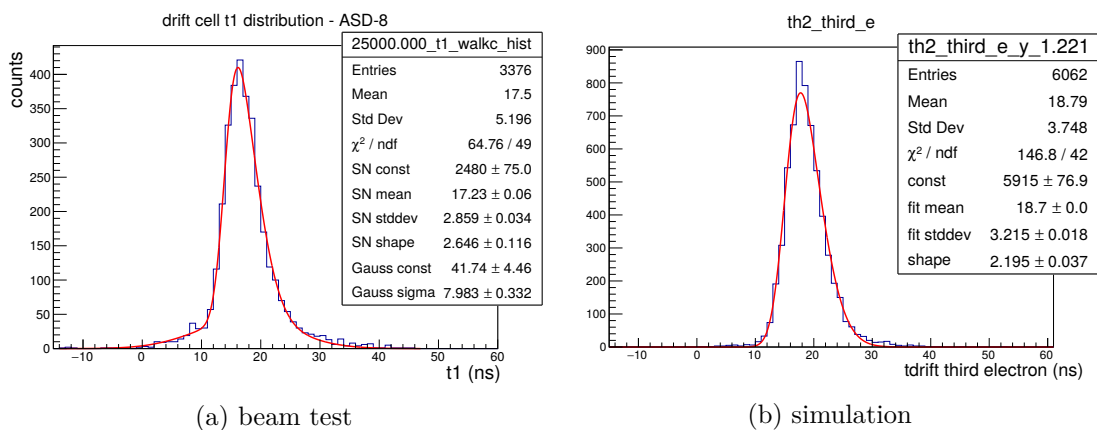


Figure 5.13:  $t_1$  distribution at  $y = 1.25$  mm measured with ASD-8, threshold 1.26 V (a) compared to simulated  $t_1$  distribution of third arriving electron, broadened by Gaussian jitter of 2 ns (b).

## 5 Simulation

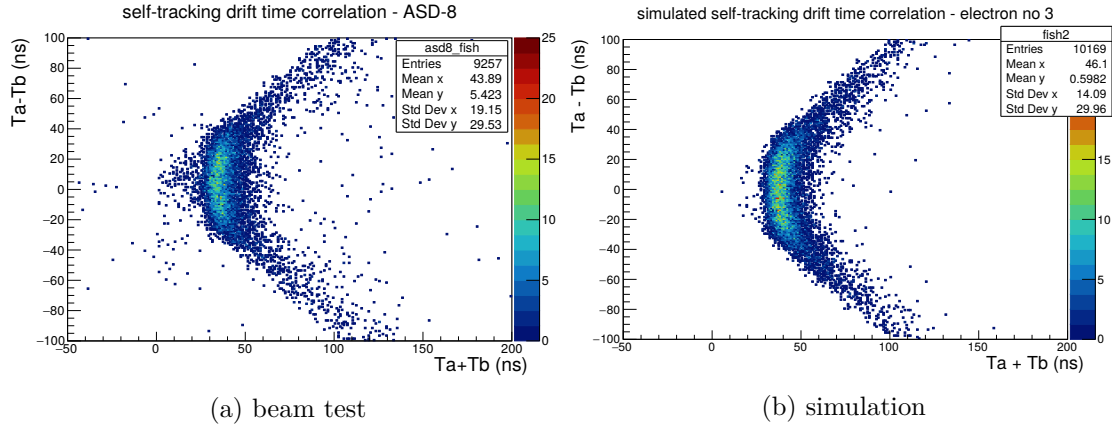


Figure 5.14: Comparison of the self-tracking drift time correlations of beam test experimental data (ASD-8, threshold 1.26 V, trigger on full diamond) and simulated data (third arriving electron + 2 ns RMS jitter).

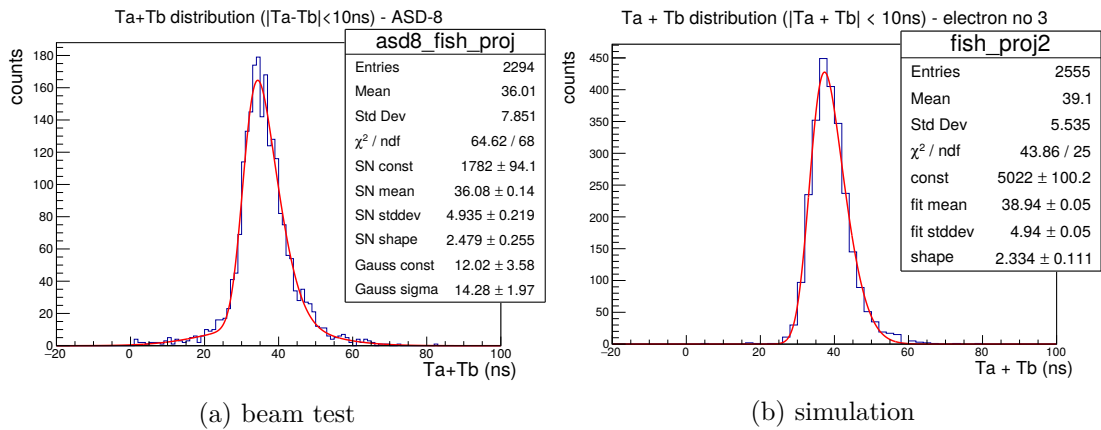


Figure 5.15: Drift time sum distribution for  $|T_a - T_b| < 10$  ns and skew normal fit of beam test experimental data (ASD-8, threshold 1.26 V, trigger on full diamond) and simulated data (third arriving electron + 2 ns RMS jitter).

## 6 Summary and outlook

The main objective of this thesis was the evaluation of the PASTTREC ASIC as a potential replacement for the ASD-8 ASIC in the next version of the HADES MDC front-end electronics.

Prior to dedicated tests to assess the performance of both ASICs with a HADES drift chamber, a detailed understanding of the analog input signal is necessary. Therefore, the raw signal of an MDC I cell was sampled and recreated in a circuit simulation model. The model yields an excellent description of the long term time development of the accumulated detector charge signal, i.e. ranging up to few microseconds. A quantitative understanding of the latter is important for a correct charge measurement calibration since a non-negligible fraction of a drift chamber pulse is contained in its tail, extending far longer than the effective charge integration times of the read-out circuits, which are in the range of 10 ns. The attempt to model the MDC current signal on short timescales ( $\approx 0$  ns to 100 ns) reveals that the cell is best described as a transmission line (coaxial cable) instead of a simple capacitor. Further, the model can only describe the pulse shape correctly when the non-negligible flex print cable capacitance is taken into account. The MDC pulse model signal was fed into a high level circuit simulation of the PASTTREC shaper, which provides a tangible demonstration of the individual analog signal processing stages. Conceptually, the analog signal chain is comparable to ASD-8, although ASD-8 has slightly different operation parameters.

Two versions of read-out electronics, the current ASD-8 based analog read-out card and a prototype analog front-end with the PASTTREC ASIC were tested in direct comparison in two different set-ups assessing the time precision. The cosmic muon tracking set-up allowed for assessing the detector time precision at mid-distance between sense wire and the field wire via the self-tracking method. The minimum ionizing proton beam set-up allowed for both, applying the self-tracking method as well as a direct measurement of the drift time precision for perpendicular tracks at any distance from the sense wire. To extract the desired features from the recorded drift time distributions, i.e. mean drift time and drift time uncertainty, the respective distributions are fitted with the probability density function of a skew normal distribution while allowing for a small Gaussian background. The beam test results via both methods are consistent within their systematic errors. The best time precision is measured at mid-distance between sense and field wire, i.e. the location in the cell accessed by the self-tracking method. Consequently, the time precision as a function of the track position has a “W” shape, when scanning over the width of an entire cell. Further, the space-time relation of the drift cell can be measured with both ASICs with comparable results. While in the cosmic set-up PASTTREC was operated with non-optimal ASIC settings (gain, shaper settings, threshold), the beam test allowed for parameter scans resulting in significantly better performing settings. The PASTTREC performance was further improved by applying a walk correction on basis of the measured time over threshold values. With the new settings and walk correction, PASTTREC only falls short of the ASD-8 time precision by approximately 20 % (3.6 ns vs 3.0 ns at half distance between field and sense wire). Comparing beam test and cosmic muon results, one has to notice that the cosmic set-up yields a systematically better time precision, especially for PASTTREC. This effect is attributed to the approximately 37 % higher charge in the primary ionization traces because cosmic muons are not minimum ionizing particles and impinge at a non-perpendicular angle, leading to a longer path length inside the active detector volume. The resulting larger average signal is expected to produce less jitter after the

discriminator. After all, a performance assessment with minimum ionizing particles is desired to cover the most challenging case of tracking particles. Therefore the beam test results are to be treated as more relevant than the cosmic muon results. However, the latter can be regarded as a consistency check of the employed methods. In both set-ups the PASTTREC prototype board proved to operate more stable than the ASD-8 based hardware, despite the lack of a differential signal input. PASTTREC showed a far lower inclination to self-oscillation and electromagnetic pick-up noise. This results in a higher detection efficiency under typical laboratory conditions w.r.t. electromagnetic interference. From simulation and from interpolation of the measured space-time relations a drift velocity of  $66 \mu\text{m}/\text{ns}$  is deduced at the middle position between sense and field wire. Knowing the velocity, we can calculate the local spatial precision of the detector for perpendicular tracks using the direct measurement results from the beam test:

$$\begin{aligned}\sigma_x &= (3.0 \pm 0.4) \text{ ns} \cdot 66 \mu\text{m ns}^{-1} = (198 \pm 26) \mu\text{m} \text{ (ASD-8)} \\ \sigma_x &= (3.6 \pm 0.3) \text{ ns} \cdot 66 \mu\text{m ns}^{-1} = (238 \pm 20) \mu\text{m} \text{ (PASTTREC)}\end{aligned}$$

Unfortunately, the intended MDC design goal precision of  $150 \mu\text{m}$  [Mar05] is exceeded by 32% (ASD-8) and 59% (PASTTREC) at the best performing position within the drift cell. It is however not ruled out, that both read-out technologies could potentially perform better if the set-up were operated in a completely interference free environment.

Both ASICs measure charge indirectly via the time over threshold of the shaped detector signal. Employing the same ASIC settings used during the beam test, both ASICs were studied systematically with the help of an arbitrary waveform generator, programmed to mimic a drift chamber pulse including the characteristic long signal tail. Extrapolating the pulser sample with the simulated pulse model it is possible to attribute the full pulse charge to each amplitude setting of the pulser. Thus by varying the pulse amplitude, a charge calibration function can be recorded. For both ASICs and for small charges one observes a close to logarithmic dependence between the measured time over threshold and the input charge. Based on theoretical considerations, this is the expected behavior. For larger charges, the relation transitions to an approximately linear function, which is interpreted as non-linearity of the shaper circuit. From the calibration data, an upper limit of the intrinsic charge measurement precision of both ASICs was determined. With the pulser, ASD-8 is able to measure charge with a relative precision better than 8%, while PASTTREC is able to resolve the test charge to a precision better than 5%. For both ASICs, but especially for PASTTREC, the precision drastically improves for higher charges. The calibration of PASTTREC was tested for consistency using a  $^{55}\text{Fe}$  source producing defined amounts of primary ionization in a drift chamber cell. Both, the main peak and the argon escape peak of the detector signal charge spectrum, derived from PASTTREC time over threshold information, follow an exponential function of the chamber high voltage. The charge ratio between main and Ar escape peak is approximately 2 : 1, matching the theoretical assumptions. For high voltages the position of the main peak is distorted by saturation of the gas amplification process due to space charge effects.

Lastly, a three dimensional GARFIELD simulation was carried out to understand the field geometry and the drift velocity in an MDC I drift cell. It is revealed, that there exist regions in between the cathode wires, where the electric field strength and consequently the electron drift velocity approaches zero. Primary ionization deposited in or near those areas creates significantly delayed output signal components. The simulation was further used to recreate the beam test. To this end, perpendicular minimum ionizing tracks were uniformly distributed over the entire simulated cell. The simulation demonstrates, that

the drift time of the earliest arriving electron has the best correlation with track position, while all following electrons carry gradually less information. The simulated space-time relations bear a high resemblance to the space-time relations measured during the beam test. The simulation further confirms the experimental observation that the best time precision is achieved at half distance between field wire and sense wire. The simulation is able to recreate the characteristic “W” shape of the time precision as a function of track position over the width of the drift cell. Noise on the analog detector signal is roughly approximated by adding a Gaussian jitter on the arrival times of the respective  $n^{\text{th}}$  electron. With an RMS jitter of 2 ns, the simulated precision curves of the third and the fourth arriving electron describe well the precision curves measured with ASD-8 and PASTTREC during the beam test. Just as it was done with the experimental data, the mean drift time and the drift time uncertainty were extracted by fitting the simulated distributions with the probability density function of a skew normal distribution. Lastly, also the characteristic boomerang shape of the self-tracking drift time correlation was successfully recreated in simulation.

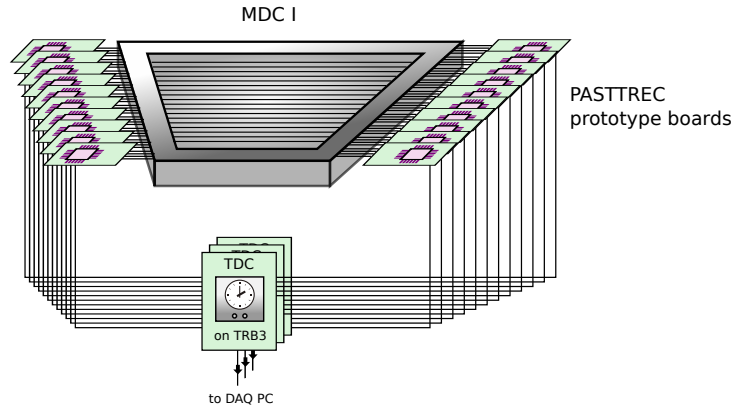


Figure 6.1: Schematic sketch of a full system test with 24 PASTTREC prototype boards.

It has been shown that PASTTREC can be operated at a HADES drift chamber with a slightly worse time precision than ASD-8. However, PASTTREC can be operated with a higher stability, and due to the longer charge integration time compared to ASD-8, it is expected to yield a better energy loss measurement precision. This work motivates the use of PASTTREC for the envisioned MDC front-end electronics upgrade. For a large detector system it is crucial that the performance achieved with small set-ups is scalable. To test the scalability of a PASTTREC based read-out, it is foreseen to conduct a so-called “full system test”, i.e. an effort to read out the two adjacent central layers of an MDC I chamber with PASTTREC only (see figure 6.1). This endeavor involves reading out 384 individual sense wires simultaneously, using 48 PASTTREC ASICs while tracking cosmic muons. In this context, the methods used in the cosmic muon set-up, as discussed in this thesis, can be employed and adapted. It is to be examined whether a large group of read-out ASICs operated in close proximity to each other and supplied via the same power network exhibits the same stability as the two PASTTREC prototype boards used in the cosmic muon set-up and the beam test set-up. Possible anticipated phenomena would involve unwanted coupling between the boards leading to oscillations and/or crosstalk. Furthermore systematic studies need to be carried out to investigate the channel-to-channel offsets when a common threshold is applied and how these can be mitigated by using the per-channel baseline correction setting of PASTTREC.

## 7 Zusammenfassung

### Einführung

Das HADES-Experiment (High Acceptance DiElectron Spectrometer), welches sich an der GSI befindet, ist ein Mehrzweck-Detektor für die Präzisionsspektroskopie von Elektron/Positron-Paaren und geladenen Hadronen, welche in Kernkollisionen in "Fixed-Target"-Geometrie erzeugt werden. Dafür stellt der Beschleuniger SIS18 der GSI Teilchenstrahlen mit einer kinetischen Energie von 1 bis 3.5 AGeV zur Verfügung. Das vorrangige experimentelle Ziel ist die Untersuchung der dichten und heißen Kernmaterie, wie sie in Schwerionenkollisionen entsteht, und ein besseres Verständnis der modifizierten Hadroneneigenschaften im nuklearen Medium zu erlangen.

Im HADES-Detektor ermöglichen 24 Mini Drift-Kammern (MDC) die Spurrekonstruktion und die Bestimmung der Teilchenimpulse über die Ablenkung der Spur in einem Magnetfeld. Darüberhinaus tragen die Driftkammern zur Teilchenidentifikation bei, indem sie den Energieverlust der Teilchen im Detektorgas messen. Das Auslesekonzept sieht vor, dass jeder Anodendraht mit einem Vorverstärker, einem Pulshaper und einem Diskriminator versehen wird. In der aktuell verwendeten Version der Ausleseelektronik umfasst der ASD-8 [New93] ASIC die genannten Module. Aufgrund der Limitiertheit der aktuell verbauten Zeit-zu-Digital-Wandler (TDC), insbesondere im Hinblick auf die erwarteten höheren Reaktionsraten an der zukünftigen FAIR-Anlage (HADES at SIS100), muss die bisher verwendete Ausleseelektronik unter Verwendung sogenannter Multi-Hit-TDCs erneuert werden. ASD-8 Chips sind für den Neubau der Analogstufe der Ausleseelektronik nicht mehr verfügbar, jedoch stellt der PASTTREC [Str17][Prz15] ASIC eine vielversprechende Ersatztechnologie dar, die im Rahmen dieser Arbeit auf ihre Eignung für die Auslese der HADES Driftkammern charakterisiert wurde. Dies geschah in mehreren Testsituationen und, wenn möglich, im direkten Vergleich zu ASD-8.

### Signalstudien

Bevor dedizierte Tests zum Vergleich beider Technologien an einer HADES Driftkammer durchgeführt werden können, ist ein detailliertes Verständnis des Eingangssignals vonnöten. Zu diesem Zweck wurde das Rohsignal einer MDC I-Zelle aufgezeichnet und in einer Schaltkreis-Simulation nachgebildet. Das Modell beschreibt exzellent die Zeitentwicklung des gesammelten Ladungssignals im Mikrosekundenbereich. Ein quantitatives Verständnis desselbigen ist wichtig für die korrekte Kalibrierung der Ladungsmessung, da der Signal-Ausläufer des Driftkammerpulses einen signifikanten Anteil der Gesamtladung beinhaltet und sich weit länger zieht als die effektive Ladungs-Integrationszeit der Ausleseelektronik (circa 10 ns). Der Versuch, das MDC-Stromsignal auf kurzen Zeitskalen (0 bis 100 ns) zu beschreiben, deckt auf, dass die MDC-Zelle besser durch ein Leitungsmodell (vgl. Koaxialkabel) beschrieben wird als durch einen simplen Kondensator. Darüberhinaus macht das Modell nur korrekte Aussagen, wenn explizit die nicht-vernachlässigbare Kapazität des Flex-Print-Kabels (FPC) miteinbezogen wird, welches als Signalleitung fest mit der Kammer/den Zellen verbunden ist. Das MDC-Pulsmodell-Signal wurde in eine idealisierte Schaltkreis-Simulation des PASTTREC-Shapers eingespeist, um so eine konkrete Demonstration der Auswirkungen der individuellen analogen Filterstufen zu erhalten. Die Signalverarbeitungskette ist konzeptuell identisch in beiden ASICs.



Zeitpräzision - Übersicht der verwendeten Bestimmungsmethoden

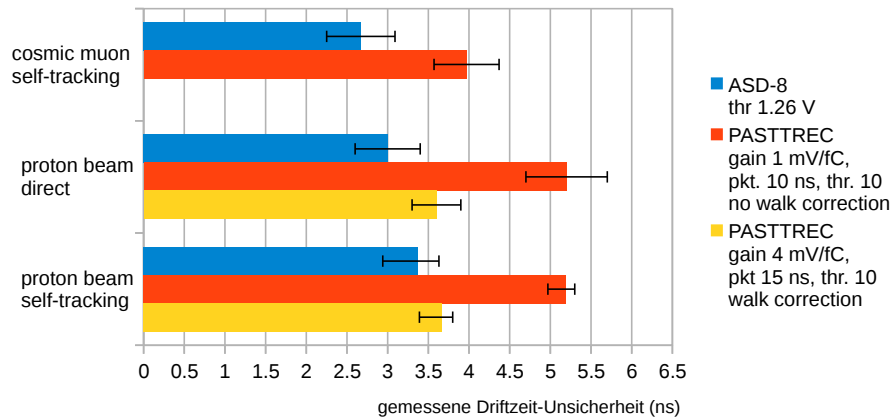


Abbildung 7.1: Vergleich der mit allen experimentellen Methoden bestimmten Zeitpräzisionen.

### Driftzeit-Messungen

Die Messpräzision der Driftzeit stellt ein wichtiges Leistungskriterium des Gesamtsystems, bestehend aus Detektor und Ausleseelektronik, dar. Die zwei zur Verfügung stehenden Versionen von Ausleseelektronik, die aktuelle ASD-8 basierte Analog-Karte und ein Prototype-Board mit dem PASTTREC ASIC, wurden in direktem Vergleich in zwei verschiedenen Szenarien zur Bestimmung der Driftzeit-Messpräzision getestet. Ein Set-up zum Tracking von kosmischen Myonen ermöglichte die Bestimmung der Zeitpräzision auf halber Distanz zwischen Feld- und Signaldraht mithilfe der sogenannten “Self-Tracking”-Methode. Ein dedizierter Teststrahl-Aufbau zur Performance-Messung mit minimalionisierenden Protonen erlaubte zweierlei Messungen, nämlich die Anwendung der Self-Tracking-Methode, sowie eine direkte Messung der Zeitpräzision für orthogonale Spuren mit beliebigem Abstand zum Signaldraht. Um die gewünschten Merkmale aus den aufgezeichneten Driftzeitverteilungen zu extrahieren, d.h. die mittlere Driftzeit und ihre Standardabweichung, wurde die jeweilige Driftzeit-Verteilung mit der Wahrscheinlichkeitsdichte-Funktion der sog. “Skew Normal Distribution” gefittet, wobei zusätzlich ein niedriges, breites gaussförmiges Podest zugelassen wird, welches als Untergrund betrachtet wird.

Die aus den Strahlzeit-Daten mit beiden Methoden (d.h. Self-Tracking, direkte Messung) gewonnenen Driftzeitpräzisionen stimmen im Rahmen ihres systematischen Fehlers überein (siehe Abb. 7.1). Die beste Zeitpräzision wurde bei halber Distanz zwischen Feld- und Signaldraht gemessen, also an der Stelle im Detektor, die durch die Self-Tracking-Methode zugänglich ist. Folglich weist die Zeitpräzision, als Funktion der Distanz zum Anodendraht, eine “W”-Form auf, wenn über die gesamte Breite der Zelle gescannt wird (siehe Abb. 7.2). Desweiteren wurde die Orts-Zeit-Relation der Driftzelle mit beiden ASICs gemessen, wobei sehr ähnliche Ergebnisse erzielt wurden. Während PASTTREC im Myonen-Aufbau mit nicht-optimalen Einstellungen (Verstärkungsfaktor, Shaper-Parameter, Diskriminator-Schwelle) betrieben wurde, ermöglichte der Strahltest Parameter-Scans, welche schließlich zu signifikant performanteren Einstellungskombinationen führten. Die Zeitpräzision von PASTTREC wurde zusätzlich durch eine Walk-Korrektur verbessert, basierend auf den gemessenen Time-Over-Threshold-Zeiten. Mit

den verbesserten Betriebsparametern und der Walk-Korrektur ist die Zeitpräzision von PASTTREC nur etwa 20 % schlechter als die mit ASD-8 gemessene (3.6 ns gegen 3.0 ns, auf halber Distanz zwischen Feld- und Signaldraht). Im Vergleich zwischen Strahltest und dem Myonen-Set-up fällt auf, dass das Myonen-Set-up systematisch bessere Zeitpräzisionen liefert, insbesondere für PASTTREC. Dieser Effekt wird der im Mittel etwa 37 % höheren Ladung in der Primärionisationsspur zugeschrieben, da die Myonen keine perfekt senkrecht einfallenden minimalionisierenden Teilchen sind. Sowohl die höhere Ionisationsdichte, als auch die durch den Einfallswinkel bedingte längere Teilchenspur im aktiven Detektorvolumen tragen zu diesem Effekt bei. Die resultierende größere mittlere Signalladung führt, nach theoretischen Überlegungen, zu einem geringeren Signal-Jitter hinter dem Diskriminator. Prinzipiell ist eine Präzisionsbestimmung mit minimalionisierenden Teilchen erwünscht, was den anspruchsvollsten Spezialfall für das Tracking von Teilchenspuren darstellt. Folglich sind die Strahltest-Ergebnisse als aussagekräftiger zu betrachten als die Ergebnisse, die mit dem Myonen-Set-up gemessen wurden. Letztere können allerdings als Konsistenzprüfung der “Self-Tracking”-Methode betrachtet werden. Sowohl im Myonen- als auch im Strahltest-Set-up verhielt sich das PASTTREC Prototyp-Board stabiler als die ASD-8-basierte Hardware, obgleich ein differenzieller Eingang zwecks Unterdrückung von Common-Mode-Noise fehlt. PASTTREC wies eine weit geringere Tendenz zu Selbstoszillation auf und war weniger sensitiv gegenüber elektromagnetischem Pickup-Noise. Dies zeigt sich unter typischen Laborbedingungen in einer höheren Detektionseffizienz. Aus einer Gasdetektorsimulation (GARFIELD) der MDC I-Zelle und aus der Interpolation der gemessenen Orts-Zeit-Relation resultiert eine lokale Elektronen-Driftgeschwindigkeit von  $66 \mu\text{m}/\text{ns}$  in der Mitte zwischen Feld- und Signaldraht. An dieser Stelle lässt sich, mit obiger Driftgeschwindigkeit und den aus den Strahltest-Daten gewonnenen Zeitpräzisionen, die Ortspräzision für senkrechte Spuren bestimmen:

$$\begin{aligned}\sigma_x &= (3.0 \pm 0.4) \text{ ns} \cdot 66 \mu\text{m ns}^{-1} = (198 \pm 26) \mu\text{m} \text{ (ASD-8)} \\ \sigma_x &= (3.6 \pm 0.3) \text{ ns} \cdot 66 \mu\text{m ns}^{-1} = (238 \pm 20) \mu\text{m} \text{ (PASTTREC)}\end{aligned}$$

Bedauerlicherweise überschreiten die obigen Werte das MDC Design-Ziel von  $150 \mu\text{m}$  [Mar05] um 32 % (ASD-8) and 59 % (PASTTREC) bereits an der Stelle des Detektors mit der besten Präzision. Es ist jedoch nicht ausgeschlossen, dass beide Auslesetechnologien eine bessere Ortspräzision erzielten, wenn das Set-up in einer gänzlich interferenzfreien Umgebung betrieben würde.

### Ladungsmessung

Beide ASIC-Technologien messen Ladung indirekt über die “Time-Over-Threshold”-Methode. Unter Verwendung derselben Betriebsparameter wie bei der Test-Strahlzeit, wurden beide ASICs systematisch mit einem Funktionsgenerator untersucht, welcher so programmiert wurde um einen Driftkammer-Puls mit seinem charakteristischen Abklingverhalten zu reproduzieren. Durch die Extrapolation des Signalsamples mit dem simulierten Pulsmodell ist es möglich, jeder Amplitudeneinstellung des Pulsers die volle Ladung des Pulses zuzuordnen. Dementsprechend kann durch Variation der Pulsamplitude eine Ladungskalibrierung durchgeführt werden. Für kleine Ladungen beobachtet man mit beiden ASICs eine nahezu logarithmische Beziehung zwischen der gemessenen Time-Over-Threshold und der Pulsladung, was den theoretischen Überlegungen auf Basis der Schaltung entspricht. Für größere Ladungen gehen die Kalibrierungsfunktionen beider ASICs in eine etwa lineare Funktion über, was als Nichtlinearität des Shapers

interpretiert wird. Aus den für die Kalibrierung gesammelten Daten kann eine obere Grenze für die intrinsische Ladungsmessungs-Präzision für beide ASICs bestimmt werden. Im Kalibrier-Set-up ist ASD-8 in der Lage, die Ladung des Testpulses mit einer relativen Präzision besser als 8% zu messen, während PASTTREC eine Präzision von besser als 5% bietet. Für beide ASICs, aber insbesondere für PASTTREC, verbessert sich die Präzision drastisch für höhere Eingangsladungen. Die Konsistenz der Ladungskalibration von PASTTREC wurde mithilfe einer  $^{55}\text{Fe}$ -Quelle überprüft, welche definierte Mengen von Primärionisation in einer Driftkammer-Zelle zu deponieren vermag. Sowohl die Lage der Hauptlinie als auch die Lage der Argon-Escapelinie im Ladungsspektrum des Detektors, welches aus den kalibrierten Time-Over-Threshold-Informationen gewonnen wurde, folgen einer exponentiellen Funktion in Abhängigkeit der Kammer-Hochspannung. Das Ladungsverhältnis beider Linien ist etwa 2 : 1, was den theoretischen Überlegungen entspricht. Für große Hochspannungs-Einstellungen ist die Position der Hauptlinie im Vergleich zur Argon-Escapelinie verzerrt, da Raumladungseffekte auftreten, die zu einer Sättigung der Gasverstärkung führen.

## Simulation

Abschließend wurde eine dreidimensionale GARFIELD-Simulation durchgeführt, um die Feldgeometrie und die Driftgeschwindigkeit der Elektronen in einer MDC I-Driftzelle zu verstehen. Die Simulation zeigt auf, dass Regionen zwischen den Kathodendrähten existieren, in denen die elektrische Feldstärke und folglich auch die Driftgeschwindigkeit auf nahezu Null absinkt. Primärionisation, die in oder in der Nähe von diesen Regionen deponiert wird, erzeugt zeitlich stark verzögerte Ausgangssignal-Anteile. Die Simulation wurde benutzt, um die Teststrahl-Situation nachzubilden. Zu diesem Zweck wurden senkrecht einfallende, minimalionisierende Spuren uniform über die gesamte simulierte Zelle verteilt. Es zeigt sich, dass die Driftzeit des am frühesten eintreffenden Elektrons die beste Korrelation mit der Spurposition aufweist, während alle folgenden Elektronen graduell weniger Ortsinformation tragen. Die simulierte Orts-Zeit-Relation weist eine hohe Ähnlichkeit mit den Orts-Zeit-Relationen auf, welche während des Strahltests gemessen wurden (siehe Abb. 7.2). Außerdem wird die experimentelle Beobachtung bestätigt, dass die beste Zeitpräzision auf halber Distanz zwischen Feld- und Signaldraht erzielt wird. Die Simulation ist in der Lage, die charakteristische "W"-Form der Zeitpräzision als Funktion der Spurposition über die Breite der Driftzelle zu reproduzieren. Rauschen, bzw. Störungen auf dem analogen Detektorsignal werden vereinfacht durch einen gaussförmigen Jitter approximiert, welcher zu den simulierten Ankunftszeiten der jeweiligen  $n$ -ten Elektronen hinzuaddiert wird. Für einen RMS-Jitter von 2 ns beschreiben die simulierten Präzisionskurven des dritten, bzw. vierten, eintreffenden Elektrons gut die Präzisionskurven, welche mit ASD-8, bzw. PASTTREC, während des Strahltests gemessen wurden. Genau wie bei den experimentellen Daten wurde die mittlere Driftzeit und die Driftzeitpräzision über das Anfitzen mit der Verteilungsfunktion einer Skew-Normal-Verteilung extrahiert. Durch die Simulation zweier halb überlappender Driftzellen konnte die charakteristische "Boomerang"-Form der Self-Tracking Driftzeit-Korrelation (Driftzeit-Differenz gegen Driftzeit-Summe) reproduziert werden.

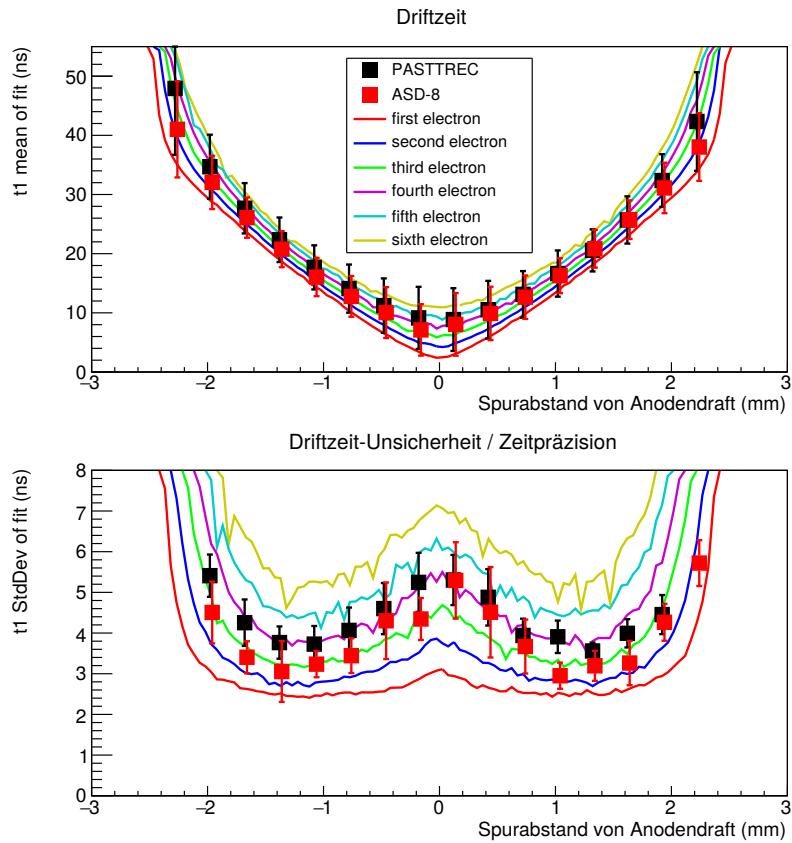


Abbildung 7.2: Vergleich zwischen GARFIELD-Simulation (erstes bis sechstes Elektron) und Strahlest-Daten, aufgezeichnet mit ASD-8 und PASTTREC. Die Form der Zeitpräzisions-Kurve wird von der Simulation reproduziert, wenn ein gaussförmig verteilter Jitter mit einer Standardabweichung von 2 ns auf alle simulierten Driftzeiten aufaddiert wird.

## Ausblick

Im Vergleich mit der aktuellen ASD-8 basierten Hardware konnte gezeigt werden, dass der PASTTREC-ASIC mit einer nur geringfügig schlechteren Zeitpräzision an einer HADES Driftkammer betrieben werden kann. Allerdings verhält sich PASTTREC im Betrieb stabiler und aufgrund der höheren Ladungsintegrationszeit gegenüber ASD-8, ist mit PASTTREC eine Verbesserung der Energieverlust-Messgenauigkeit zu erwarten. Die vorliegende Arbeit motiviert den Einsatz von PASTTREC für das geplante MDC Front-End Electronics Upgrade. Für ein großes Detektorsystem ist es darüberhinaus entscheidend, dass die an kleinen Set-ups erzielten Ergebnisse skalierbar sind.

Um die Skalierbarkeit einer PASTTREC-basierten Auslese zu testen, ist ein sogenannter “Full System Test” vorgesehen, d.h. der Versuch die zwei zentralen Ebenen einer MDC I-Kammer allein mit PASTTREC auszulesen. Dieses erfordert das gleichzeitige Auslesen von 384 einzelnen Signaldrähten mit 48 PASTTREC ASICs während kosmische Myonen getrackt werden. Hierzu kann das im Rahmen dieser Arbeit diskutierte Myonen-Set-up, bzw. die dafür entwickelten Analyse-Methoden, verwendet und gegebenenfalls verfeinert werden. Es soll untersucht werden, ob eine große Gruppe dieser Auslese-ASICs, dicht beieinander und über die selbe Spannungsversorgung betrieben, die selbe Betriebsstabilität zeigt wie die zwei PASTTREC Prototyp-Boards, welche im zuvor beschriebenen Myonen-Set-up und während des Strahltests verwendet wurden. Mögliche hierbei zu erwartende Phänomene wären ungewolltes Koppeln zwischen den Ausleseboards, welches zu unkontrolliertem Schwingen und/oder Übersprechen führt. Darüberhinaus sind systematische Studien über die Kanal-zu-Kanal-Offsets bezüglich des Schwellensettings nötig. Es gilt herauszufinden, inwieweit dieser Offset durch die in PASTTREC kanalweise einstellbare Baseline-Korrektur ausgeglichen werden kann.

## 7 Zusammenfassung

## A Appendix

### A.1 Flex print cable capacitance



Figure A.1: MDC I type cable.



Figure A.2: MDC II type cable.

In the HADES drift chamber system, two different types of flex print cables are used:

**MDC I type cables** For MDC I chambers only, a special type of printed circuit board has been designed and produced. On one side it is an apposition of several rigid "T"-shaped pieces with soldering contacts for sense wires on the head side in regular distances, corresponding to the distances of the sense wires within the chamber. The "T" pieces are glued inside the chamber frame and route the sense wire signals to the outside of the chamber. Each "T" part of the structure comprises eight sense wire signal lines. At the bottom end of each "T" shape, the rigid structure merges to flex print cables with various lengths (circa 14 cm to 17 cm) and at various angles to best bridge the distance between read-out electronics and the chamber frame. Next to each signal line, there is a pseudo-differential partner line, running in parallel with the sense line, beginning at the flex print connector, extending to right next to the soldering point at the head side of the "T" piece. In addition, the flex print cable provides a ground connection to the chamber frame.

**MDC II type cables** For MDC II, III and IV, the connectivity is provided by two separate entities. A rigid "T" piece in the chamber frame and individual straight flex print cables which are soldered to the bottom end of each "T" piece. Each cable contains four signal lines, four pseudo-differential partner lines and a ground connection to the chamber frame. The pseudo-differential line ends before the solder joint to the "T" piece. The flex print cables used have various lengths.

As discussed in section 2.4.4, the MDC flex print cable is part of the signal chain and contributes to the shaping of the analog detector signal. Especially the capacitance of the cable, in combination with the input impedance of the read-out electronics, forms a low-pass filter which reduces the steepness of the leading signal edge.

## A Appendix

The capacitance of the different types of cables are measured with an LCR meter. The working principle of the device is based on measuring the complex impedance of the device under test, when subjected to an AC signal (1 kHz, 10 kHz, 100 kHz, 1 MHz, 2 MHz). The cables are measured at the highest possible frequency setting (2 MHz), while comparing with the results at lower frequencies for estimating the systematic error of the measurement.

All cables are tested in two situations:

- With the pseudo-differential partner lines grounded at the FPC connector,
- and with the partner lines left unconnected.

For the MDC I cable, the measurement yields:

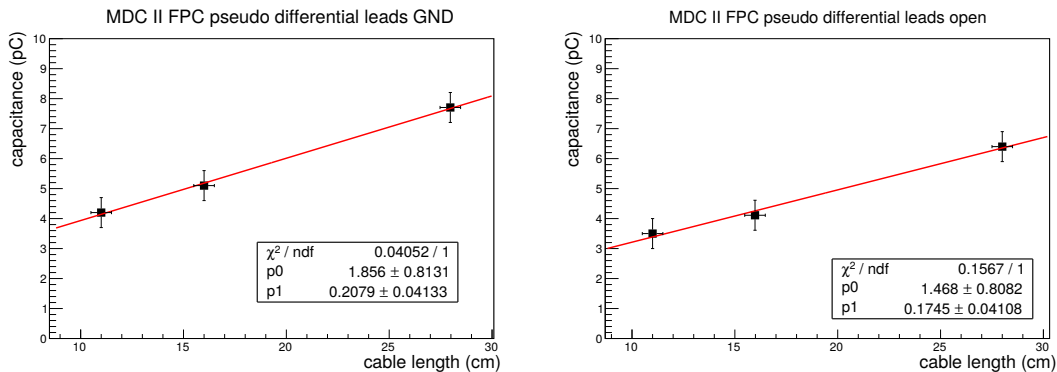
$$C_{\text{FPC, MDC I, partner GND}} = (25 \pm 2) \text{ pF} \quad (111)$$

$$C_{\text{FPC, MDC I, partner open}} = (13 \pm 2) \text{ pF} \quad (112)$$

For the MDC II type, cables of lengths 11 cm, 16 cm and 28 cm are tested and a linear regression is done for both grounding situations (see figure A.3). We arrive at the following formulas for MDC II type cables of length  $l$ :

$$C_{\text{FPC, MDC II, partner GND}} = (0.21 \pm 0.04) \text{ pF/cm} \cdot l[\text{cm}] + (1.9 \pm 0.8) \text{ pF} \quad (113)$$

$$C_{\text{FPC, MDC II, partner open}} = (0.17 \pm 0.04) \text{ pF/cm} \cdot l[\text{cm}] + (1.5 \pm 0.8) \text{ pF} \quad (114)$$



(a) Pseudo-differential lines connected to ground. (b) Pseudo-differential lines left unconnected.

Figure A.3: Linear regression of measured capacitances for MDC II type flex print cables of different lengths.

### A.2 Skew normal distribution

A standard normal distribution is described by the following probability density function:

$$\phi(x) = \frac{1}{\sqrt{2\pi}} e^{-\frac{x^2}{2}} \quad (115)$$

or alternatively by its cumulative distribution function:

$$\Phi(x) = \int_{-\infty}^x \phi(t) dt = \frac{1}{2} \left[ 1 + \text{erf} \left( \frac{x}{\sqrt{2}} \right) \right] \quad (116)$$



A distribution resembling the normal distribution, but introducing skewness can be created by the following probability density function [Azz14]

$$f(x) = 2\phi(x)\Phi(\alpha x) \quad (117)$$

with  $\alpha$ , the shape parameter. This function describes the so-called skew normal distribution which was first described by O'Hagan and Leonard in 1973 [OHA73]. Introducing a scale parameter  $\omega$  and a location parameter  $\xi$ , the distribution can be shifted in  $x$  and its width can be tuned.

$$f(x) = \frac{2}{\omega} \phi\left(\frac{x-\xi}{\omega}\right) \Phi\left(\alpha\left(\frac{x-\xi}{\omega}\right)\right) \quad (118)$$

The statistical mean  $\mu$ , the standard deviation  $\sigma$  and the standard definition of skewness  $\gamma_1$  for the skew normal distribution can be calculated from its natural parameters  $\omega$ ,  $\xi$  and  $\alpha$  with the following relations [Boo18]:

$$\mu = \xi + \omega\delta\sqrt{\frac{2}{\pi}} \quad \text{with} \quad \delta = \frac{\alpha}{\sqrt{1+\alpha^2}} \quad (119)$$

$$\sigma = \omega\sqrt{1 - \frac{2\delta^2}{\pi}} \quad (120)$$

$$\gamma_1 = \frac{4-\pi}{2} \frac{(\delta\sqrt{2/\pi})^3}{(1-2\delta^2/\pi)^{3/2}} \quad (121)$$

For  $\alpha = 0$ , the skew normal distribution is identical to a standard normal distribution.

Throughout the analysis in this thesis the probability density function implemented in the C++ boost library (v1.58.0) was used to provide the basis for all skew normal fit functions.

## A Appendix

### A.3 $^{55}\text{Fe}$ charge spectra recorded with PASTTREC

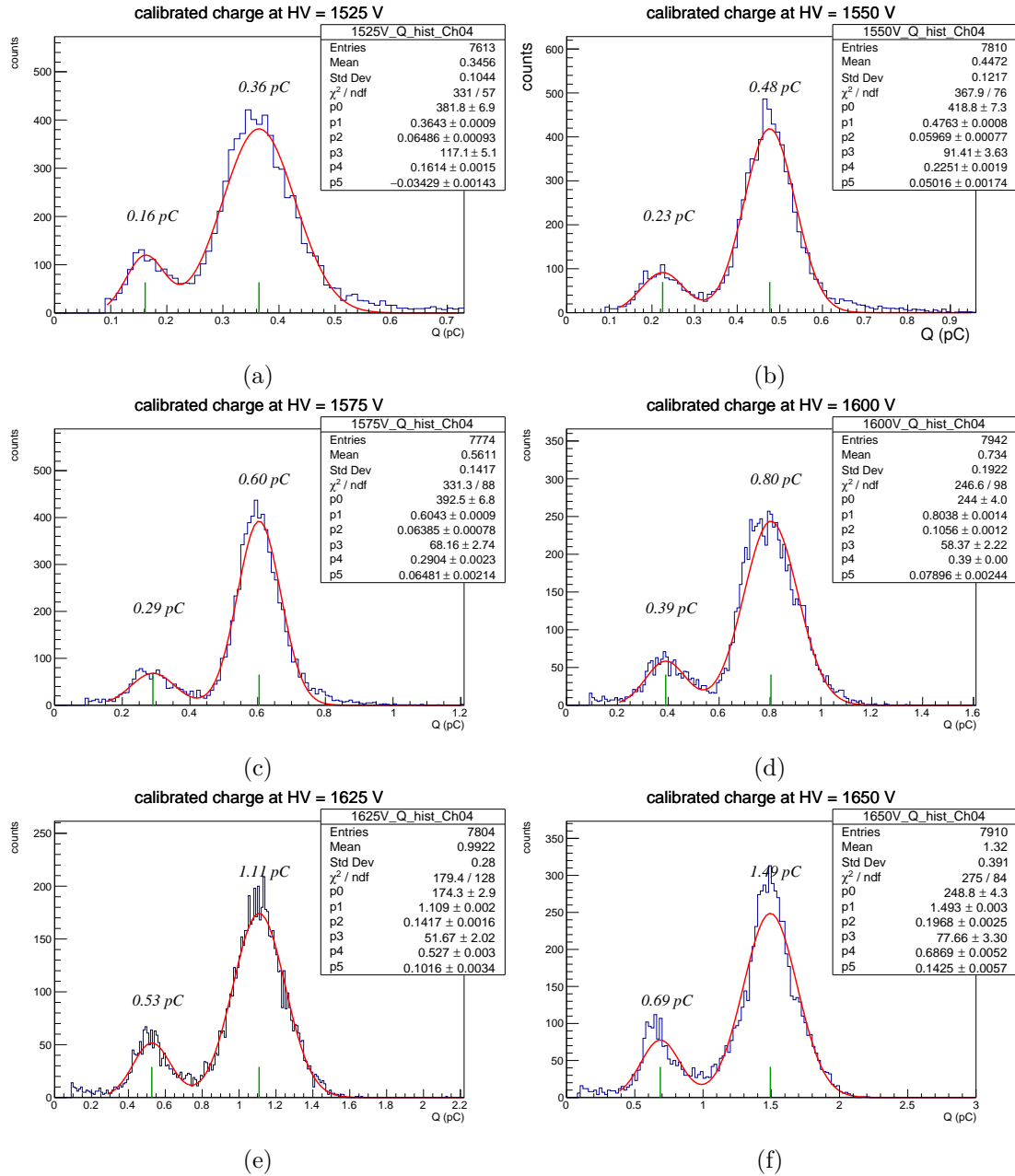


Figure A.4: Calibrated charge spectrum of an MDC I cell irradiated with  $^{55}\text{Fe}$ , recorded with PASTTREC. Gas mixture: 70 % Ar, 30 %  $\text{CO}_2$ . High voltage 1525 V to 1650 V.

### A.3 $^{55}\text{Fe}$ charge spectra recorded with PASTTREC

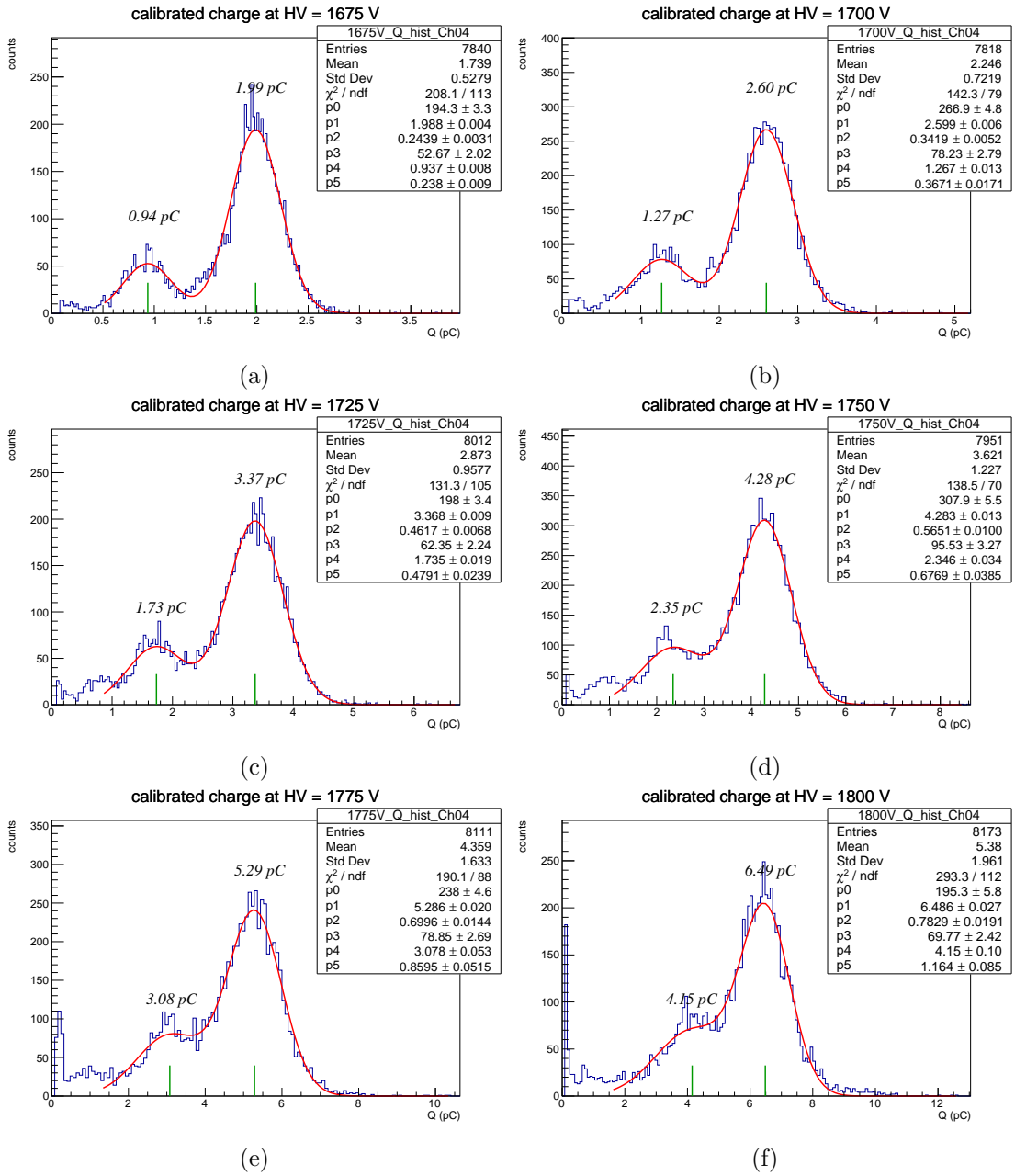


Figure A.5: Calibrated charge spectrum of an MDC I cell irradiated with  $^{55}\text{Fe}$ , recorded with PASTTREC. Gas mixture: 70 % Ar, 30 %  $\text{CO}_2$ . High voltage 1675 V to 1800 V.

## A Appendix

### A.4 Beam test MIPS charge spectra, PASTTREC

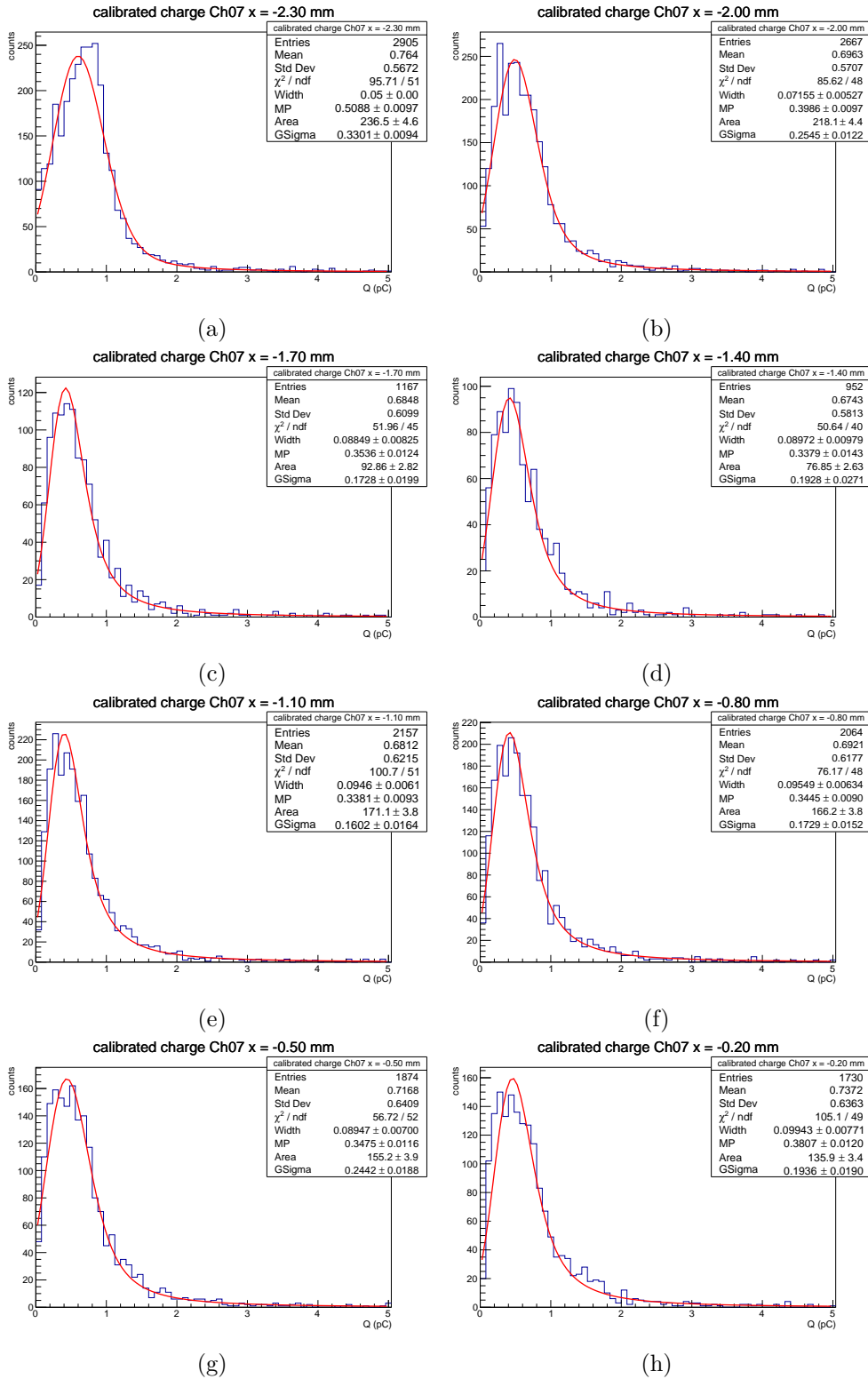


Figure A.6: Calibrated charge spectrum of an MDC I cell as reaction to minimum ionizing proton tracks at varying position, recorded with PASTTREC. Gas mixture: 70 % Ar, 30 % CO<sub>2</sub>. High voltage 1750 V. Histogram is fitted with a Languas function.

## A.4 Beam test MIPS charge spectra, PASTTREC

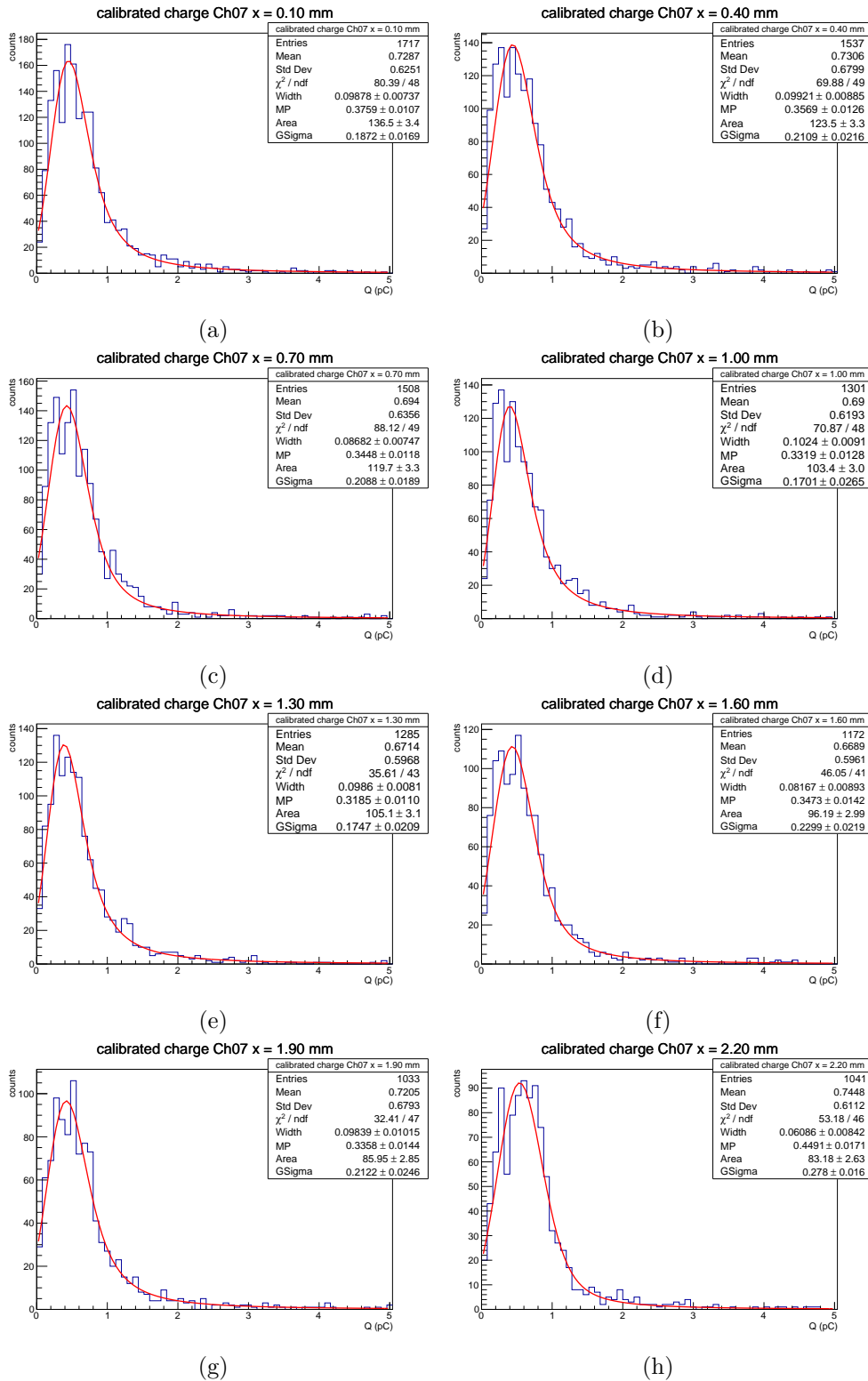


Figure A.7: Calibrated charge spectrum of an MDC I cell as reaction to minimum ionizing proton tracks at varying position, recorded with PASTTREC. Gas mixture: 70 % Ar, 30 % CO<sub>2</sub>. High voltage 1750 V. Histogram is fitted with a Langaus function.

## A.5 Table of ASD-8 thresholds

ASD-8 threshold input voltage (V)	HADES DAQ threshold setting (LSB of 8 bit DAC, hex)	TRB3 adapter board setting (LSB of 16 bit DAC, dec)
0.00	0	0
0.04	4	878
0.09	8	1756
0.13	C	2634
0.18	10	3512
0.22	14	4389
0.27	18	5267
0.31	1C	6145
0.35	20	7023
0.40	24	7901
0.44	28	8779
0.49	2C	9657
0.53	30	10535
0.57	34	11413
0.62	38	12291
0.66	3C	13168
0.71	40	14046
0.75	44	14924
0.80	48	15802
0.84	4C	16680
0.88	50	17558
0.93	54	18436
0.97	58	19314
1.02	5C	20192
1.06	60	21070
1.11	64	21947
1.15	68	22825
1.19	6C	23703
1.24	70	24581
1.28	74	25459
1.33	78	26337
1.37	7C	27215

Table A.1: Comparison of ASD-8 threshold voltage and digital to analog converter settings in the HADES DAQ and on TDC adapter board used in the cosmic muon tracking set-up and the beam test set-up.

A.5 Table of ASD-8 thresholds

ASD-8 threshold input voltage (V)	HADES DAQ threshold setting (LSB of 8 bit DAC, hex)	TRB3 adapter board setting (LSB of 16 bit DAC, dec)
1.41	80	28093
1.46	84	28971
1.50	88	29848
1.55	8C	30726
1.59	90	31604
1.64	94	32482
1.68	98	33360
1.72	9C	34238
1.77	A0	35116
1.81	A4	35994
1.86	A8	36872
1.90	AC	37750
1.95	B0	38627
1.99	B4	39505
2.03	B8	40383
2.08	BC	41261
2.12	C0	42139
2.17	C4	43017
2.21	C8	43895
2.25	CC	44773
2.30	D0	45651
2.34	D4	46529
2.39	D8	47406
2.43	DC	48284
2.48	E0	49162
2.52	E4	50040
2.56	E8	50918
2.61	EC	51796
2.65	F0	52674
2.70	F4	53552
2.74	F8	54430
2.78	FC	55307
2.83	100	56185

Table A.2: Continuation of table A.1.





## References

- [Ada11] J. Adamczewski-Musch, H.G.Essel, S. Linev, *Online Object Monitoring With Go4.V4.4*, IEEE TNS Vol.58, No.4, August 2011, pp. 1477-1481
- [Aga09] The HADES Collaboration, Agakichiev, G., Agodi, C. et al., *The high-acceptance dielectron spectrometer HADES*, Eur. Phys. J. A (2009) 41: 243. DOI: 10.1140/epja/i2009-10807-5
- [Azz14] Azzalini, Adelchi; Capitanio, Antonella (2014) *The skew-normal and related families* pp. 24–33. ISBN 978-1-107-02927-9.
- [Boi82] R. A. Boie, A.T. Hrisoho and P. Rehak, *Signal Shaping and Tail Cancellation For Gas Proportional Detectors*, NIM, A192 (1982) 365-374.
- [Boo18] C++ Boost Library v1.58.0 Documentation - Skew Normal Distribution [https://www.boost.org/doc/libs/1\\_58\\_0/libs/math/doc/html/math\\_toolkit/dist\\_ref/dists/skew\\_normal\\_dist.html](https://www.boost.org/doc/libs/1_58_0/libs/math/doc/html/math_toolkit/dist_ref/dists/skew_normal_dist.html) (retrieved 2018-08-21)
- [BR08] Walter Blum, Werner Riegler, Luigi Rolandi, *Particle Detection with Drift Chambers*, Springer Berlin Heidelberg, 2008, doi.org/10.1007/978-3-540-76684-1, ISBN 978-3-540-76683-4
- [CBM09] B. Friman, C. Höhne, J. Knoll, S. Leupold, J. Randrup, R. Rapp, P. Senger, *The CBM Physics Book, Compressed Baryonic Matter in Laboratory Experiments*, November 2009
- [CFW18] California Fine Wire Company *Datasheet TUNGSTEN 99.95% CS MATERIAL #: 100211* <http://www.calfinewire.com/datasheets/100211-tungsten9995cs.html> (retrieved 2018-11-16)
- [Dem09] Wolfgang Demtröder, *Experimentalphysik 2*, Springer-Lehrbuch, Springer, Berlin, Heidelberg, 2009, DOI: 10.1007/978-3-540-68219-6\_7, ISBN 978-3-540-68210-3
- [GAR] Rob Veenhof, *GARFIELD 9, Simulation of gaseous detectors*, <http://cern.ch/garfield> (retrieved 2018-11-16)
- [Had09] P. Finocchiaro, et al., *Technical Design Report for HADES-100*, internal note, [https://hades-new.gsi.de/sites/default/files/web/media/documents/Hades\\_at\\_SIS100\\_proposal.pdf](https://hades-new.gsi.de/sites/default/files/web/media/documents/Hades_at_SIS100_proposal.pdf) (retrieved 2018-11-22)
- [Hig75] Highland, Virgil L. *Some practical remarks on multiple scattering* Nuclear Instruments and Methods, Volume 129, Issue 2, p. 497-499 (1975). DOI: 10.1016/0029-554X(75)90743-0
- [Joh28] Johnson, J. (1928). *Thermal Agitation of Electricity in Conductors*. Phys. Rev. 32 (97). Bibcode:1928PhRv...32...97J. doi:10.1103/physrev.32.97.
- [KW16] H. Kolanoski, N. Wermes, *Teilchendetektoren - Grundlagen und Anwendungen* Springer-Verlag Berlin Heidelberg 2016, DOI: 10.1007/978-3-662-45350-6, ISBN 978-3-662-45349-0
- [LeC08] LeCroy Corporation, *LeCroy Wavesurfer Xs series Oscilloscopes - Operator's Manual*, 2008, [http://cdn.teledynelecroy.com/files/manuals/wsxs\\_om\\_rev.c.pdf](http://cdn.teledynelecroy.com/files/manuals/wsxs_om_rev.c.pdf) (retrieved 2018-11-16)

## References

- [LNHB18] Laboratoire National Henri Becquerel, *Table de Radionucléides*, [http://www.nucleide.org/DDEP\\_WG/Nuclides/Fe-55\\_tables.pdf](http://www.nucleide.org/DDEP_WG/Nuclides/Fe-55_tables.pdf) (retrieved 2018-11-15)
- [Lyn91] G.R. Lynch and O.I. Dahl, *Approximations to multiple Coulomb scattering*, Nucl. Instrum. Methods B58, 6 (1991), DOI: 10.1016/0168-583X(91)95671-Y
- [MAG] Rob Veenhof, Stephen Biagi, *Magboltz - transport of electrons in gas mixtures*, <http://magboltz.web.cern.ch/magboltz/> (retrieved 2018-11-16)
- [Mar05] Jochen Markert *Untersuchung zum Ansprechverhalten der Vieldraht-Driftkammern niedriger Massenbelegung des HADES Experimentes* Dissertation zur Erlangung des Doktorgrades der Naturwissenschaft, Fachbereich Physik, Johann Wolfgang Goethe-Universität Frankfurt, 2005
- [Mic11] J. Michel et al., *The upgraded HADES trigger and data acquisition system*, 2011 JINST 6 C12056, DOI: 10.1088/1748-0221/6/12/C12056
- [NEB] Rob Veenhof, Supratik Mukhopadhyay, Nayana Majumdar, *A nearly exact Boundary Element Method*, <http://nebem.web.cern.ch/nebem/> (retrieved 2018-11-16)
- [Nei13] A. Neiser et al., *TRB3: a 264 channel high precision TDC platform and its applications*, Topical workshop on electronics for particle physics 2013, 23–27 September 2013, Perugia, Italy, <http://dx.doi.org/10.1088/1748-0221/8/12/C12043>
- [New93] F.M. Newcomer *A Fast Low Power, Amplifier-Shaper-Discriminator for High Rate Straw Tracking Systems* IEEE Transactions on Nuclear Science, 40(4):630, August 1993
- [NIS18] National Institute of Standards and Technology, *X-Ray Mass Attenuation Coefficients - Argon*, <https://physics.nist.gov/PhysRefData/XrayMassCoef/ElemTab/z18.html> (retrieved 2018-12-11)
- [OHA73] O'Hagan, A. and Leonard, T. (1976). *Bayes estimation subject to uncertainty about parameter constraints* Biometrika, 63, 201-202.
- [PDG10] K. Nakamura et al. (Particle Data Group) *Review of Particle Physics* Journal of Physics G 37 075021 (2010)
- [PDG16] C. Patrignani et al. (Particle Data Group), *Chinese Physics C*, 40, 100001 (2016) DOI: 10.1088/1674-1137/40/10/100001
- [Prz15] Dominik Przyborowski *Zastosowanie submikronowych technologii VLSI w rozwoju wielokanałowych układów scalonych do odczytu detektorów cząstek jonizujących*, doctoral thesis, AGH University of Science and Technology, Cracow, 2015
- [RF18] RF Cafe, *Coaxial Cable Equations Formulas* <http://www.rfcafe.com/references/electrical/coax.htm> (retrieved 2018-11-16)
- [Rug05] Wilson J. Rugh, *Notes for Signals and Systems, Version 1.0, 2000-2005* <https://www.ece.jhu.edu/~cooper/courses/214/signalsandsystemsnotes.pdf> (retrieved 2018-11-16)

- [RW99] R. Rapp, J. Wambach, *Chiral symmetry restoration and dileptons in relativistic heavy ion collisions* Adv.Nucl.Phys. 25 (2000) 1, DOI: 10.1007/0-306-47101-9\_1
- [Sau77] F.Sauli *Principles of operation of multiwire proportional and drift chambers* Lectures given in the academic training programme of CERN, CERN; European Organization For Nuclear Research, Geneva, 1977
- [Sch01] B. Schwingenheuer, *Electronics commissioning experience at HERA-B*, 7th Workshop on electronics for LHC experiments, Stockholm, Sweden, 10-14 Sep 2001: Proceedings, p. 40-44
- [SPI14] Linear Technology Corporation / Analog Devices, *LTspice IV, Version 4.23h*, 2010-2014, <http://ltspice.analog.com/software/LTspiceIV.exe> (retrieved 2018-12-11)
- [Ste18] J. Steinheimer, et al., *The Hot and Dense QCD Equation of State in Heavy Ion Collisions and Neutron Star Mergers*, Springer Proc.Phys. 208 (2018) 191-198, DOI: 10.1007/978-3-319-94256-8\_22
- [Str17] Paweł Strzempek, *Development and evaluation of a signal analysis and a read-out system of straw tube detectors for the PANDA spectrometer*, doctoral thesis, Jagiellonian University, Cracow, 2017
- [Ugu13] C. Ugur, et al., *264 Channel TDC Platform applying 65 channel high precision (7.2 ps RMS) FPGA based TDCs*, in: NoMe - TDC 2013 - 2013 IEEE Nordic Mediterranean Workshop on Time to Digital Converters, Proceedings. 10.1109/NoMeTDC.2013.6658234.

## References

## Danksagung

Ich danke meinem Doktorvater Joachim Stroth, sowie meinem Mentor Christian Müntz für die Ermöglichung und die ausgezeichnete Betreuung dieser Arbeit. Besonderer Dank gilt auch an vorderster Stelle meinen Kollegen Christian Wendisch und Jan Michel für die kontinuierliche technische, fachliche und tatkräftige Unterstützung in *allen* experimentellen Aspekten dieser Arbeit.

Desweiteren danke ich:

- Jerzy Pietraszko und Adrian Rost für die Unterstützung im Umgang mit den Diamant-Detektoren während der COSY-Strahlzeit,
- Jochen Markert für seine Hilfe beim Verstehen von GARFIELD-Skripten,
- Michael Deveaux für die Bewältigung der bürokratischen Hürden zu Beginn der Promotion, sowie für den interessanten Ausflug ins Reich der Korallen,
- Lothar Naumann und Xingming Fan für die Bereitstellung des Laser-Testsetups in Rossendorf, welches zu entscheidenden Lernerfahrungen für den Betrieb der Signalauslekette geführt hat,
- Marianne Frey und Ingo Fröhlich für die Zähmung der alltäglichen Bürokratie am IKF,
- Michael Traxler und Sergey Linev für die Einführung in die Benutzung der TDCs und des Go4-Frameworks,
- Wolfgang König für seine Einsichten in das geheime Eigenleben passiver Bauelemente,
- Christoph Blume für das konstruktive Beiwohnen meiner PhD-Committee-Meetings und seine Bereitschaft als Zweitgutachter zu fungieren,
- Michael Petri für den täglichen moralischen Beistand,
- Philipp Klaus für die Gespräche und die gute Zeit während der gemeinsam besuchten Tagungen und Konferenzen, sowie für die zahlreichen Tipps und Tricks rund um Linux,
- Roland Weirich für den erfolgreichen Kampf mit polnischen Bonddrähten,
- Manuel Lorenz für das gelegentliche Teilhabenlassen an seiner Weisheit,
- Marcus Iberler für die “Ehrenmitgliedschaft” in der Plasmaphysik-Gruppe sowie für die Nachmieterschaft seiner Wohnung in Bornheim,
- Meinen geschätzten, kurzweiligen (Ex-)Kolleg\*Innen Melanie, Michal, Benni, Philipp S., Tobias, Samir, Heidi, Claudia, Timo, Qiyan, Gisa, Behruz,
- Meinen aufstrebenden Nachwuchs-Kollegen Florian (für die Schokolade), Holger (für typische Holger-Sachen), Simon (dem das Undenkbare gelang), Ben (für Zitate auf Latein, deren Bedeutung mir unerschlossen blieb), Marvin (für das Hochhalten ökologischer Ideale auf Facebook),
- Bianca v. K. für die Versorgung mit Vitaminen und dafür, dass sie mir beigebracht hat wie man in den Urlaub fährt,

## Danksagung

- Volker für Kaffee, Nüsse, Bier, Käsebröte, gute Gespräche und geteilte Lebensweisheit in seinem Wohnzimmer in Niederursel,
- Für gute Freundschaft: Jan-Christoph, Jonatan, Balou, Ruben, Sven H., Philipp E., Sero, Antje, Sven K., Claudia, Anna, Mathilde, Bianca O.,
- Wiebke für das gemeinsame Durchstehen der Widrigkeiten des Physikstudiums und für die vielen guten Momente dazwischen,
- *Toy of the Ape* und der *Steven Stealer Band* für Lebensfreude durch Live-Musik,
- Victoria, dass ich einer ihrer *wenigen* guten Freunde sein durfte und, dass ich im Cafe Habibi die doppelte Menge Soße zu meinen Falafel hatte.

Ich danke Claus-Heim Niemand<sup>†</sup>, der bei mir schon früh das Interesse für Elektronik und IT erkannt und gefördert hat. Von ihm bekam ich im Alter von sieben Jahren meinen ersten Lötkolben sowie mein erstes Digitalmultimeter und im Alter von zehn Jahren meinen ersten Computer.

Ich danke meiner Mutter und meinem Onkel Ludger dafür, dass sie mit mir in meinen jungen Jahren Star Trek geschaut haben. Ich danke meinem Vater<sup>†</sup> dafür, dass er mich bei dem Verfolgen meiner naturwissenschaftlich/technischen Interessen stets unterstützt hat, auch wenn er diese nicht geteilt hat; ebensowenig wie ich seine Vorliebe für Imkerei und Gartenarbeit.

## Curriculum Vitae

### Personal Information

Name: Michael Wiebusch  
Address: Ingolstädter Straße 38  
60316 Frankfurt  
Date of birth: February 11<sup>th</sup>, 1989  
Nationality: German

### Education and Qualifications

since 11/2014 PhD in Physics  
at Goethe University Frankfurt am Main  
10/2012-10/2014 Master of Science in Physics  
at Goethe University Frankfurt am Main  
04/2009-10/2012 Bachelor of Science in Physics  
at Goethe University Frankfurt am Main  
09/1999-06/2008 Abitur (A-levels)  
at Gustav-Stresemann-Gymnasium, Bad Wildungen  
Main subjects: Mathematics, Physics

### Work Experience

08/2008-04/2009 Community Service  
at Rheumaklinik Bad Wildungen